VELOCITY PROFILE MEASUREMENT IN A HORIZONTAL FLUID LAYER CONTAINING HEAT SOURCES USING THE TECHNIQUE OF LASER-DOPPLER ANEMOMETRY

by

Robert Wayne McGriff

B.S. Kansas State University, 1977

A MASTER'S THESIS

submitted in partial fulfillment of the
requirements for the degree

MASTER OF SCIENCE

Department of Nuclear Engineering
KANSAS STATE UNIVERSITY
Manhattan, Kansas

1980

Approved by:

Thomas W. Foster
Major Professor

THIS BOOK
CONTAINS
NUMEROUS PAGES
WITH THE ORIGINAL
PRINTING BEING
SKEWED
DIFFERENTLY FROM
THE TOP OF THE
PAGE TO THE
BOTTOM.

THIS IS AS RECEIVED
FROM THE
CUSTOMER.

TABLE OF CONTENTS

NOMENCLATURE

f_D	Doppler-signal frequency, hz
$\overline{f}_D$	Mean Doppler-signal frequency, hz
g	gravitational acceleration, cm/sec^2
J	turbulence intensity
k	thermal conductivity, W/m^2 C
L	total fluid layer depth, cm
Lo	depth of conduction sublayer, cm
L*	characteristic length scale for the fluid layer (corresponds to ΔT^*), cm
q	volumetric heat generation rate, W/m^2 C
r	scattering-volume radial distance from center of glass, mm
r^2	correlation coefficient
Ra	Rayleigh number
Ra_C	critical Rayleigh number
Ra_E	external Rayleigh number
Ra_{KG}	internal Rayleigh number
T_0	lower fluid-boundary temperature, C
T_1	upper fluid-boundary temperature, C
ΔT^*	characteristic (destabilizing) temperature difference within the fluid layer, C
V_T	rotating glass-plate tangential velocity, mm/sec
α	coefficient of volumetric expansion, C^{-1}

β thermal diffusivity, cm^2/sec

θ half-angle of separation between two beams forming scattering volume in air

ν kinematic viscosity, cm^2/sec

ν_i channel-number frequency equivalent, hz

$\psi_i(\nu_i)$ no. of counts in MCA channel location corresponding to ν_i

$\psi_i(\ln\nu_i)$ no. of counts in MCA channel location corresponding to $\ln \nu_i$

ω angular speed of rotating glass plate, rad/sec

LIST OF ILLUSTRATIONS

LIST OF TABLES

1.0 INTRODUCTION

1.1 General Description and Significance of the Problem

In the recent months following the accident at Three Mile Island much public attention has been focused on the question of nuclear power plant safety. This is a vital issue, as nuclear power plants are expected to play a significant role in reducing America's dependence on foreign oil supplies. The safety record of the nuclear power industry in this country is excellent, thus illustrating that nuclear power can be used in this country as a safe and reliable source of energy.

Even with the excellent safety record of the nuclear power industry, the accident at Three Mile Island aptly demonstrates that the highly improbable can happen. Thus no prudent nuclear power plant designer can ignore the possibility of an occurrence of the postulated worst-case accident - a loss of coolant followed by a core meltdown and the subsequent formation of a layer of molten fuel in the pressure vessel. Nuclear power plant designers must, therefore, design nuclear power plants in such a manner as to minimize the consequences of such accidents.

One particular area of concern for designers working with the postulated worst-case accident is the heat transfer mechanism in a layer of molten fuel. Specifically, the determination of the rate of melting or penetration of the reactor vessel and sacrificial

protective barriers by a horizontal layer of molten fuel is still plagued by uncertainties in the thermal-hydraulic mechanisms. One of the major emphases of this investigation was to obtain vertical-velocity measurements within a horizontal fluid layer approximating the supposed configuration occurring in such an accident. Specifically, horizontal fluid layers with unequal boundary temperatures and containing internal heat sources were studied.

Natural convection and conduction are the two heat transfer mechanisms in such horizontal fluid layers at low to moderate temperatures. As energy is added either externally or internally to an initially stagnant fluid layer of uniform density heat is transferred by conduction alone until such a time that a density gradient develops across the vertical extent of the layer. An imbalance between the viscous and buoyant forces develops, and when the buoyant forces exceed the viscous forces fluid motion ensues. The initial conductive heat transfer mechanism is then augmented by large-scale mixing of the fluid. Heat transfer due to density-driven fluid motion is known as natural-convection heat transfer.

Buoyant forces can be created either by differential heating of the fluid layer, in which one fluid boundary is heated to a higher temperature than the other fluid boundary, or by internal heat sources in the fluid layer. Natural-convection heat transfer due to differential heating of the horizontal fluid-layer boundaries

has been studied much more extensively than convection due to the presence of internal heat sources. The temperature profile in the initial conduction state for the differential heating case is linear. Because the density of a fluid is a function of the temperature, this initial linear temperature profile produces a density gradient to such an extent that instabilities are developed. The type of convective heat transfer developed when the fluid layer is heated from below is known as Benard convection, in honor of the scientist (Benard, 1901), who first extensively studied this type of problem.

The use of internal heat sources in the fluid layer creates a nonlinear temperature profile. Again, this temperature gradient causes a density gradient to develop in the fluid layer leading to convective heat transfer. Convection heat transfer due to internal heat sources will form one of the major foci of this study.

The dimensionless parameter used in characterizing natural convection in a fluid layer is the Rayleigh number. For fluids satisfying the classical Boussinesq approximation the Rayleigh number can be expressed as (Kulacki and Goldstein, 1972)

$$Ra = \frac{g \beta \Delta T^* L^{*3}}{\alpha \quad k} \quad . \qquad (1)$$

Physically, the Rayleigh number represents the ratio of the buoyant forces to the viscous forces times the ratio of the heat convected to the heat conducted. The value of the Rayleigh number at which natural convection begins is known as the critical Rayleigh number.

Several different boundary conditions can be applied to the case of a horizontal fluid layer containing heat sources. The boundary conditions of interest for this study are shown in Fig. 1. Since the fluid boundaries have unequal temperatures, buoyant forces are created in the horizontal layer by both differential heating of the fluid layer and through the use of internal heat-sources.

Because the buoyant forces formed in the fluid layer depicted in Fig. 1 are created by both differential heating and internal energy-sources, it is convenient to define two Rayleigh numbers using Eq. (1) to describe the heat transfer process. One is the external Rayleigh number, expressed as (Boon-Long, 1978)

$$Ra_E = \frac{g \beta L^3 (T_o - T_1)}{\alpha \nu} . \qquad (2)$$

The external Rayleigh number characterizes natural convection due to differential heating. The second Rayleigh number is defined as the internal Rayleigh number and is expressed as (Kulacki and Goldstein, 1972)

$$Ra_{KG} = \frac{g \beta q L^5}{64 \alpha \nu k} . \qquad (3)$$

The form of the internal Rayleigh number given in Eq. (3) characterizes natural convection in a horizontal fluid layer with equal boundary temperatures and containing internal heat sources.

In lieu of comprehensive experimental information on the mechanisms of energy transport within a fluid layer, Baker, Faw,

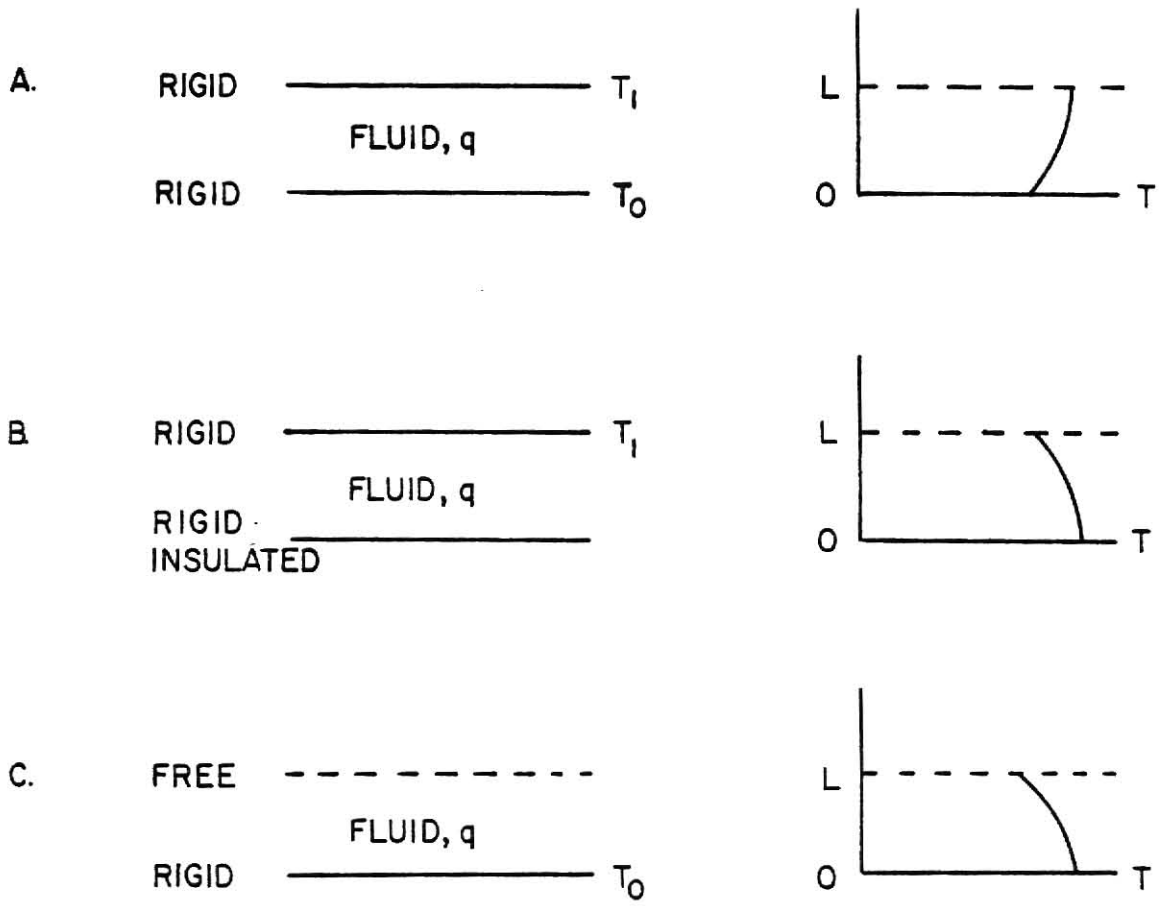

Fig. 1. Possible Boundary Conditions and Temperature Profiles for a Horizontal Fluid Layer with Unequal Boundary Temperatures and Containing Internal Heat Sources (from Boon-Long, 1978).

and Kulacki (1976) have proposed a semi-empirical model of the heat transfer process that takes place in the fluid layer depicted in Fig. 1.a. In this model it is assumed that the horizontal fluid layer can be divided into two sublayers at the plane of maximum horizontally-averaged temperature (see Fig. 2). In the upper sublayer all heat transfer occurs in the upward direction, while in the lower sublayer all heat transfer occurs in the downward direction. It is further specified in the model that the mode of heat transfer in the lower sublayer is conduction while in the upper sublayer the predominant mode of heat transfer is convection. In solving the resulting equations it is assumed that the boundary between the two sublayers (the plane of maximum-average temperature) is insulated. Of interest to this study is the following relationship derived from the model between the fraction of downward heat transfer and the heights of the two predicted sublayers:

$$\eta_{BFK} = \frac{L_o}{L} \quad . \tag{4}$$

The results predicted with this model have been compared with those from an experimental study carried out by Boon-Long (1978). In the latter study, the extent of downward heat transfer was correlated for the first time in general with the internal and external Rayleigh numbers. For negative external-Rayleigh numbers (i.e., upper fluid-boundary temperature greater than the lower fluid-boundary temperature) the experimental results agreed well with

A. COMPOSITE LAYER

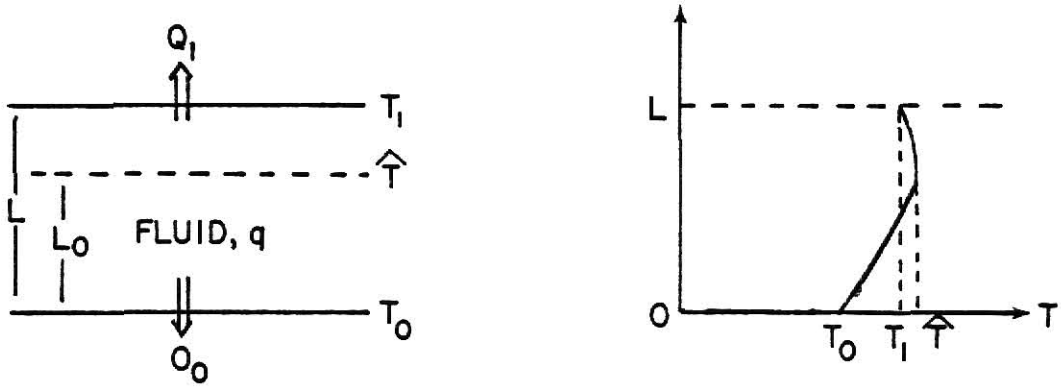

B. SEPARATED LAYER

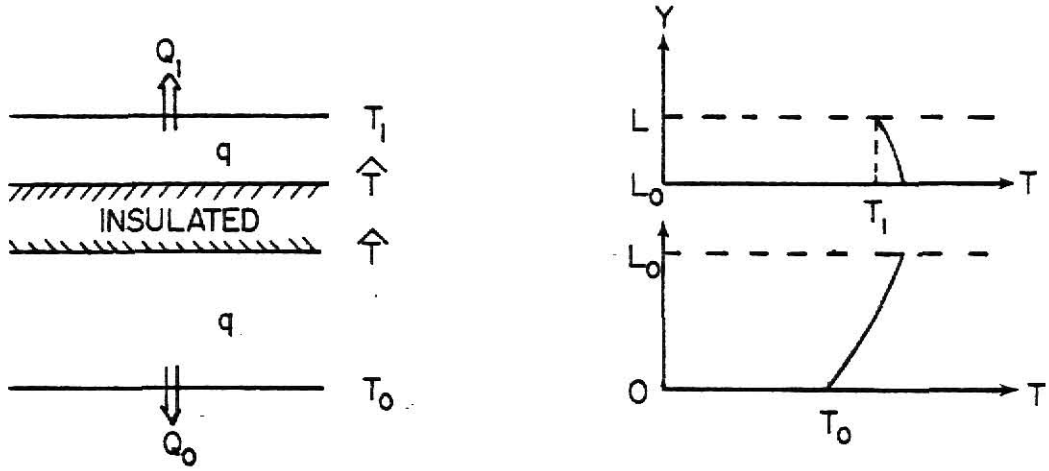

Fig. 2. Schematic Representation of Separated Fluid Layer with Unequal Boundary Temperatures and Containing Internal Heat Sources (from Boon-Long, 1978).

those predicted by the model. For positive external Rayleigh numbers, the experimental results did not agree as well. One possible explanation for this disagreement is that destabilizing buoyant forces are produced in the lower sublayer. Therefore the assumption of purely conductive heat transfer in the lower sublayer may not be a valid model for the case of positive external Rayleigh numbers.

Because little work has yet been done on quantifying the convection profiles in horizontal fluid layers subject to natural convection, one of the major emphases of this investigation was to obtain vertical velocity measurements with the horizontal fluid layer depicted in Fig. 1.a. Using the technique of laser-Doppler anemometry (LDA), an experimental program was devised to test the validity of the assumptions associated with the Baker, Faw, and Kulacki model.

1.2 Review of Literature

Relatively few experimental studies have been carried out on the measurement of even the gross characteristics of the fluid-flow patterns present in either Benard convection or convection due to internal heat-sources. Fewer still have been performed using techniques such as laser-Doppler anemometry from which detailed information is possible. A review of LDA principles (including literature citations) is presented in Appendix A. It is sufficient to say at this point that laser-Doppler anemometry is an experimental technique utilizing laser-light scattering to obtain local velocity measurements in a fluid flow without dis-

turbing the fluid-flow pattern. The few natural-convection studies that have been done with LDA techniques have dealt almost exclusively with Bernard convection. In addition to a review of LDA studies of natural convection, this section will also present a review of those studies which examined the gross characteristics of the convective fluid-flow patterns developed in horizontal fluid layers containing internal heat sources.

1.2.1 Convective Patterns

Of particular interest in this study is the shape of the fluid flow patterns which are developed in horizontal fluid layers as a consequence of internal heat sources. Tritton and Zarraga (1967) looked at this problem using a horizontal fluid-layer containing an aqueous zinc-sulfide solution that was electrolytically heated between two lateral zinc electrodes. The fluid layer was cooled from above and insulated at the bottom. The flow patterns were visualized using polystyrene beads and photographed. At steady state, the authors observed cellular patterns similar to those found in Bernard convection with one important difference - the fluid descended in the center of the cell and ascended at the peripheries of the cellular patterns in the layer containing internal heat generation. They also observed that the horizontal scale of the convection pattern was unusually large, i.e., the distance between the rising and falling currents was observed to be typically five times the depth of the layer.

In a follow-up study using a similar convection cell, Schwiderski and Schwab (1971) found that the thermal coefficient of resistivity in the fluid layer played a role in how the convection patterns developed. They found that the convection currents were not affected significantly by the temperature and flow direction of the cooling water, the thermal properties of the bottom plate, or the temperature distribution in the side walls. It was determined that the thermal properties of the upper cooling plate had some effect, but the primary factor affecting the development of the cellular patterns was found to be the electric current passing through the fluid layer. Thus the strong dilution of the convection cells observed by Tritton and Zarraga was essentially caused by uneven electrical heating due to the temperature-dependence of the fluid-layer electrical conductivity. If this effect is eliminated there does not appear to be any major differences in the shape of the convection patterns observed for convection due to internal heating and for convection due to external heating.

Schwiderski and Schwab also reported on the development of cellular patterns in a fluid layer containing heat sources. First, there was the development of small, more or less regular hexagonal patterns which were unstable due to the directional dependence of the electric current. The instability of the hexagonal patterns existed beyond the time at which the electric current reached its final value. Thereafter a transition to a roll pattern was noted; moreover, for large Rayleigh numbers the roll patterns developed were relatively stable.

Kulacki and Goldstein (1972) investigated among other features the nature of the flow and mean temperature fields in the post-stability regimes for a horizontal fluid layer with equal boundary temperatures containing internal heat sources. In their experimental system a dilute layer of aqueous silver-nitrate solution was electrolytically heated between two silver-plated copper flats that formed two of the side walls. The upper and lower boundaries were composed of copper plates, and were cooled to the same temperature with a temperature regulation of less than 0.04 C. Temperature measurements were recorded using a Mach-Zehnder interferometer. From observation of the mean-temperature fields obtained with the Mach-Zehnder interferometer the authors observed three regimes of motion: (a) gentle laminar convection for $Ra_C \leq Ra_{KG} \leq 5 \times 10^3$, (b) developed laminar convection for $5 \times 10^3 \leq Ra_{KG} \leq 10^4$, and (c) transition to turbulent convection for $Ra_{KG} > 10^5$. For the first region conduction was still a relatively important mechanism for energy transport in the fluid layer.

1.2.2 LDA Studies

Several studies have been carried out using LDA techniques to investigate the velocity profiles obtained in natural convection. Amenitskii, Rinkevichyus, and Kirsanov (1973, 1974) investigated the velocity profile of natural convection from a vertical heated wall using an LDA system. An electric heater was attached to one of the vertical walls, while the opposite wall from the heater was

cooled by a flowing supply of constant temperature water. The remaining two vertical walls were made of glass to allow the laser beams to pass through the cell. Vertical velocity measurements were made in the horizontal plane approximately halfway from the bottom of the cell. The results agreed well with the theoretical predictions of Ostrach (1953, as referenced in Amenitskii, Rinkevichyus, and Kirsanov (1974)).

Adrian (1975) observed measurements of both the vertical velocity and temperature fluctuations at fixed points in the turbulent convection flow-field present in water over ice. Convection occurs in this situation because the density of water attains its maximum value at a temperature t_m = 3.98 C. Thus for water over ice in which the lower boundary temperature is less than t_m and the upper boundary temperature is greater than t_m, the fluid layer below t_m develops a density gradient that in turn causes convective motion to occur in this layer. The fluid layer above t_m is stable. Adrian was especially interested in the large magnitudes of the temperature and velocity fluctuations near the interface between the convection layer and the stable conduction layer. These fluctuations were attributed by Townsend (1967, as quoted in Adrian's paper) to fluid impactions on the base of the stable region, causing ripples in the stable region whose spread is predominantly horizontal. Using a reference-beam LDA system (see Appendix A.4.1 for discussion) to make the measurements, Adrian noted velocities less than 1 mm/sec.

Berge and Dubois (1976) used an LDA system to study the time-dependent behavior of the velocity in Bernard convection. They were most interested in the transition to turbulence; however, unlike other papers in which the vertical-velocity component was measured, Berge and Dubois measured the horizontal component of velocity. For values of a non-dimensional parameter ($\epsilon = \frac{Ra - Ra_c}{Ra_c}$) greater than thirty it was observed that the velocity amplitude at a particular location in the fluid showed intermittent oscillations versus time. It was also observed that if at a point in the fluid layer horizontal oscillations in the velocity were occurring, the horizontal velocity at other points did not necessarily oscillate in time. As ϵ increased in value it was observed that the frequency of the horizontal oscillations also increased and that the oscillations became more continuous in time. For large values of ϵ (greater than 2000) the fundamental frequency of the oscillations disappear to give rise to a broad turbulent spectrum. Berge and Dubois believe these oscillations represent the most important step in the transition to turbulence in Bernard convection.

Garon and Goldstein (1973) examined both the heat transport and the vertical velocity component for a fluid layer heated from below (Benard convection) for relatively high Rayleigh numbers. Using a reference-beam LDA system (refer to Appendix A.4.1) the authors were able to obtain rms vertical velocity profiles from the bottom of their cell to the midplane (there were unable to record above the midplane due to the orientation of their system optics). It was found that the measured values of the rms vertical velocities appeared

to agree (within the predicted depth) with an one-third power variation with height predicted by Kraichnan (1962, as referenced in Garon and Goldstein's paper).

The most relevant study to this investigation is described in a paper by Steinberner and Reineke (1978). These authors presented the results of an analytical and experimental investigation of natural convection in a fluid enclosed in a rectangular cavity and containing heat sources. In the experiment water was heated by passing an alternating current from the horizontal plates through the fluid. The equipment possessed a large amount of flexibility in that both the horizontally-oriented electrodes and the lateral side-walls incorporated cooling channels that allowed the authors to explore the influence of several sets of boundary conditions. Both the case where the vertical walls had the same temperature, upper and lower walls adiabatic, and the situation where all of the walls were cooled to the same temperature were studied. The temperature field in the turbulent boundary layers next to a vertical wall and the local heat flux were determined using holographic interferometry. Measurements of velocities in the turbulent boundary layer of a vertical wall were made using a dual-beam LDA system. The authors obtained both vertical-velocity profiles and rms velocities in the boundary layer. For the laminar boundary layer the velocity profiles that were obtained agreed well with the theory of Ostrach (1952, as referenced in Steinberner and Reineke's paper).

1.3 Objectives of This Investigation

The main objectives of this investigation were two-fold: (1) to develop and test an operational LDA system, and (2) to apply the LDA system to the measurement of absolute vertical-velocities in a horizontal, internally-heated fluid layer with unequal boundary temperatures. The measurements of vertical velocities in the fluid layer for various Rayleigh numbers will provide for the first time an experimental check of the validity of the assumptions of the Baker, Faw, and Kulacki model described in Section 1.1.

2.0 EXPERIMENTAL APPARATUS

The description of the experimental apparatus presented in this section is divided into two parts: (1) a description of the convection cell apparatus, and (2) a description of the LDA system. The convection-cell system is discussed first, inasmuch some of its features dictated a few of the design requirements used in the development of the LDA system.

2.1 Convection Cell Apparatus

The convection cell and associated instrumentation were assembled originally and used by Boon-Long (1978). A block diagram of the total system is depicted in Fig. 3. The general features of the convection cell itself is depicted in Fig. 4. As shown in Fig. 4 the fluid boundaries are defined by copper plates in both the upper and lower plate assemblies. The length of the spacers is a variable quantity that depends on the desired fluid-layer depth (available spacer lengths ranged from 2.54 cm to 20.32 cm). The spacers are made from three phenolic-glass tubes that are cemented together and cut to the desired length within a tolerance of 0.00254 cm. The four sidewalls of the convection cell are made of 1.27 cm-thick glass. The cell is placed in a 50.8 cm x 50.8 cm x 50.8 cm wooden box that is filled with styrofoam fill for thermal-insulation purposes. A minimum of 10 cm of styrofoam insulation surrounds the top, bottom, and sides of the cell. Two openings in the wooden box allow the scattered and unscattered laser-light to pass through the cell to the LDA collection-

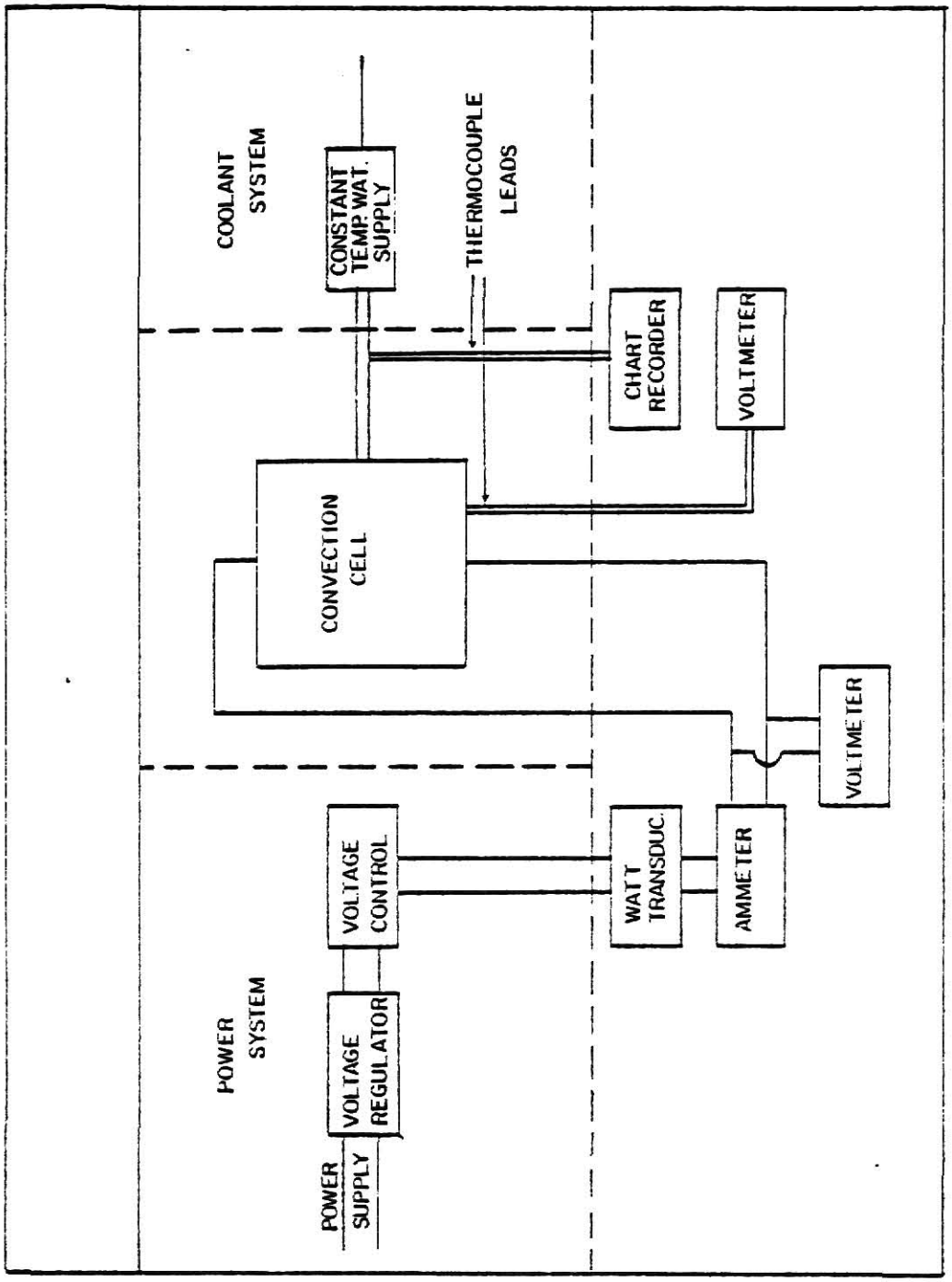

Fig. 3. Block Diagram of Convection Cell Apparatus (from Boon-Long, 1978).

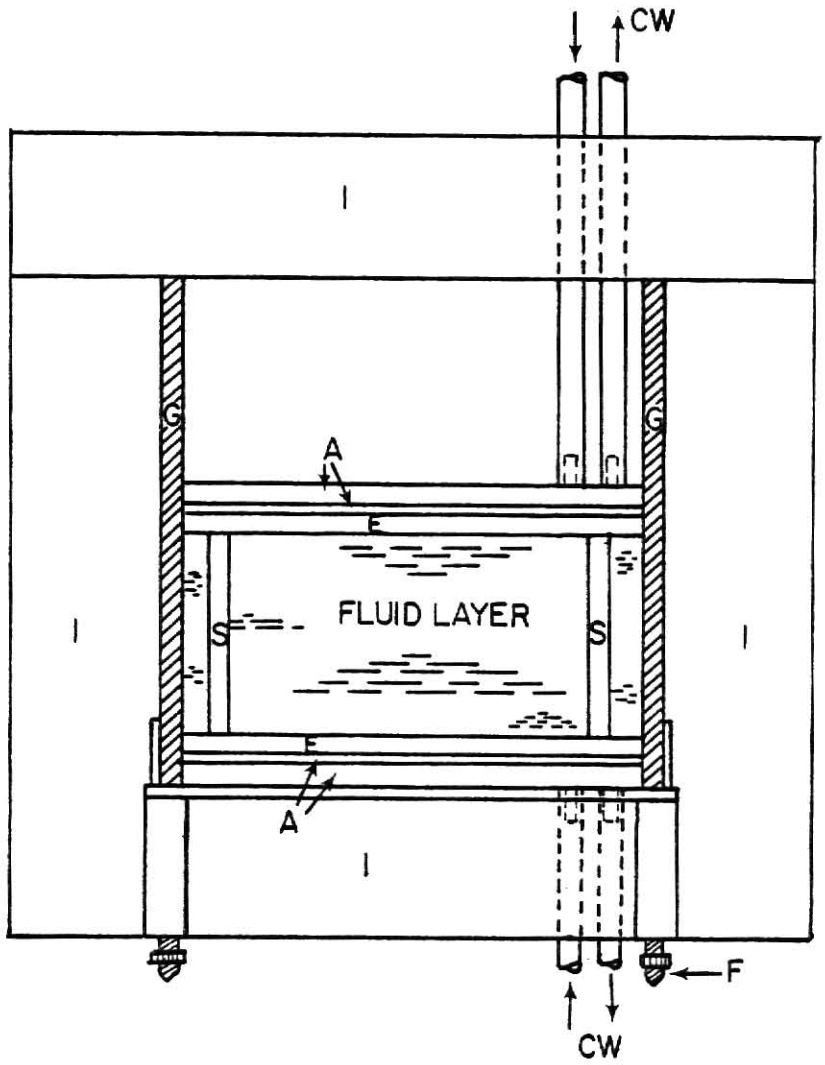

LEGEND

A —— ALUMINUM
CW —— COOLING WATER
E —— COPPER ELECTRODE
F —— ADJUSTABLE FEET
G —— GLASS SIDEWALL
I —— INSULATION
S —— SPACER

Fig. 4. General Features of the Convection Cell (from Boon-Long, 1978).

optics assembly. These openings measure 5.08 cm (length) by 12.70 cm (height), and are lined with styrofoam sheets to the glass sidewalls of the convection cell so that the styrofoam fill present in the wooden box does not interfere with the transmission of the laser beams through the cell assembly.

Each copper plate measures 1.27 cm thick and, as originally machined, are flat to within 0.00508 cm. Due to repeated use, both copper plates showed evidence of etching; thus some deviation from this original specification was unavoidable. Two aluminum plates, cut from 6061-T6 aluminum-plate stock, are attached to each copper plate (see Fig. 5) forming a plate assembly. The side dimensions of the lower plate-assembly measure 25.4 cm by 25.4 cm, while the sides of the upper plate-assembly measure 0.00762 cm less to allow easier movement of this plate assembly in and out of the cell. The thickness of the aluminum plate is 1.27 cm thick. The second aluminum plate of each plate assembly also has cooling channels machined into it in a double-pass pattern (see Fig. 6). The cooling channels are 1.905 cm wide and 0.7938 cm deep. To prevent leakage between the aluminum plates a silicone rubber cement is applied between the plates. Electrical insulation between the copper plate and the first aluminum plate is provided by a 0.0127 cm-thick mylar film.

As constructed by Boon-Long, a total of thirty-six thermocouples are installed in both plate assemblies to monitor temperatures. Nine copper-constantan thermocouples are used in each copper plate, while nine iron-constantan are used in the aluminum plate directly next to a

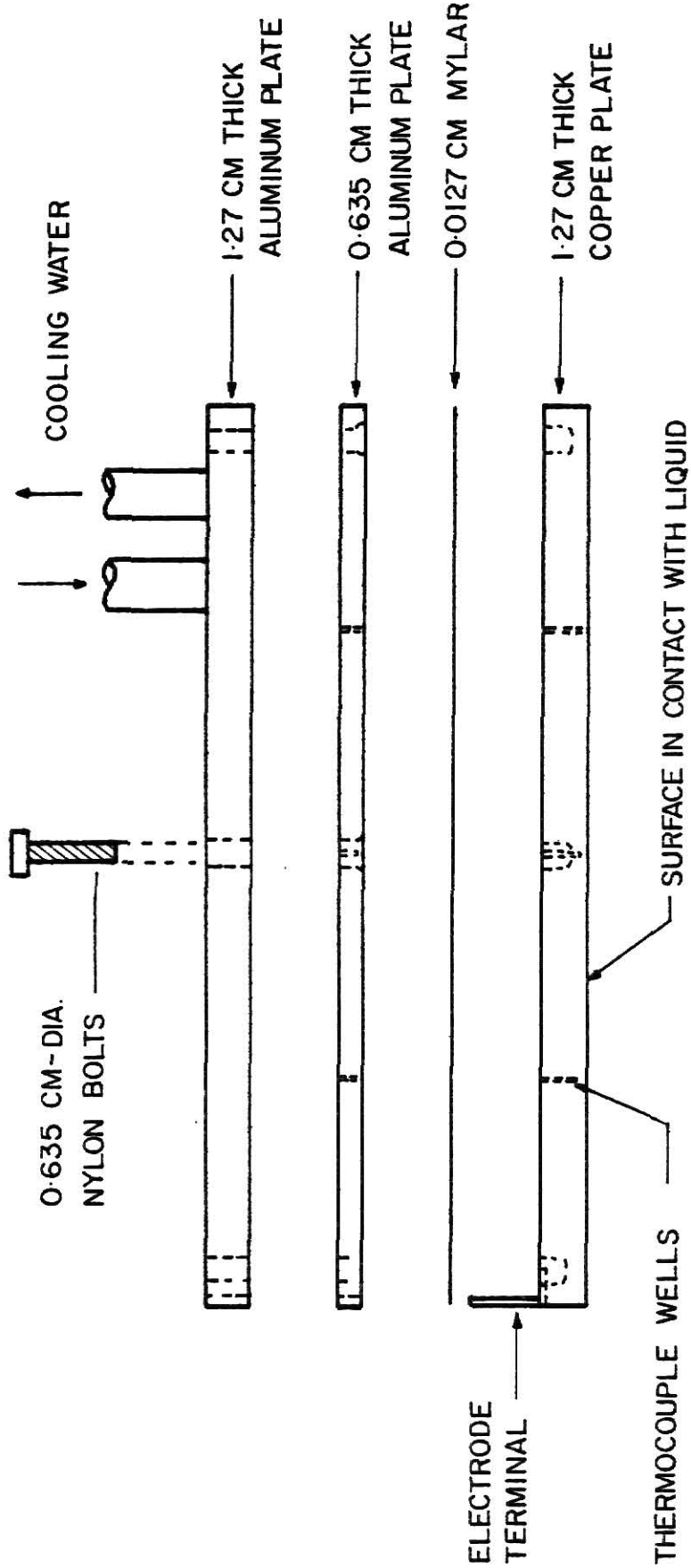

Fig. 5. Schematic of Convection Cell Plate Assembly (from Boon-Long, 1978).

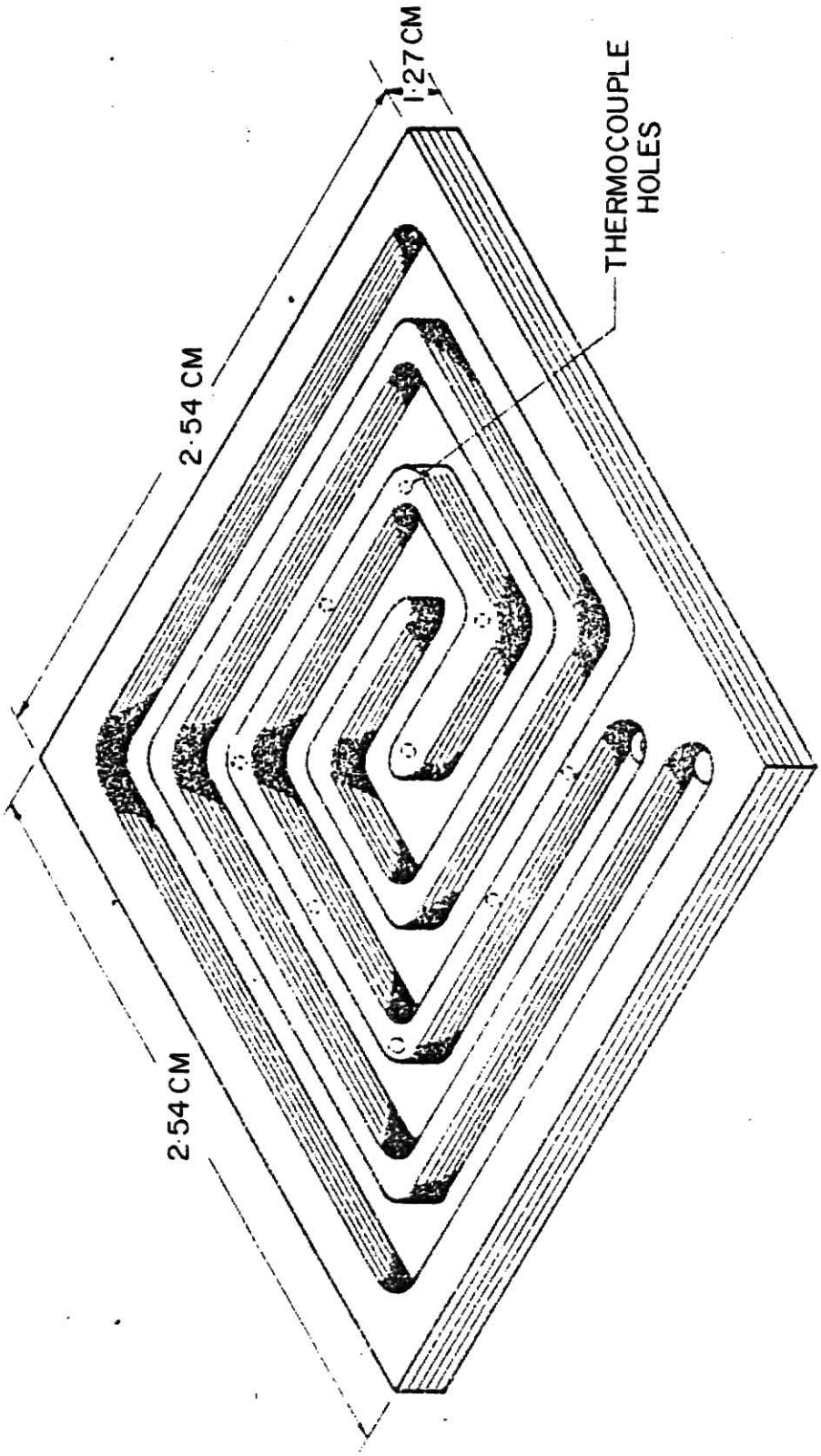

Fig. 6. Convection Cell Aluminum Plate Channels (from Boon-Long, 1978).

copper plate. In each plate the thermocouples are placed in rows of three, symmetric about the center of the plate. Thermocouple leads are extended out of the cell through shallow grooves along the interfaces of the plates. The positive leads are routed through a 10-point selecting switch, while the negative leads are connected to a common junction. All temperature measurements are made with a Keithley Model 179 TRMS digital voltmeter.

During actual operation of the cell it was found that not all of the thermocouples worked. The minimum number of functional thermocouples was found to be three (both copper plates), while each aluminum plate had at least six functional thermocouples. The variations in the temperature readings obtained from the good thermocouples in a plate generally varied less than five percent; therefore, an average of the temperature readings obtained from each plate was believed to represent a valid average-temperature for that plate. For this reason no attempt was made to replace the non-functional thermocouples.

The water that is used to maintain the temperature profiles in the upper and lower plate-assemblies is from the building supply. One plate-assembly receives cold water only, while the other plate-assembly receives warmer water. The warmer-water temperature is monitored to detect fluctuations in the water temperature. The monitoring is accomplished by inserting a copper-constantan thermocouple into the output water from the affected plate-assembly, and

monitoring the resultant electromotive force (emf) developed with a Varian Model G-1000 strip-chart recorder. By keeping the water flow-rate sufficiently high, small fluctuations in the water temperature have a negligible effect on the boundary temperature (Kulacki, 1971, as quoted in Boon-Long, 1978), and are not detected by the Varian recorder.

Internal heating of the fluid is provided by Joulean heating in which an alternating 60-hz current is passed through an electrolytic solution. The electrolytic solution is created by adding relatively small amounts of 0.13 molar solution of copper sulfate to the distilled water that composes the fluid layer. The quantity of copper-sulfate solution that is added ranges from approximately 1 ml for the 5.08-cm layer height to approximately 400 ml for the 20.32-cm layer height.

The power input to the fluid is monitored with a F.W. Bell watt transducer (Model PK-2202B) that has a 0.5% rated accuracy at the rated power level of 2000 watts. As described in Boon-Long (1978), the transducer utilizes a Hall generator (a magneto-sensitive semi-conductor) to generate a voltage proportional to the product of the load current and the magnetic field. The output from the watt trans-ducer (a dc millivolt output proportional to the input power to the cell) is monitored by a Keithley Model 179 TRMS digital voltmeter.

More specific details on the design and construction of the con-vection cell and associated instrumentation is found in the Ph.D. dissertation by Boon-Long (1978).

2.2 LDA System

The design and construction of the LDA system used in this study is presented in this section. There were two overriding design constraints imposed by both the scope of the intended study and by the nature of the convection cell. The first constraint, imposed by the scope of the intended study, was that since only the vertical-velocity component was to be measured, it was only necessary to design and build a one-component LDA system. The second constraint, imposed by the nature of the convection cell, was that the absolute velocities of the velocities to be measured were low. In comparable velocity studies carried out by Steinberner and Reineke (1978) and Garon (1973), the values of the absolute velocities reported were generally less than 10 mm/sec. This lower range of velocities and the fact that the velocity could go to zero imposed special requirements on the LDA system. These requirements are more fully discussed in the following pages of this section.

2.2.1 LDA-Optics Design and Components

Figure 7 depicts the design of the LDA optical-configuration employed in this study. One of the first decisions that is made in a velocity study that involves the technique of LDA is the choice of optical configuration to use (see Appendix A.4). The configuration selected for use in this study is the dual-beam mode in which a single transmission-lens is used to focus the two laser beams to an intersection point (the scattering volume - see Fig. 7) in the fluid layer. There are three reasons for the selection of the dual-beam mode. One

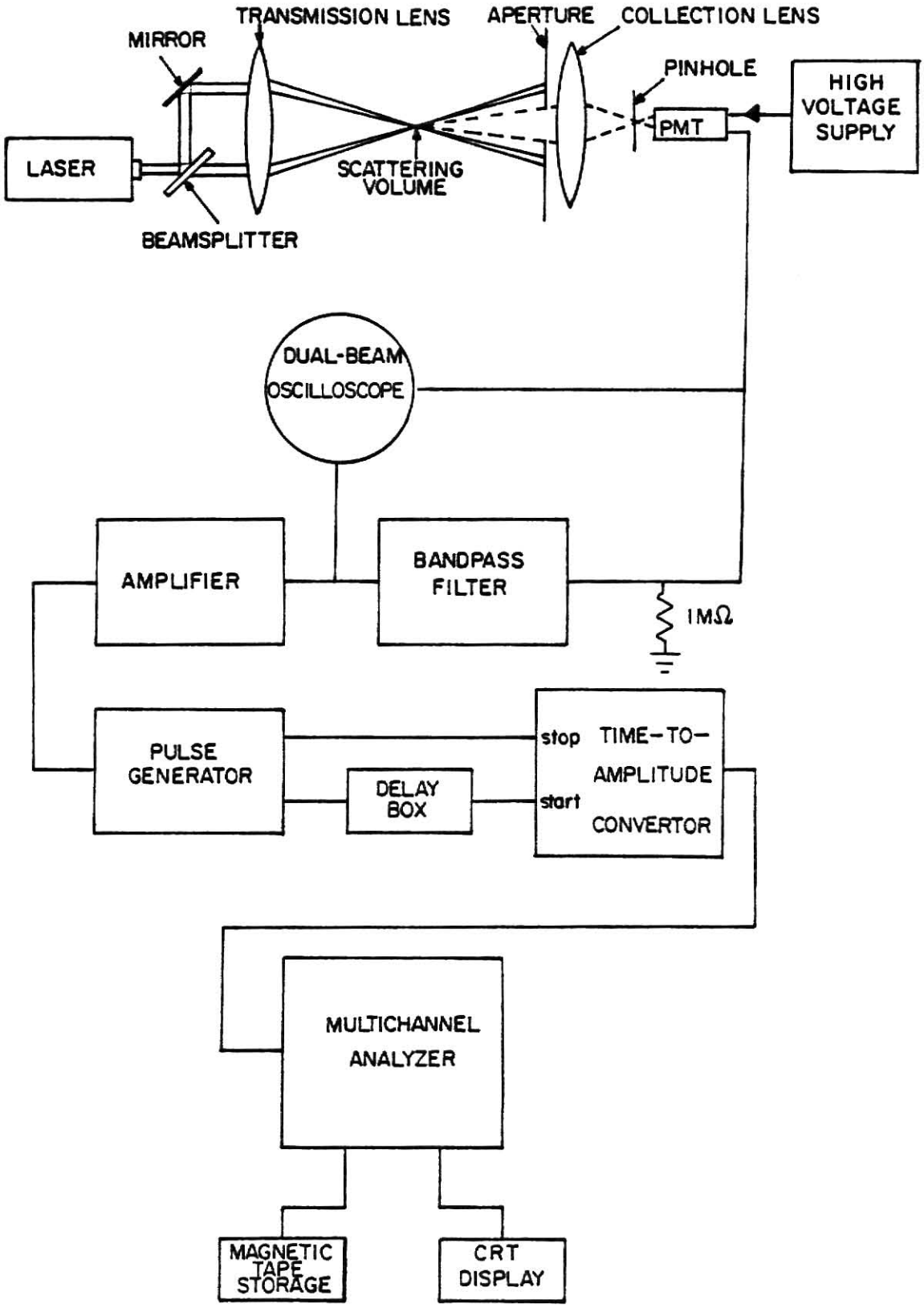

Fig. 7. Block Diagram of Total LDA System.

is ease of alignment - one lens is used to focus the laser beams, thus insuring that the two beams intersect. Because one lens is used to focus the two laser beams, the scattered light from one beam is automatically injected into the scattered light from the second beam. This considerably simplifies the alignment procedure associated with the collection optics. The second reason has to do with the diameter of the receiving aperture - it is larger than that possible with either the reference-beam or dual-scatter modes (see Appendix A.4.2). Thus more of the scattered light can be collected for analysis. The third reason is that the frequency of the Doppler signal (or the velocity component being measured) is independent of the direction of observation by the collection optics (see Appendix A.4.2).

There is a distinct disadvantage associated with the selection of the dual-beam optical configuration. This disadvantage is a result of the requirement to inject both laser beams into the fluid layer. Because it is the vertical velocity component that is to be measured, it is necessary to focus the two laser beams into the fluid in the plane perpendicular to the horizontal plane of the fluid. This limits the amount of vertical travel possible in the fluid layer. This problem is minimized by decreasing to the extent practicable the angle of separation between the two intersecting laser beams.

The laser source used in this study is a Spectra-Physics Model 165 multi-line argon-ion laser. The maximum output of the laser is two watts (all lines). For this study the laser was tuned to 488 nm. At this wavelength the laser has a maximum output of .7 watts (for the

results presented in this study the power level ranged between 40 and 50 milliwatts). The beam from this laser is routed from one end of the laboratory to the opposite end of the room where the LDA system is set up (movement of the laser closer to the LDA system was not allowed as this would have interfered with other experiments being carried out in the room).

The transmission-optics assembly consists of a beamsplitter, mirror, and transmission lens. The beamsplitter is manufactured by Oriel (Model No. A-45-102-4) in which the front surface to the incoming laser beam is coated with Inconel and the back surface is coated with a magnesium fluoride (MgF_2) anti-reflection coating. The incoming laser beam is split into two beams (a reflected beam and a transmitted beam) of approximately equal intensities by the beamsplitter. The reflected beam is then reflected off of a plane mirror such that it travels in a direction parallel with the transmitted beam from the beamsplitter to the transmission lens. The plane mirror is an Ealing aluminized plane-mirror set in a kinematic mount (Model No. 22-8825). The kinematic mount incorporates three thumbscrews that adjust the orientation of the mirror about two perpendicular axes. The transmission lens is a Melles Griot plano-convex lens of diameter 42.0 mm, and focal length 600 mm (Model No. 01 LPX 323). This lens also has a MgF_2 anti-reflection coating to minimize reflection losses.

The collection optics consists of an iris diaphragm, collection lens, pinhole, and a photomultiplier (PM) tube. The iris diaphragm serves two purposes: (1) it blocks the two unscattered laser beams from reaching the receiving lens and thus the PM tube, and (2) it controls the amount of scattered light reaching the PM tube. The collection lens, a Melles-Griot biconvex lens of diameter 50.8 mm and focal lenght 127 mm (Model No. 01 LPX 189), collects the scattered light and focuses it for detection by the PM tube. The iris diaphragm and collection lens are mounted on the ends of an aluminum tube (length 7 cm, diameter 5.5 cm) custom-built for this purpose. The pinhole, whose purpose is to insure that the PM tube sees only laser light scattered from the scattering volume, has a diameter of 203 microns, and is mounted on an iris diaphragm that is in turn attached to the PM-tube housing.

The PM tube is an RCA 1P28, and is used because of its low cost, durability, and good response (S-5) in the spectral region of interest. The quantum efficiency of the 1P28 at 488 nm is approximately 7 percent (quantum efficiency is defined as the number of photoelectrons emitted from the photocathode per incident photon). The PM tube is enclosed in a light-tight Jarrel-Ash single photomultiplier-tube housing (Model No. 83-021). The PM tube is mounted in an eleven-pin socket that is provided with the PM-tube housing. A voltage-divider network is attached to the base pins of the socket in which ten 1-megohm resistors are employed in the divider network (no capacitors were present in the circuit). The supply voltage for the PM tube is obtained

from an Ortec high voltage power supply (Model 456).

All components in the transmission and collection-optics assemblies are mounted in Ealing lens holders, pillars, and bases. Ealing optical benches are used in the placement of the optical components. Ease of alignment is facilitated not only by the use of the optical benches but also by the use of Ealing vertical-slide pillars (Model No. 22-4089) because the optical components are easily moved up and down.

The collection-optics assembly and transmission lens are each mounted on separate optical benches and placed on a 132 cm x 89 cm x 6.4 cm aluminum slab that rests on top of a table. The aluminum slab is used to minimize the effect of room vibrations on the optical components. Because of space limitations it is not possible to place the beamsplitter assembly directly on the aluminum slab. Instead, this assembly is mounted on a separate optical bench that in turn rests on lead bricks on the same table as the aluminum slab.

One optical design feature not implemented in the construction of the LDA system is the use of a Bragg cell to frequency shift one of the two laser beams that are used to form the scattering volume. A Bragg cell is an acousto-optic device in which an incident light beam is divided into several beams with different frequencies and directions. Bragg cells are either in the form of a solid block of transparent material or a small cell filled with a liquid. In either case plane acoustic waves are created at one end of the cell and are trans-

mitted across the cell at the speed of sound to the opposite end of the cell where these waves are absorbed by a damping material. These waves cause variations in the index of refraction in the material composing the cell; the effect is analogous to a three-dimensional moving diffraction grating (Durrani and Greated, 1977). If the angle of incidence of the incident light is equal to the Bragg angle, nearly all of the light is diffracted into the first order. The light diffracted into the first order in this manner is frequency-shifted by an amount equal to the frequency of the sound wave (Durrani and Greated, 1971).

The advantage of having one of the two laser-beams frequency-shifted in an LDA system is that zero velocity corresponds to the shift frequency. Thus use of a Bragg cell in this study would have proved advantageous for two reasons. The first reason is that the frequency range of the Doppler signals detected by the PM tube would have been increased by an amount equal to the shift frequency. This avoids the unpleasantness of trying to measure low-frequency Doppler signals in the presence of background low-frequency noise, and also allows easier separation of the Doppler portion of the signal from the pedestal component of the signal (see Appendix A.7). The second reason is that it provides directional information about the flow field. Scattering particles traveling in one direction result in a PM-tube signal frequency equal to the magnitude of the Doppler shift plus the shift frequency, while scattering particles traveling

in the opposite direction result in a PM-tube signal frequency equal to the shift frequency minus the Doppler shift (Mazumder, 1970).

A Bragg cell was purchased for use in the LDA system developed for this study, but it was not used because of signal detection problems. Most, if not all, commercial Bragg cells have a frequency shift equal to 40 Mhz. This frequency shift was not detected when the Bragg cell was incorporated into the system, because the high-frequency signal was being filtered out by stray capacitance present in the signal line from the anode of the PM tube to the bandpass filter. In a private communication with L. Crosswy of ARO, Inc., it was determined that the voltage-divider network needed renovation, and a high-frequency amplifier was also required before the band-pass filter. For these and other reasons it was determined the time was not sufficient to accommodate the use of a Bragg cell in this study.

2.2.2 LDA Signal-Analysis Instrumentation

The method of signal analysis employed in this study is period timing in which a measurement is made of the period of the Doppler signal that is detected by the PM tube. A block diagram of the instrumentation system is given in Fig. 7. This system is based on a similar system that is described in a paper by Maynard, Gaylord, and Rust (1975).

The signal from the PM tube is first fed into a bandpass filter. The filter serves two functions: (1) it removes the low frequency

or "pedestal" component of the signal (this is the unmodulated portion of the total signal from the PM tube - see Appendix A.7), and (2) it removes any unwanted high-frequency noise. For this study an active bandpass filter had to be designed and built. The circuit design, given in Fig. 8, is based on designs provided in a book on active-filter design and construction by Lancaster (1975). This bandpass filter design is actually a high-pass filter followed by a low-pass filter. For the design given in Fig. 8 the cutoff frequency of the high-pass filter is 100 hz while for the low-pass filter it is 10,000 hz (the cutoff frequency is defined as the point at which the filter response drops by 3 of its peak value on the way out of the filter passband). The cutoff frequency is adjusted by scaling the capacitors in Fig. 8 (e.g., doubling the capacitor values reduces the cutoff-frequency by a factor of two). Power for the bandpass filter is supplied by a Heathkit Electronic design experimenter.

The output from the bandpass filter is unsuitable for use as a timing signal because the pulse width is too large; therefore the timing signals are derived from the amplifier-pulse generator combination shown in Fig. 7. The signal from the bandpass filter is amplified by a Princeton Applied Research (PAR) Model 24 amplifier. Following the amplification process the signal is applied to the external-trigger input of a Datapulse Model 110B pulse generator. For every positive transition of a preset threshold the pulse generator produces a negative-voltage signal that has an amplitude of approximately one volt and a small width ($\sim$ 50 nsec). The input signal to the

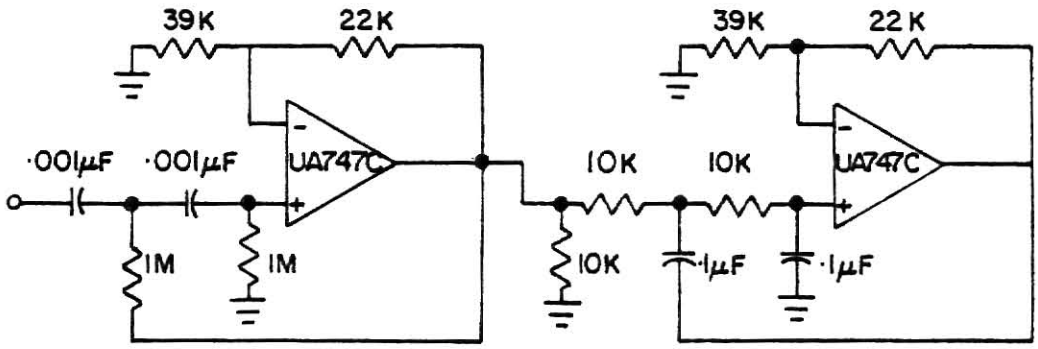

Fig. 8. Bandpass Filter Circuit Diagram.

pulse generator has to be at least 1.25 volts, or the trigger will not activate. Since the input signal is continuous and of varying amplitude (see Appendix A.7.1), a zero-crossing detector should have been employed in the generation of timing signals (one was not available that would work for the range of Doppler-signal frequencies encountered in this study). To minimize the problem of the finite-trigger threshold encountered with the use of the Datapulse pulse generator, the input signal is amplified as much as possible using the PAR amplifier.

Each negative-voltage timing signal generated by the pulse generator is divided into two equal signals and applied to the start and stop inputs of an Ortec Model 437A time to amplitude converter (TAC). One signal is delayed approximately 32 nsec with respect to its counterpart using an EG&G delay box (Model DB-263). The undelayed signal is applied to the stop input of the TAC while the delayed signal is applied to the start input of the TAC. The timing sequence of the TAC is activated at this point, and ends with the application of the next stop signal that is generated by the next positive-going threshold crossing at the trigger input of the pulse generator. The subsequent delayed signal that is applied to the start input of the TAC is ignored. The output signal from the TAC is a bipolar signal of constant shape, the amplitude of which is proportional to the instantaneous period of the Doppler signal from the PM tube.

The TAC has a range switch and a range multiplier that determine the range of signals that can be analyzed by the TAC. For example, if the range switch is set at .4 μsec and the range multiplier is set at x 100, the largest time difference (or signal period) that can be measured by the TAC is 40 μsec. For the TAC model that is used in this study it is necessary to change one of the timing capacitors associated with the range multiplier in order to be able to measure the low-frequency Doppler signals that are generated in the convection cell. With this change the x 100 range multiplier is increased to approximately x 33,000, thus enabling the TAC to measure signals with frequencies as low as 37 hz.

The signal from the TAC is next analyzed for the amplitude information by a Canberra Model 8180 Intelligent Multichannel Analyzer. This system contains an amplifier, multichannel analyzer (MCA), and microprocessor. The MCA has among other features an analog-to-digital convertor (ADC) and a maximum of 4096 memory locations. The signal from the TAC is applied directly to the ADC input where it is converted into a digital value that is proportional to the input-signal amplitude. This digital value is then used to select a particular memory location to increment. Thus the channel locations in the MCA act as a digital representation of a linear scale in which channel one represents some maximum frequency while channel 4096 corresponds to the smallest possible frequency that can be measured by the TAC (which is determined by the range setting).

The MCA also has a cathode-ray tube (CRT) that is used to display visually the contents of the memory locations. This information is also

transferred to a 9-track tape for later analysis by a computer. The tapewriter is a Canberra Model 8531A Magnetic Tape Controller (the tapewriter serves as the interface between the MCA and the tape unit), while the tape drive is a Pertec Model 7820-9 Magnetic Tape Unit.

3.0 PROCEDURE

Because one of the major facets of this study was the development of an operational LDA system, the LDA development procedures described in this section are necessarily detailed and somewhat tedious. This section also describes the procedures involved in operating the convection cell, obtaining velocity measurements in the convection cell, and evaluating the experimental results. In order to cover the necessary material in an organized format this section is divided into five parts, with the first part dealing with the calibration of the LDA signal-analysis instrumentation.

3.1 Calibration of the LDA Signal-Analysis Instrumentation

Calibration of the LDA signal-analysis instrumentation involved the application of a signal with a known and constant frequency (refer back to Fig. 7). Because the signal frequency was constant, only one channel location in the MCA memory was preferentially incremented as the signal was being applied (the location of which depended on both the signal frequency and on the TAC range-setting). Measurement of several different frequencies allowed a calibration (or curve fit) of frequency vs. channel number to be made for the particular TAC range used.

The source of the continual and constant-frequency signals for this calibration procedure was the pulse generator in the signal-

analysis system (refer to Sect. 2.2.2). Instead of being operated in the trigger mode (as it is for the generation of timing signals when LDA signals are being analyzed) the pulse generator was switched to the continuous-frequency mode for the calibration procedure, and it was this output signal that was applied to the start and stop inputs of the TAC.

Inasmuch as the calibration procedure depended on an accurate frequency value for the continuous-signal output from the pulse generator, a determination of this frequency was made using the MCA as a frequency counter. The positive output from the pulse generator was applied directly to the ADC input of the MCA. Next the analyzer was set to count for a preset time, and the number of signals was recorded. At least five different recordings were taken for each frequency setting of the pulse generator, from which an average count total was recorded. The frequency was determined easily since the total counts and count-time were known.

It is important to note at this point that whenever the MCA was used it was operated in the live-time mode. In this mode the MCA compensates for the ADC dead time (this dead time is the time the ADC is unavailable to analyze input signals because it is still processing a previous signal). Thus in the live-time mode the analyzer collects signals for the preset time and the resultant count total is not affected by the analyzer dead time.

Once an accurate determination of the frequency had been made, the negative-output signal from the pulse generator was applied to

the delay box-TAC instrumentation. The resultant output signal from the TAC (a signal whose amplitude is proportional to the frequency of the signal that is applied - see Sect. 2.2.2) was then applied to the ADC input of the MCA. The channel location that was being continually incremented was noted with the use of the CRT display capability of the MCA.

The above procedure of determining accurately the frequency of the signal output from the pulse generator and the subsequent determination of the corresponding channel location in the MCA memory was repeated at least ten times for each TAC range measured. Once a sufficient amount of data had been collected for the TAC range the range setting was changed, and the entire calibration procedure was repeated.

After all of the data had been taken the resulting data points were plotted on a graph of frequency vs. channel number. The results for the two TAC ranges used exclusively in this study are given in Figs. 9 and 10 (note that only 532 MCA channel locations were utilized). It is quite clear from these graphs that the analysis capabilities of the TAC is linear only in certain narrow frequency ranges. A satisfactory curve fit for these two plots was not obtained for either an exponential or polynomial fit. It was then decided to plot the data on a graph of the natural logarithm of frequency vs. the natural logarithm of channel number. The results are given in Figs. 11 and 12. A straight-line fit was obtained for

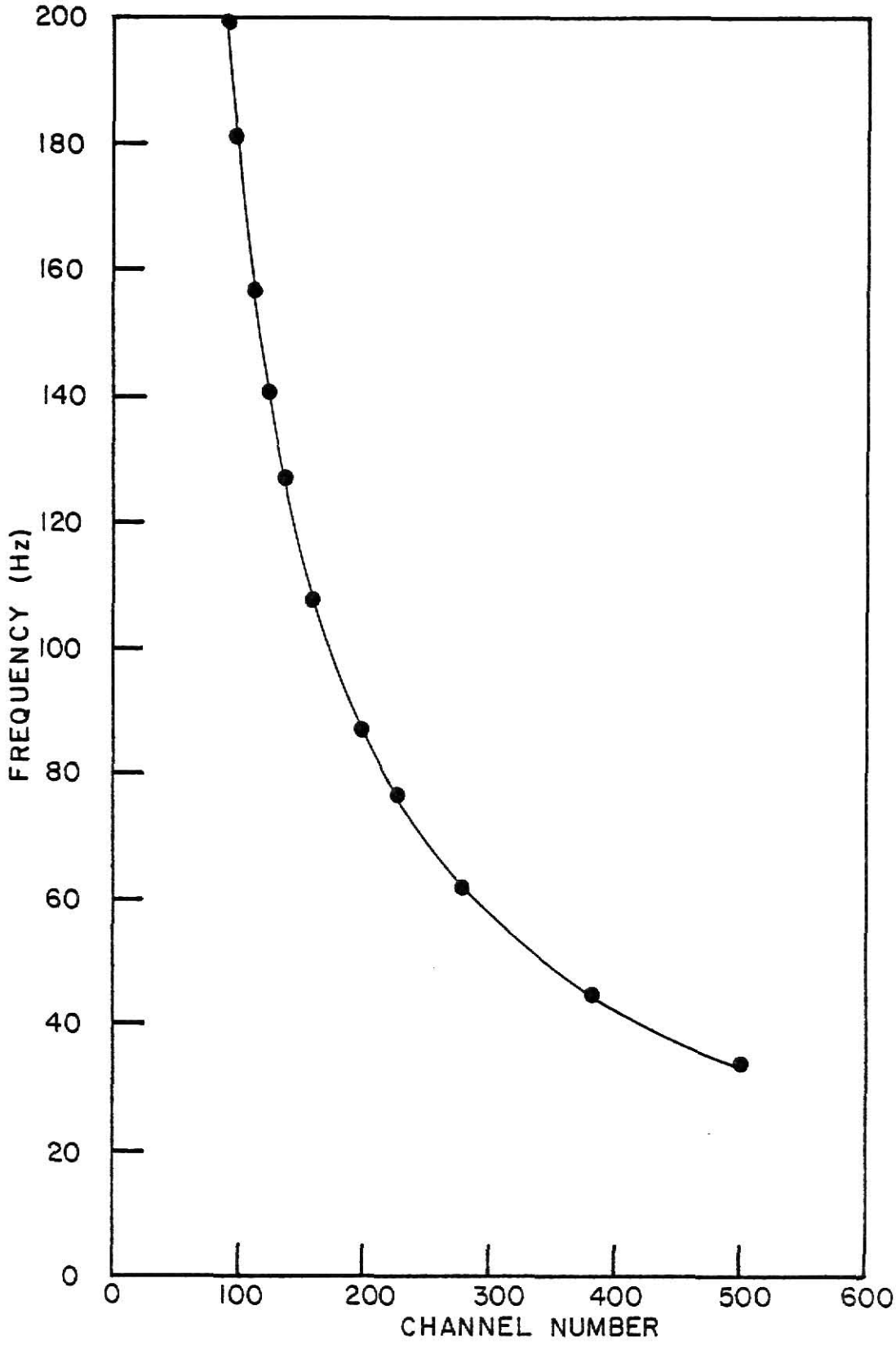

Fig. 9. Plot of Frequency vs. Channel Number for .03-sec TAC Range.

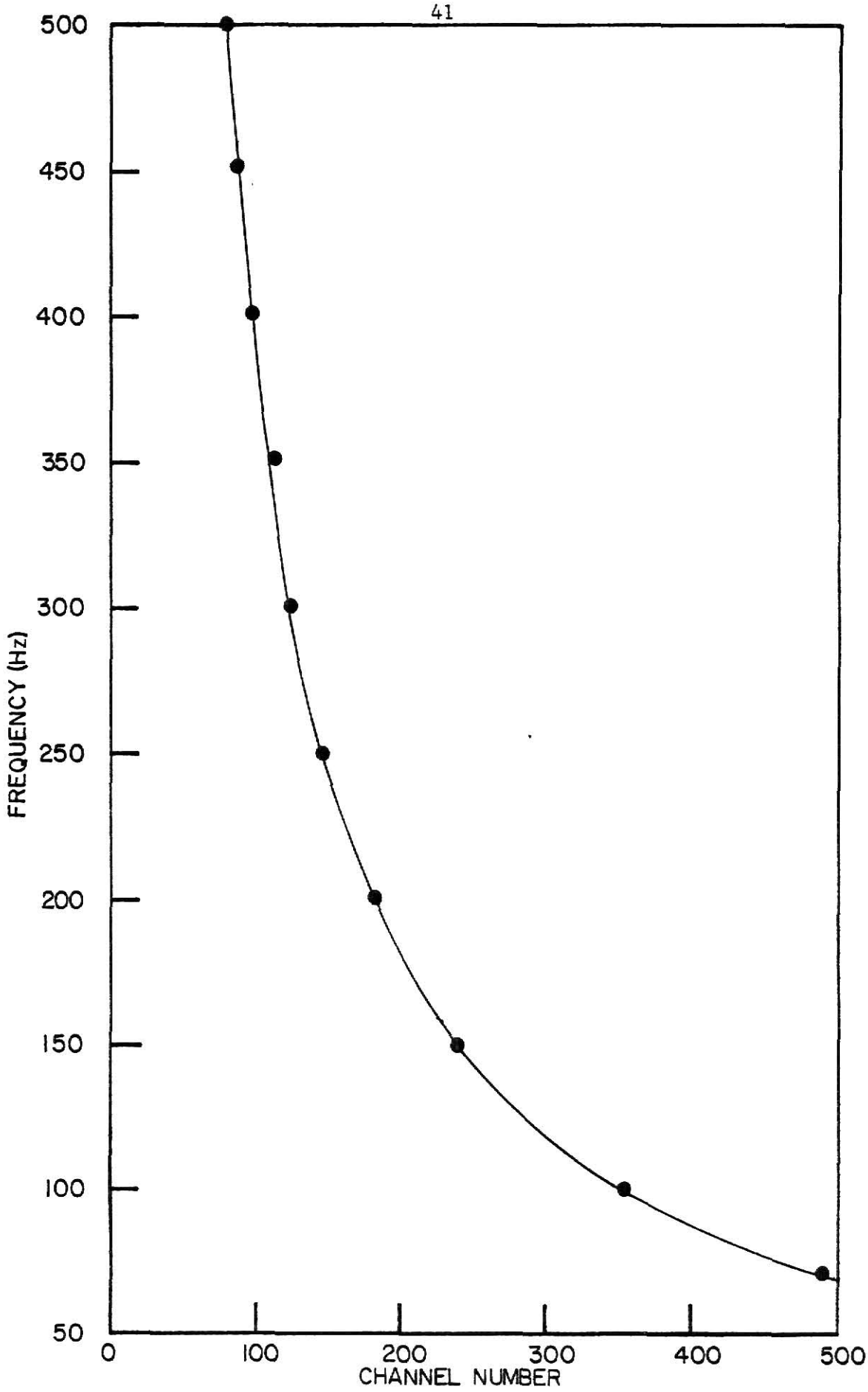

Fig. 10. Plot of Frequency vs. Channel Number for .01-sec TAC Range.

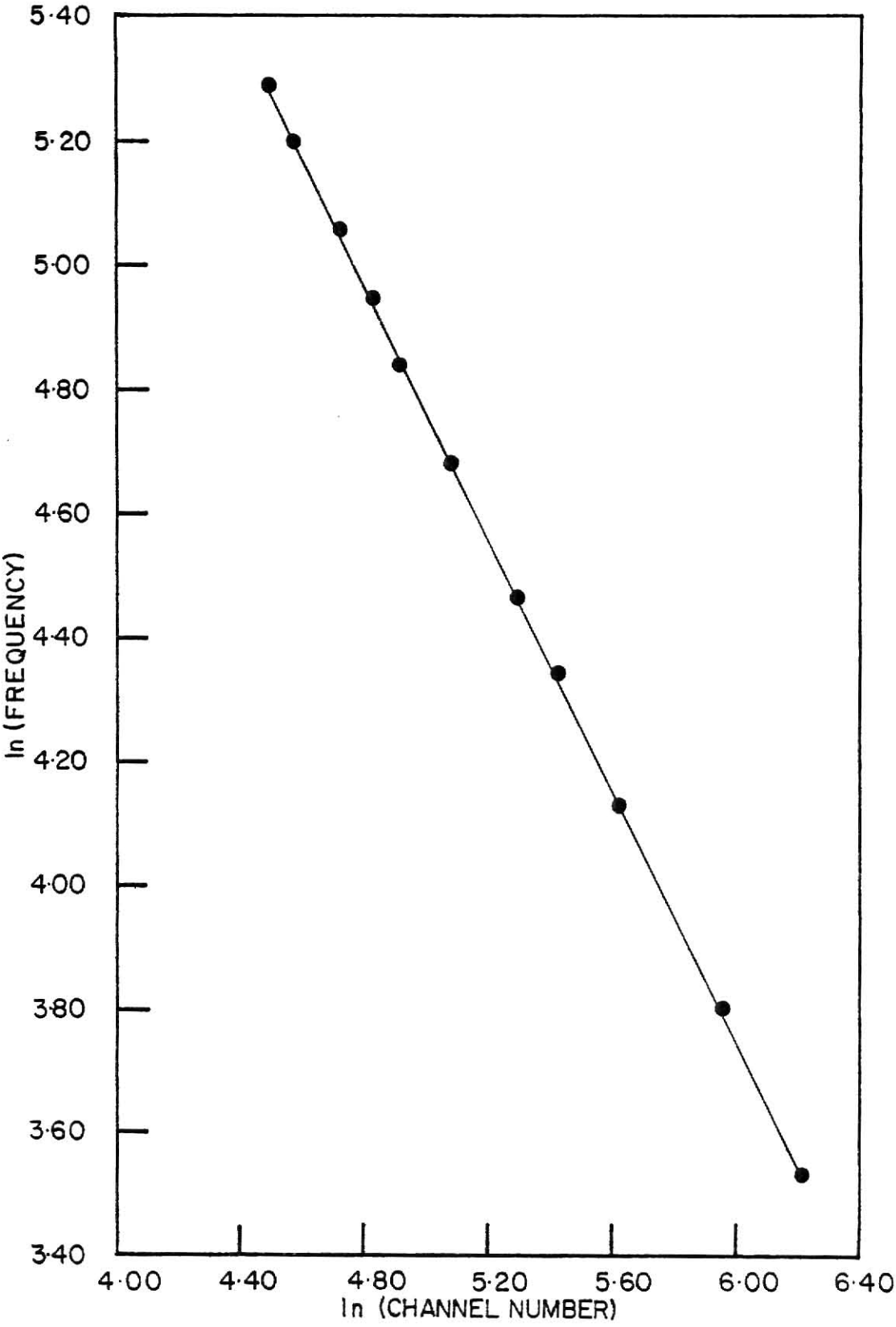

Fig. 11. Plot of ln (Freq.) vs. ln (Ch. No.) for .03-sec TAC Range.

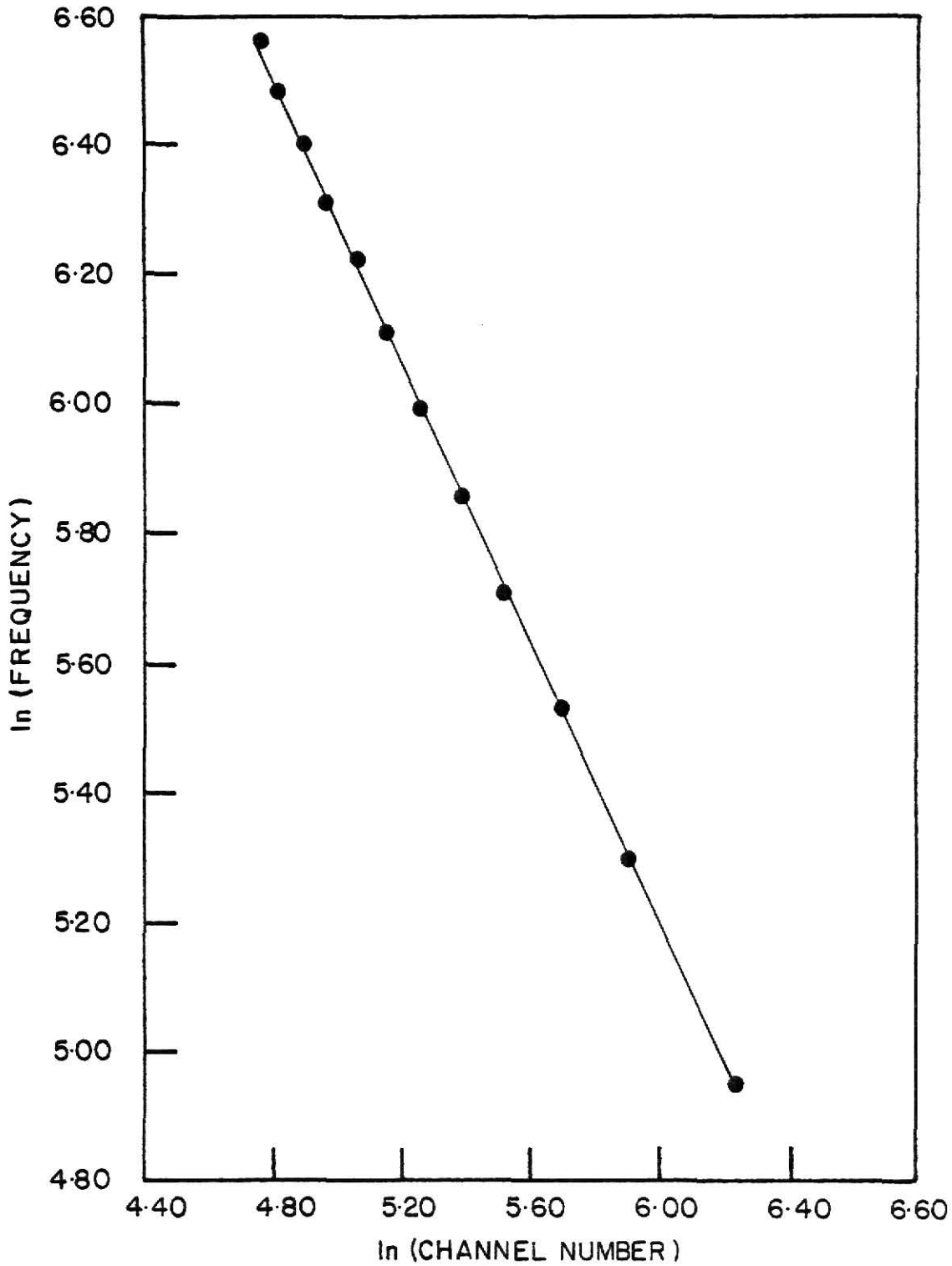

Fig. 12. Plot of ln (Freq.) vs. ln (Ch. No.) for .01-sec TAC Range.

these two plots using the computer program POLFIT (for details see Appendix B). Thus for the .03 sec TAC range the MCA frequency calibration was

$$\ln (\text{freq.}) = 9.871 - 1.021 \ln (\text{ch. no.}) , \qquad (5)$$

while for the .01 sec range the calibration was

$$\ln (\text{freq.}) = 10.872 - 1.067 \ln (\text{ch. no.}) . \qquad (6)$$

The two calibrations given in Eqs. (5) and (6) were checked by two different methods. The first was to calculate the maximum percentage-deviation between the true frequencies and the frequencies generated by the curve fits. For Eq. (5) the maximum deviation was .60% while for Eq. (6) it was 2.0%.

The second method involved an evaluation of the correlation coefficient, r. In this case r is a measure of the degree of linearity between the natural logarithm of the frequency and the natural logarithm of the channel number. Simply, the closer r^2 is to one, the better the calculated curve-fit (or regression line) correlates the data points (Bajpai, Mustoe, and Walker, 1977). A Hewlett-Packard (HP) linear regression program was used in conjunction with a HP-25 programmable calculator to evaluate the r^2 values. Use of this program yielded the same coefficients as those in Eqs. (5) and (6) (to three decimal places) and r^2 values of .99993 for Eq. (5) and .996 for Eq. (6). With these r^2 values and the low maximum percentage-deviations mentioned previously, Eqs. (5) and (6) were considered satisfactory curve fits.

3.2 Alignment of LDA Optics

The first alignment of the LDA optics was of the transmission optical-components in the formation of a scattering volume (see Fig. 13). To simplify this alignment (and the alignment of the collection optics) all optical benches were leveled using a liquid level before any optical components were mounted. Benches were adjusted using computer cards as shims until they were level.

The next step was to mount the laser. For the initial set of LDA measurements a helium-cadmium laser (Liconic Model 4110) was used as the light source. It was mounted on the arm of a milling machine which was in turn mounted on a separate table adjacent to the table supporting the aluminum slab and optics. The milling machine provided the option of moving the laser vertically, and it was heavy enough to damp out most of the room vibrations that could affect the laser. The laser was leveled in a fashion similar to the aforementioned optics.

The beamsplitter-mirror combination was installed next. The orientation of the beamsplitter relative to the incoming laser beam was adjusted to be about 45°. The mirror was then mounted, and a coarse adjustment was made of the orientation of the mirror surface (using the three thumbscrews) such that the reflected beam from the mirror traveled a parallel path with the transmitted beam from the beamsplitter. It should be mentioned at this point that the path traveled by the transmitted beam from the beamsplitter was never adjusted. Instead, any adjustments in the formation of the scattering volume were made with the reflected beam from the mirror.

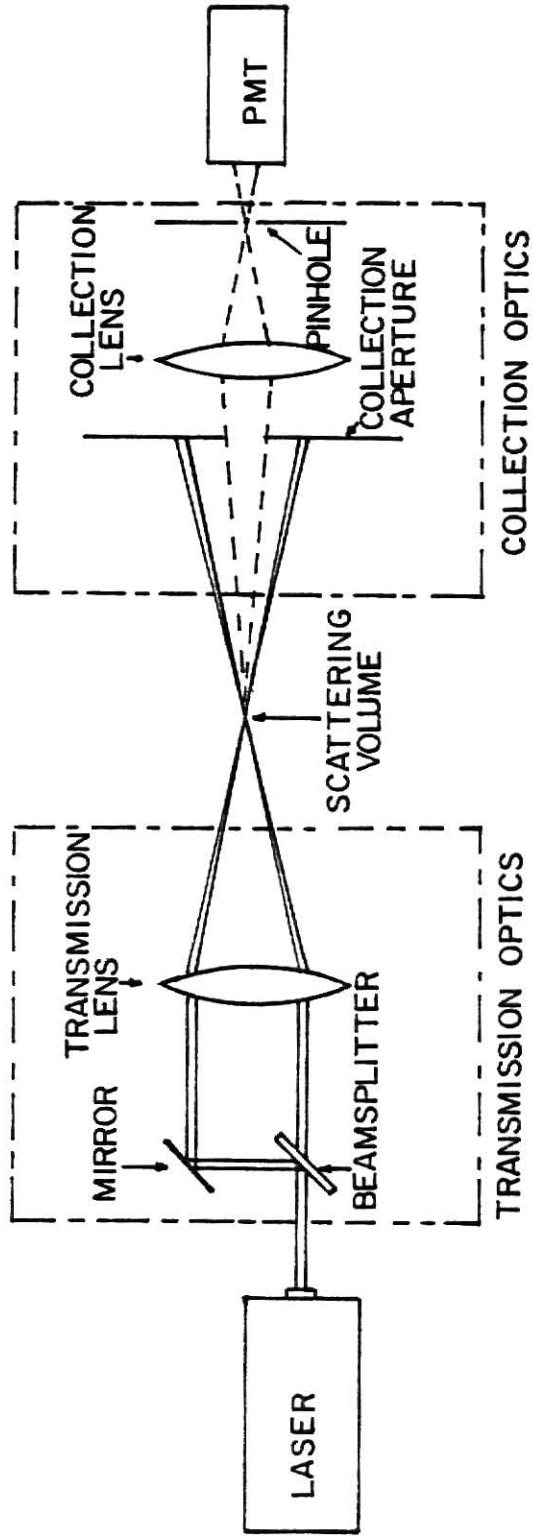

Fig. 13. Schematic of LDA Optical Configuration.

The transmission lens was installed next. With the transmission lens in place the scattering volume was reasonably well defined. According to the criteria established in Sect. 2.2.1 for the maximum possible vertical travel of the scattering volume in the convection cell, the separation between the two beams from the beamsplitter-mirror combination was next minimized as much as possible with the adjustment of the vertical positions of the mirror and beamsplitter relative to each other.

At this point final adjustments were made to better define the scattering volume. A plano-convex lens was mounted in a lens holder and placed on the same optical bench as the transmission lens. This lens was placed behind the transmission lens with respect to the incident beams, and moved along the optical bench to the location of the scattering volume (this being possible since the convection cell was not yet in place). With the plane face of the plano-convex lens forming the incident surface for the incoming beams, a reflected image of the scattering volume was projected to the room wall opposite the lens. In this manner an expanded image of the scattering volume was obtained. Visual inspection of the expanded image allowed fine adjustments to be made with the mirror such that the two beams forming the scattering volume coincided exactly.

An added benefit of obtaining an expanded image of the scattering volume was that the fringe pattern formed in the scattering volume

was that the fringe pattern formed in the scattering volume (see Appendix A.4.2) was clearly shown. Thus the effects of any room vibrations were easily seen by noting shifts in the fringe pattern. Because the velocities to be measured were low, it was necessary to minimize the effect of room vibrations on the optics since these vibrations cannot be distinguished from the Doppler-shift frequencies of the same order of magnitude. Judicious placement of lead bricks on the table containing the optics helped to minimize greatly vibration problems.

Once a satisfactory scattering volume was formed, the distance between the transmission lens and the plano-convex lens was measured and recorded. A measurement was also made of the beam separation at the transmission lens and recorded. These two quantities were then used in the calculation of θ, the half-angle of separation between the two beams at the scattering volume (in air).

Alignment of the collection optics was similar for either the rotating glass plate or the convection cell. For the rotating glass plate the aperture opening was centered symmetrically between the two laser beams emerging from the scattering volume. An image of the scattering volume was then projected by the collection lens. The PM tube was moved along the optical bench containing the collection optics until a focused image of the scattering volume was formed at the pinhole.

For the convection cell there was a greater problem with spurious light reaching the PM tube (spurious light is defined as light emanating from sources other than the scattering volume). The primary source of this spurious light was scattering from the laser beams due to the presence of a suspended particulate in the fluid layer. To minimize this problem and to help better locate the scattering volume, the collection optics were moved slightly off-center. This enabled the scattering volume to be more clearly seen in relation to the laser beams forming the scattering volume.

3.3 Testing of the LDA System - Rotating Glass Plate

To check the calibration procedure outlined in Sect. 3.1 the tangential velocities of a slowly-rotating glass plate were determined. The glass plate was coated with dust particles, which served as scattering particles when the glass plate rotated through the scattering volume. The glass plate was attached to a Bristol Model 350 motor that had a constant angular speed of .4 rev/min (this angular speed was checked several times and very good agreement was found between the specified magnitude and that actually measured.

In order to insure that an accurate measurement was made of the tangential velocity it was necessary to align the glass plate such that the dust particles traveled through the scattering volume in a direction perpendicular to the fringe pattern. The scattering volume was focused on the glass surface closest to the transmission lens.

Once the rotating glass plate was properly positioned in the scattering volume, a measurement was made of r, the distance from the center of the rotating glass plate to the scattering volume. A value for the tangential velocity was calculated using the following equation:

$$V_T = rw \ . \qquad (7)$$

The rotation of the glass plate was started, and a Doppler signal was obtained. To check the authenticity of the Doppler signal an oscilloscope was employed to display the signal. By cutting off one of the two laser beams used to form the scattering volume, authentic Doppler signals disappeared from the oscilloscope display.

Once a signal had been verified as authentic, it was collected and analyzed by the signal-analysis instrumentation. At least 10,000 counts were taken at each radial position measured on the rotating glass plate. Although it was observed that the shape of the peak did not vary appreciably after 10,000 counts, most count totals were between 20,000 and 35,000.

The spectra obtained for each radial position measured was transferred to a magnetic tape for subsequent computer analysis for the tangential velocity. The computer analysis was carried out according to the procedure outlined in Sect. 3.6.1. The results of this testing procedure are presented in Sect. 4.1.

3.4 Convection Cell Operation

To make vertical-velocity measurements in the convection cell, the cell assembly was placed within the optical train and supported by a Newport Research Corporation Model 280 laboratory jack. This jack was designed to carry a maximum of 47.6 to 204 kg over an elevation range of 7.6 to 15.2 cm. The cell was leveled using a liquid level. Adjustments were made with the placement of computer cards between the laboratory jack and cell assembly.

The cell preparation involved a thorough cleaning of the copper electrodes and glass sidewalls. First the copper electrodes were sanded with sandpaper (fine grade) and then rinsed with distilled water. The copper electrodes were further cleaned with acetone and rinsed with distilled water once more. The glass sidewalls were cleaned with both distilled water and acetone and dried with paper towels. This cleaning procedure was generally done after every second or third run.

Once the cell was cleaned the spacers were put into place. From 1 ml to 400 ml (depending on layer height) of .13 molar copper-sulfate solution was put into the cell. Distilled water was added next until the desired layer height was obtained. At this point the horizontal level of the cell was checked once more using a liquid level.

After the horizontal level of the cell was judged satisfactory, measurements were made to determine the height of the scattering

volume from the bottom of the cell. This was accomplished by placing a metric ruler attached to a metal plate in the fluid layer. The laser was then turned on, and a reading was taken of the height of the scattering volume relative to the bottom of the cell. Another metric rule was positioned outside of the wooden box containing the convection cell where it was used to measure the distance from the top of the aluminum slab to the bottom of the wooden box. The cell was moved to several different heights, where readings were taken of both the height of the scattering volume from the bottom copper plate and the height of the wooden box relative to the top of the aluminum slab. In this way the scattering-volume location was calibrated with the movement of the convection cell.

Once the scattering-volume height calibration was complete the ruler in the fluid layer was removed, and the scattering particles were added. For this study the naturally-occurring particle concentration in the distilled water was too low; therefore artificial seeding was added in the form of .312 μm-diameter polystyrene spheres. These particles were manufactured by Dow Chemical Corporation and have a specific gravity of 1.05.

After the scattering particles had been added the top plate assembly was lowered into place. As it was being lowered it was tilted slightly to facilitate escape of air bubbles. A visual observation was made to check for the presence of air bubbles on the top plate. If there were air bubbles present, the top plate assembly was

moved slightly up and down to promote bubble escape. If there was not enough water present, more was added through the small opening between the glass sidewalls and the sides of the upper plate assembly.

Before turning on the power to the convection cell a check was made to be sure there was not a short in the upper plate assembly between the copper and aluminum plates. If the resistance measured between the copper electrode shown in Fig. 5 and the top aluminum plate was several megohms, the test proceeded.

Cooling-water flow was next started, followed by the application of power to the cell. Before applying power to the cell the Variac (see Sect. 2.1) was first adjusted to a minimum output so that the initial applied voltage (and thus power) was low. The voltage level was then increased slowly to the desired approximate power level. As this was being done, the current level was monitored with a Simpson Model 153 amp-clamp in order to detect excessive and unsafe current levels. The final power level was never the same as the initial power level since the ohmic heating within the fluid layer is a function of the electrical conductivity which in turn is a function of the temperature distribution in the water layer.

3.5 Velocity Measurements in the Convection Cell

After power was applied to the convection cell, a period of time was allowed to elapse for attainment of steady-state conditions before velocity measurements were made. Boon-Long (1978) calculated the time required to reach steady-state conditions based on the solution

of the one-dimensional transient conduction equation. His calculations for this time yielded 2.18 hours for a layer height of 5.08 cm, 8.96 hours for a layer height of 10.16 cm, and 36.9 hours for a layer height of 20.32 cm. Boon-Long also pointed out that these time estimates were conservative due to the fact that the additional convective motion accelerated the approach to steady-state conditions. Accordingly, these times were used only as rough estimates of the time needed to reach steady-state conditions. In fact, for most runs the actual time taken exceeded the times calculated by Boon-Long.

Three criteria were used in establishing the existence of steady-state conditions. First, the elapsed time between the start of the cell and the start of measurements was roughly equal to the time estimates calculated by Boon-Long. Second, the power level had to have been relatively constant (less than 3% fluctuation) for at least thirty minutes prior to velocity measurements. Third, no variations in the coolant temperature to the warmer of the two electrodes were allowed during the time taken to reach steady-state conditions. If a variation was recorded during this period, extra time (generally one hour for each variation) was allotted before velocity measurements were made.

After steady-state conditions were established in the cell, velocity measurements were made. Although there was no set start-location for the velocity measurements, generally the measurements were started in the middle of the layer, followed by successive measurements closer to the bottom of the cell. The scattering volume was

then returned to the middle of the fluid layer, and subsequent measurements were taken in the upper half of the fluid layer. When the scattering volume was moved, at least five minutes elapsed before any measurements were recorded in order to allow any transient phenomena created by the cell movement to decay away.

Similarly to the case of the rotating glass plate, counts were not taken for a set period of time, but rather a count total of at least 10,000 was obtained for each measurement location. As alluded to previously the count distribution or spectra in the MCA memory did not change appreciably after 10,000 counts. Nevertheless most count totals were between 20,000 and 40,000 counts. After each measurement was made the resultant spectra in the MCA memory was recorded on magnetic tape for computer analysis of the velocity information. The procedures employed in obtaining the experimental velocities is described in Sect. 3.6.1.

After the velocity measurements had been made (a procedure that generally took three to four hours) voltage readings of the thermocoupler were recorded in the upper and lower plate assemblies. A final power reading was also recorded at this point. These data were subsequently used in the calculations for the internal Rayleigh number (Ra_{KG}), the external Rayleigh number (Ra_E), and the fraction of downward heat transfer as predicted by the Baker, Faw, and Kulacki model (η_{BFK}) as described in Sect. 1.1

3.6 Velocity and Heat Transfer Calculations

3.6.1 Velocity Calculations

The signal analysis system described in Sect. 2.3 was designed to obtain signals proportional to the Doppler period. As shown in Appendix A.4.2, these signals were related to the instantaneous velocities of the scattering particles according to the following relationship:

$$V = \frac{\lambda f_D}{2\sin\theta} \quad . \tag{A.21}$$

Because a continual signal was used in this study to obtain the desired velocity information, the spectrum collected by the multichannel analyzer was not confined to a single channel location. Instead, the spectra obtained were broadened about some mean value due to the effects described in Appendix A.8.2. Specifically, for the case of the rotating glass plate, the source of broadening was due to transit time effects, while for the convection cell the broadening was due to both transit-time effects and velocity fluctuations about some mean value due to the presence of turbulence in the flow field.

Despite the presence of the broadened signal, the required mean-velocity information was still obtained easily from the spectra by evaluating the mean frequency according to the following equation:

$$\overline{f}_D = \frac{\sum_{i=1}^{N} \nu_i \, \psi(\nu_i)}{\sum_{i=1}^{N} \psi(\nu_i)} \quad . \tag{8}$$

For the case of laminar flow, the value obtained for $\overline{f}_D$ is the actual value of the velocity when used in Eq. (A.21).

For this study the frequency calibration of the mutlichannel analyzer was of the form (recall Eqs. (5) and (6))

$$\ln (\text{freq}) = A + B \ln (\text{Ch. no.}) \; . \tag{9}$$

Thus Eq. (8) was altered accordingly:

$$\ln \overline{f}_D = \frac{\sum_{i=1}^{N} \ln \nu_i \; \psi(\ln \nu_i)}{\sum_{i=1}^{N} \psi(\ln \nu_i)} \; . \tag{10}$$

Once a value for $\overline{f}_D$ was obtained, Eq. (A.21) was used to evaluate the desired value of the average velocity. A computer program was written to carry out both of these calculations and is described in Appendix C.

3.6.2 Heat-Transfer Calculations

The external and internal Rayleigh numbers and the fraction of energy generated and transferred downward were calculated. To evaluate the Rayleigh numbers, the first step was to convert the thermocouple readings obtained from the plate assemblies into temperature measurements. The conversion tables used to convert the thermocouple millivolt readings into temperature readings were obtained from a reference edited by Weast (1975). Average temperatures were than calculated for each plate from the thermocouple measurements.

The next step was to obtain the appropriate physical properties of water. These properties were obtained from pure-water tables supplied in a reference by Kreith (1973), and were evaluated at the average temperature of the upper and lower fluid boundaries.

Evaluation of the internal Rayleigh number required that the power be obtained from the dc-millivolt output from the watt transducer. The watt transducer was rated to yield a 55 millivolt output for a rated power level of 2000 watts. Lower output readings were scaled according to the rated values in the calculation of the steady-state power level in the cell.

After all of the necessary preliminary calculations had been completed, the values for external and internal Rayleigh number were evaluated using Eqs. (2) and (3). These two calculated Rayleigh numbers were then used in an evaluation of the following equation for the fraction of downward heat transfer as predicted by Baker, Faw, and Kulacki (1976):

$$\frac{(1 - \eta_{BFK})^{0.870}}{32\ \eta_{BFK}^{2} + Ra_E/Ra_{KG}} = 0.0138\ Ra_{KG}^{0.226} \qquad (11)$$

In Boon-Long's study (1978) a procedure was developed whereby he was able to calculate experimental values for the fraction of downward heat transfer and the heat balance. For this study it was not possible to obtain these two measurements as both of these values depended on accurate values for the thermal conductivity for the region between the two sets of thermocouples in each plate assembly. Experi-

mental runs were performed to determine these two thermal conductivities, but no satisfactory values were obtained as variations as high as 100% were measured. In lieu of dismantling and rebuilding the apparatus, an ice-water bath was placed in the cell to check the functional thermocouples in the copper plates. The thermocouples in the copper plates indicated the correct readings; thus it was decided that satisfactory measurements could be made of the water properties of the fluid layer and of the external Rayleigh number (which is directly proportional to the temperature difference between the upper and lower copper plates). Therefore a decision was made in the interest of time to forego any attempt to rebuild the cell and to continue with the study.

4.0 EXPERIMENTAL RESULTS AND DISCUSSION

In this chapter experimental results are presented for velocity measurements made of a rotating glass plate and in the convection cell. The velocity results from the rotating glass-plate demonstrate the limitations and abilities of the LDA system developed for this study, and these abilities and limitations will be examined closely to see how they affect the velocity measurements made in the convection cell.

4.1 Rotating Glass-Plate Results

Tangential velocities at fourteen different radial positions on the rotating glass plate assembly described in Sect. 3.3 were measured with the LDA system. The resultant tangential velocities roughly covered the range of velocities expected in the convection cell. At each radial position two velocity measurements were made with the LDA system; one with the 0.01 -sec TAC conversion range and the other with the 0.03 -sec TAC conversion range. The results of these measurements are presented in Table 1 and in Fig. 14. A conservative error of $\pm$ 2 mm was assumed for each radial-position measurement, while no error was assumed to be associated with the angular speed of the motor used to rotate the glass plate. The latter conclusion is buttressed by the fact that several different measurements yielded no observable differences in the rated speed. Thus the error bars associated with the true tangential velocities depicted as a straight line in Fig. 14 were calculated using Eq. (7) and the $\pm$ 2 mm error associated with the measurement of r.

Table 1. Rotating Glass-Plate Data

r(mm)	V_T(mm/sec)	V_r^a(exp)	% error[a]	V_T^b(exp)	% error[b]
29.5	1.24	1.35	8.9	1.31	5.7
34.5	1.45	1.60	10.3	1.54	6.2
37.5	1.57	1.69	7.6	1.62	3.2
42.0	1.76	1.86	5.7	1.76	0
43.5	1.82	1.93	6.0	1.82	0
47.5	1.99	2.06	3.5	1.88	-5.5
51.5	2.16	2.27	5.1	2.17	0.5
55.5	2.32	2.33	0.4	2.15	-7.3
59.0	2.47	2.53	2.4	2.38	-3.6
61.0	2.56	2.62	2.3	2.47	-3.5
64.0	2.68	2.78	3.7	2.60	-3.0
67.0	2.81	2.85	1.4	2.69	-4.3
70.0	2.93	2.99	2.1	2.71	-7.5
74.0	3.10	3.13	1.0	2.90	-6.4

[a]TAC range = .01 sec.
[b]TAC range = .03 sec.

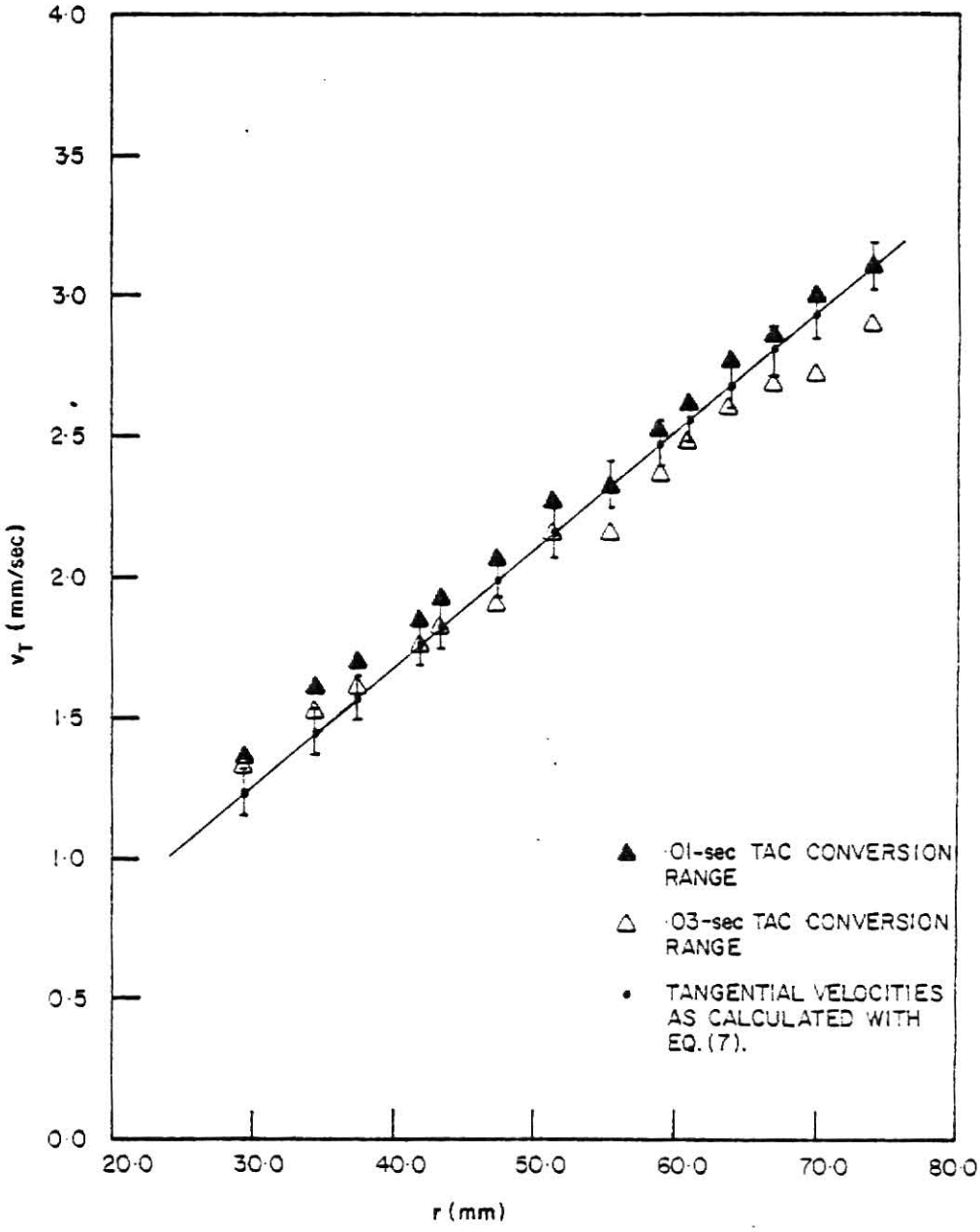

Fig. 14. Experimental Test Results of LDA System-Rotating Glass Plate.

The effect of the non-linear conversion capability of the TAC (refer to discussion on this effect in Sect. 3.1) is readily illustrated with the aid of Fig. 14. As an example, consider the velocity results generated with the .03 -sec TAC conversion range. Note that in this range the measured velocity is more and more underestimated with increasing velocity. This effect can be explained with the help of Fig. 15, which is the multi-channel analyzer spectrum for the 3.10 mm/sec measurement made with the .03 -sec TAC conversion range. Note in this figure the location of channels 44 and 95. Using Eq. (5) a calculation can be performed to determine the change in the frequency sensitivity in the peak region shown in Fig. 15. For channels 44 and 45 the frequency equivalents are 406 hz and 397 hz respectively, while for channels 94 and 95 the frequency equivalents are much closer, 187 hz and 185 hz, respectively. Thus frequencies higher than 397 hz, but less than 406 hz, increment only channel 45, thus illustrating the loss in frequency sensitivity with decreasing channel number. This effect, as shown in Fig. 15, tends to skew the resultant spectra towards the lower-frequency region, and results in a calculated average-velocity that is less than the true velocity.

The effect is different for the .01 -sec TAC conversion range as the frequencies (and hence velocities) decrease. As shown in Fig. 14 this range tends to overestimate the velocity as the magnitude of the velocity decreases. This effect can be explained with the help of Fig. 16, which is the multichannel-analyzer spectrum for the 1.24

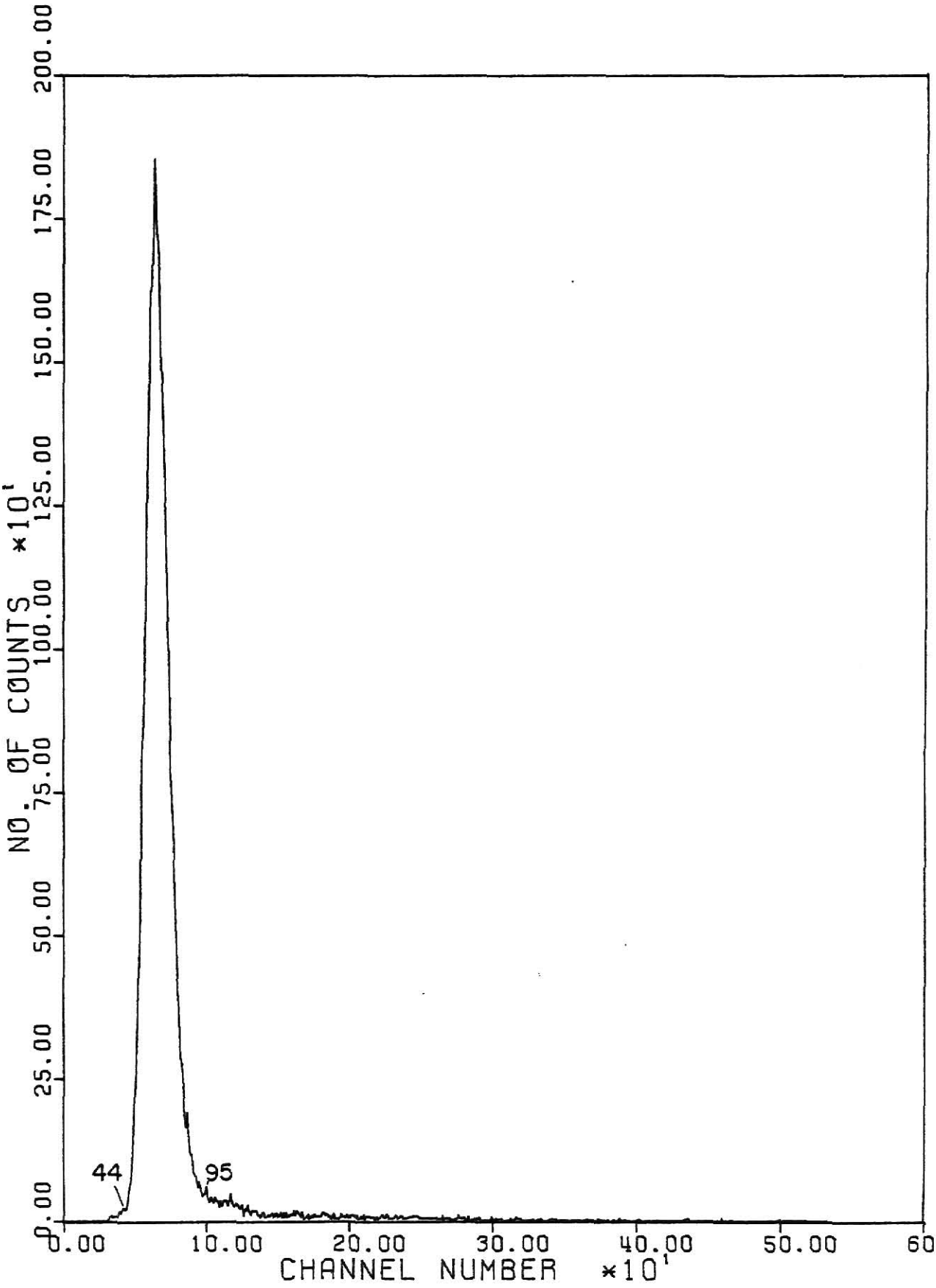

Fig. 15. MCA Spectrum for Tangential Glass-Plate Velocity = 3.10 mm/sec, as Measured with the 0.03-sec TAC Conversion Range.

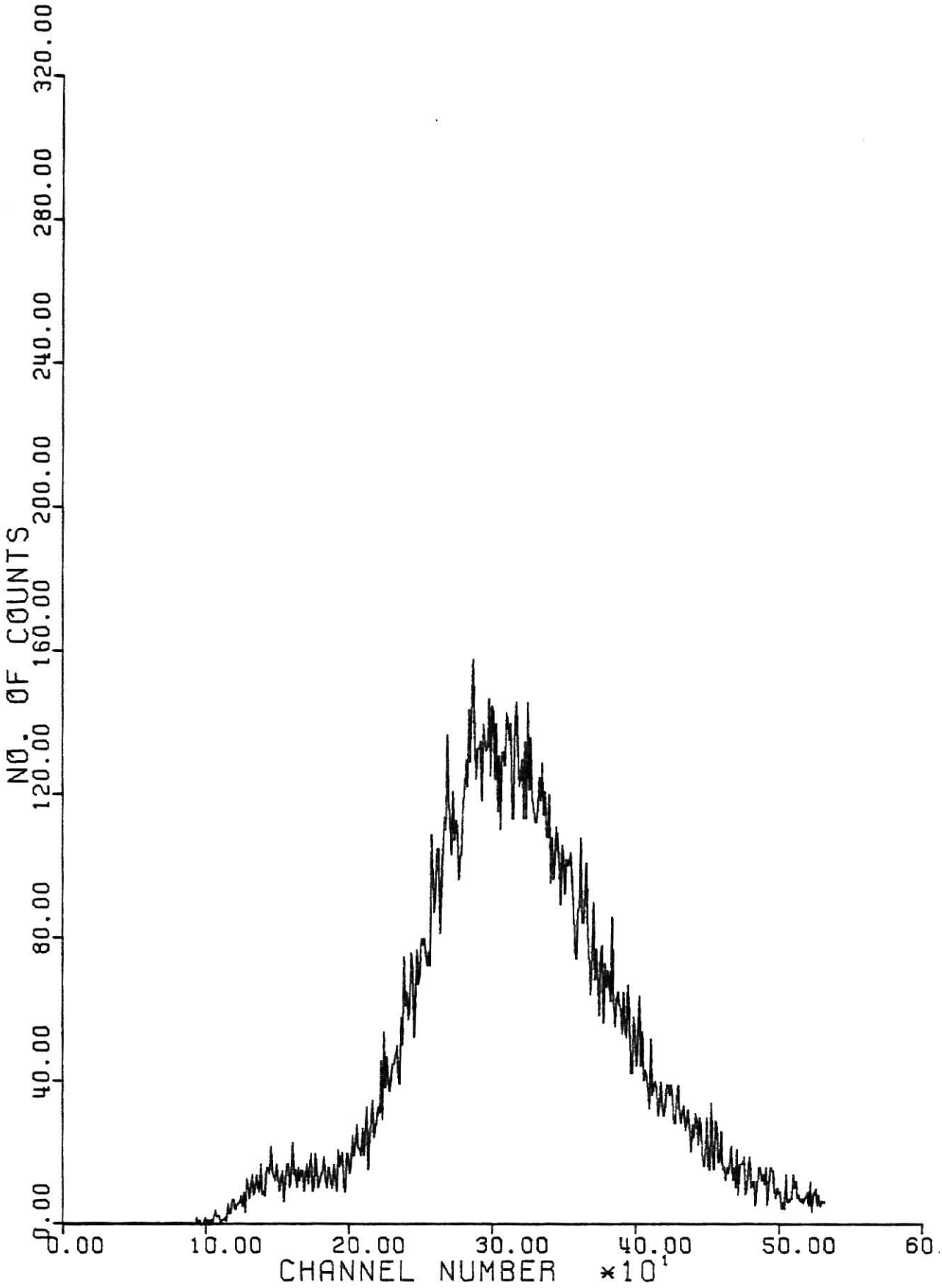

Fig. 16. MCA Spectrum for Tangential Glass-Plate Velocity = 1.24 mm/sec, as Measured with the 0.01-sec TAC Conversion Range.

mm/sec measurement made with the .01-sec TAC conversion range. As shown in this figure there is a significant loss of low-frequency signals because the period of these signals is greater than the TAC conversion range. Thus the calculated average velocity is higher than the true tangential velocity.

Generally speaking, the non-linear capabilities of the TAC is an undesirable feature for an LDA signal-analysis system. This non-linear characteristic skews and broadens the resultant multichannel-analyzer spectrum (as shown in Figs. 15 and 16), and affects the results of the calculation for the average frequency. Still, the calculated velocities agree to within 10% with the true tangential velocities. Thus if the LDA signal-analysis system is used with care (e.g., do not use the .01-sec TAC conversion range for low-frequency signals) a reasonable estimate can be made of the average velocity.

The TAC non-linearity does preclude other measurements of interest such as the measurement of a velocity gradient across the scattering volume (see Fig. 17). A velocity gradient across the scattering volume would broaden and skew the multichannel-analyzer spectrum relative to that for a point measurement (Durst, Melling, and Whitelaw, 1976). Although models have been developed to account for a velocity gradient (e.g., Edwards, et al., 1971), they could not be applied to the LDA system developed for this study because no method exists for taking into account the spectrum broadening and skewness due to the non-linear TAC conversion.

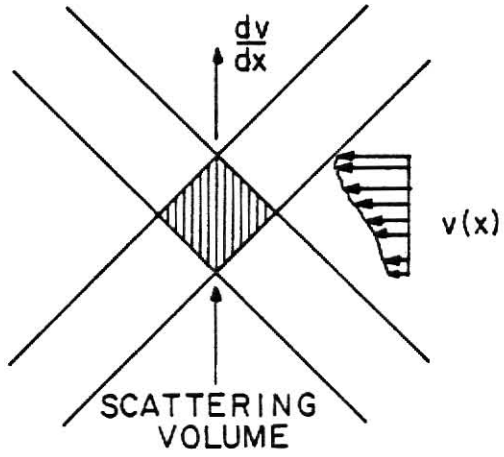

Fig. 17. Pictorial Representation of Velocity Gradient Existing Across LDA Scattering Volume.

If the fluid flow is turbulent (as it is in the convection cell) no parameters of interest other than the mean velocity can be determined due to the non-linear TAC conversion. For example, consider turbulence intensity, which is defined as (Eckert and Drake, 1972)

$$J = \frac{\sqrt{\frac{1}{3}\left(\overline{u'^2} + \overline{v'^2} + \overline{w'^2}\right)}}{\overline{u}}, \qquad (11)$$

where it is assumed that the mean velocity is in the x-direction. If no velocity gradient existed across the scattering volume, turbulence intensity would manifest itself as a symmetrical broadening of the multichannel-analyzer spectrum over and beyond that due to transit-time effects (for discussion of transit-time effects, see Appendix A.8.2). Thus with careful measurement of transit-time effects, a determination of the turbulence intensity could have been made with a better signal-analysis system.

Before a discussion of the results obtained with the convection cell is presented, it should be noted that velocity measurements made with a rotating glass-plate are not as straightforward as it might appear. Placement of the glass plate relative to the scattering volume is very important. Figure 18.a depicts proper placement of the glass plate relative to the scattering volume, while Figs. 18.b and 18.c depict two examples of improper placement. In Fig. 18.b, placement of the scattering volume on the second glass-air interface results in a decreased angle of separation between the two beams forming the scattering volume. According to Eq. (A.21), this lowers the frequency of the

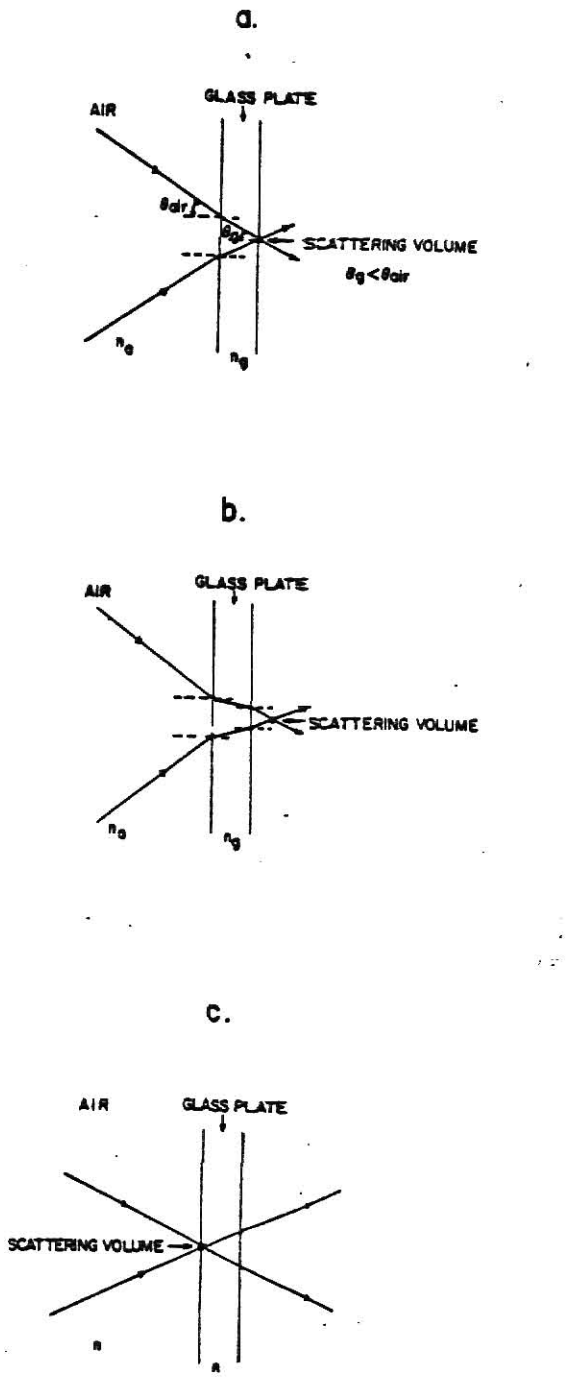

Fig. 18. Proper and Improper Placement of LDA Scattering Volume with Respect to a Rotating Glass Plate.

Doppler signal. This can be taken into account if an accurate value of θ_g, is substituted into Eq. (A.21). If θ_{air} is used in Eq. (A.21) with the lower frequency signals, the result is low average-velocity value. The correct value for the velocity can be obtained if θ_g is used in Eq. (A.21). However, this quantity is generally not known as well as θ_{air}, so it is better to position the scattering volume at the first glass-air interface.

In Fig. 18.c the scattering volume is not focused at either of the two glass-air interfaces. However, an apparent Doppler signal can be detected with this configuration. As explained in a paper by Durst (1973), the apparent Doppler-signals are obtained when separate beams illuminate separate particles (all of which have approximately the same velocity). For this example Durst derived that the resulting signal frequency is

$$f_D = \frac{2\ U\ \sin\theta}{\lambda} \qquad (12)$$

where U is the component of the particle velocity perpendicular to the beams. Since only a component of the tangential velocity is being measured, the Doppler-signal frequency is less, and a subsequent velocity analysis indicates a lower velocity than the true velocity. Improper scattering volume placement is believed to be the reason for the relatively inconsistent data points for V_T = 1.99 and 2.32 mm/sec shown in Fig. 14.

The next section will present the results obtained from velocity measurements made in the convection cell apparatus described in Sect.

2.1. Many of the LDA-system limitations discussed in this section will be further illustrated in this next section.

4.2 Convection Cell Results

Velocity profile measurements were obtained in the convection cell for ten different sets of internal and external Rayleigh numbers in accordance with the procedure outlined in Sect. 3.5. The range of experimental data is $6.28 \times 10^6 \leq Ra_{KG} \leq 1.07 \times 10^{10}$ and $2.24 \times 10^7 \leq |Ra_E| \leq 2.36 \times 10^9$, and is depicted in Fig. 19. As shown in Fig. 19 two of the ten measurements were made with positive external-Rayleigh numbers while the other eight measurements were made with negative external-Rayleigh numbers. Because the lower fluid boundary is cooler than the upper fluid boundary, which enhances the possible existence of the conduction sublayer predicted by the Baker, Faw, and Kulacki model described in Sect. 1.1, more measurements were made with negative external-Rayleigh number values. The two lines displayed in Fig. 19 are the limits for convective heat transfer in an internally-heated fluid layer. The lower limit corresponds to the line of critical Rayleigh numbers as calculated by Ning (1977). Below this line no convection occurs; only conduction heat transfer is occurring. The upper limit corresponds to the line of zero downward heat flux, and was determined by Boon-Long (1978) from the experimental data collected by Kulacki and Emara (1975). Below this line the fluid is heated with internal heat sources only, but above the line the fluid layer is heated both internally and from below.

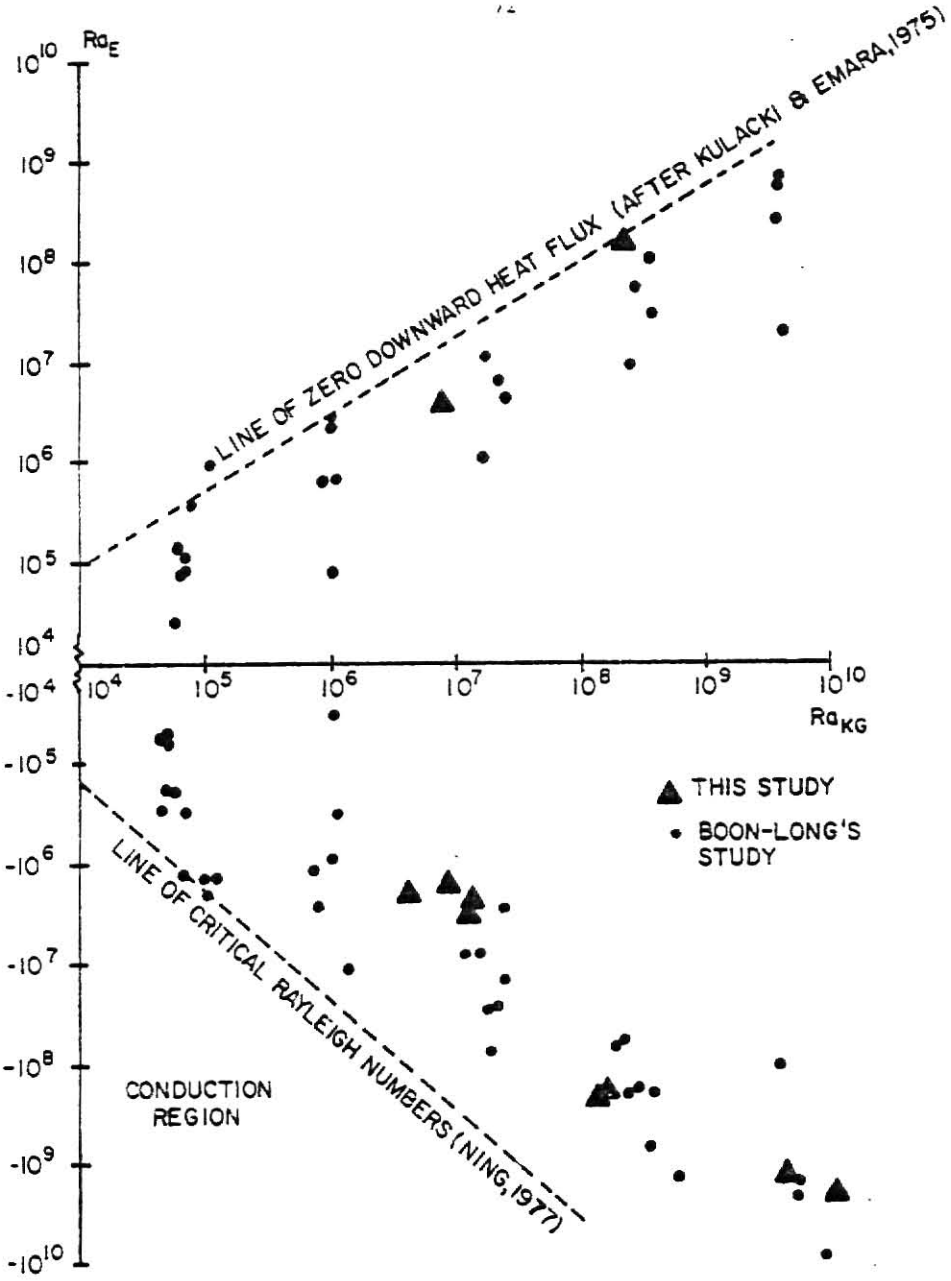

Fig. 19. Range of Experimental Data (after Boon-Long, 1978).

The ten experimental measurements were obtained using three different fluid-layer depths; 5.08 cm, 10.16 cm, and 20.32 cm. For the 5.08-cm layer depth it was possible to obtain measurements throughout the fluid layer. However, measurements very close to the bottom were limited by both the sealant applied between the glass sidewalls and the bottom plate assembly and by the amount of separation between the two focused beams used to form the scattering volume in the convection cell. Measurements close to the upper plate assembly were also limited by the beam spacing. For the 10.16 and 20.32-cm layer heights it was not possible to obtain vertical-velocity measurements over the entire fluid-layer depth due to the limited vertical travel of the laboratory jack used to vertically manuever the convection cell. Every attempt was made to measure as much as the fluid layer as possible for the two larger fluid-layer depths.

Diagrams of the velocity profiles obtained for the results reported in this study are presented in Figs. 20-25, while the numerical results are presented in Table 2. Before a discussion of these results is presented, a discussion is presented in the next section on the performance of the LDA system in the convection cell.

4.2.1 Convection-Cell LDA Measurements

Many of the LDA-system limitations discussed in Sect. 4.1 were graphically illustrated with the application of the LDA system to the convection cell. The measurement problems were primarily a result of the low velocities being measured and the turbulence associated with

Table 2. Convection Cell Vertical Velocity Results.

Run	L(cm)	Ra_{KG}	Ra_E	Z/L	$\overline{V}$ (mm/sec)
13	5.08	6.28×10^6	-3.11×10^7	.20	.82
				.30	.95
				.39	1.15
				.49	1.36
				.59	1.46
				.69	1.50
				.79	1.60
				.89	1.52
				.95	1.21
14	5.08	1.19×10^7	-4.49×10^7	.16	.82
				.20	.83
				.30	.88
				.39	1.10
				.49	1.46
				.59	1.73
				.69	1.77
				.79	1.76
				.89	1.62
				.94	1.21
16	5.08	9.62×10^6	-2.24×10^7	.20	.96
				.30	1.09
				.39	1.17
				.49	1.36
				.59	1.32
				.69	1.33
				.79	1.30
				.89	1.23
				.94	1.11
17	5.08	1.28×10^7	-3.37×10^7	.20	.62
				.30	1.04
				.39	1.07
				.49	1.22
				.59	1.28
				.69	1.31
				.79	1.33
				.89	1.29
				.94	1.20

Table 2 continued

Run	L(cm)	Ra_{KG}	Ra_E	Z/L	$\bar{V}$ (mm/sec)
18	5.08	8.69×10^6	5.99×10^6	.12	1.07
				.20	1.25
				.30	1.43
				.39	1.53
				.49	1.63
				.69	1.63
				.79	1.74
				.89	1.58
				.94	1.33
23	10.16	2.69×10^8	-1.92×10^8	.20	.88
				.25	1.49
				.30	1.77
				.39	1.85
				.49	2.11
				.59	2.08
				.69	2.18
				.74	2.17
25	10.16	2.79×10^8	1.76×10^8	.05	2.15
				.10	2.03
				.15	1.83
				.20	1.89
				.30	1.97
				.39	2.03
				.49	2.05
				.59	2.08
				.69	2.07
				.74	2.10
29	10.16	2.44×10^8	-2.23×10^8	.20	1.51
				.30	1.79
				.39	2.04
				.49	2.20
				.59	2.29
				.69	2.37
31	20.32	7.86×10^9	-1.86×10^9	.12	.89
				.17	1.66
				.20	1.72
				.22	1.75
				.25	1.98
				.27	2.12
				.30	2.15
				.32	2.27
				.34	2.45

Table 2 continued

Run	L(cm)	Ra_{KG}	Ra_E	Z/L	$\bar{V}$ (mm/sec)
32	20.32	1.07×10^{10}	-2.36×10^{9}	.12	1.03
				.15	1.04
				.17	1.42
				.20	1.76
				.22	1.85
				.25	1.90
				.30	2.11

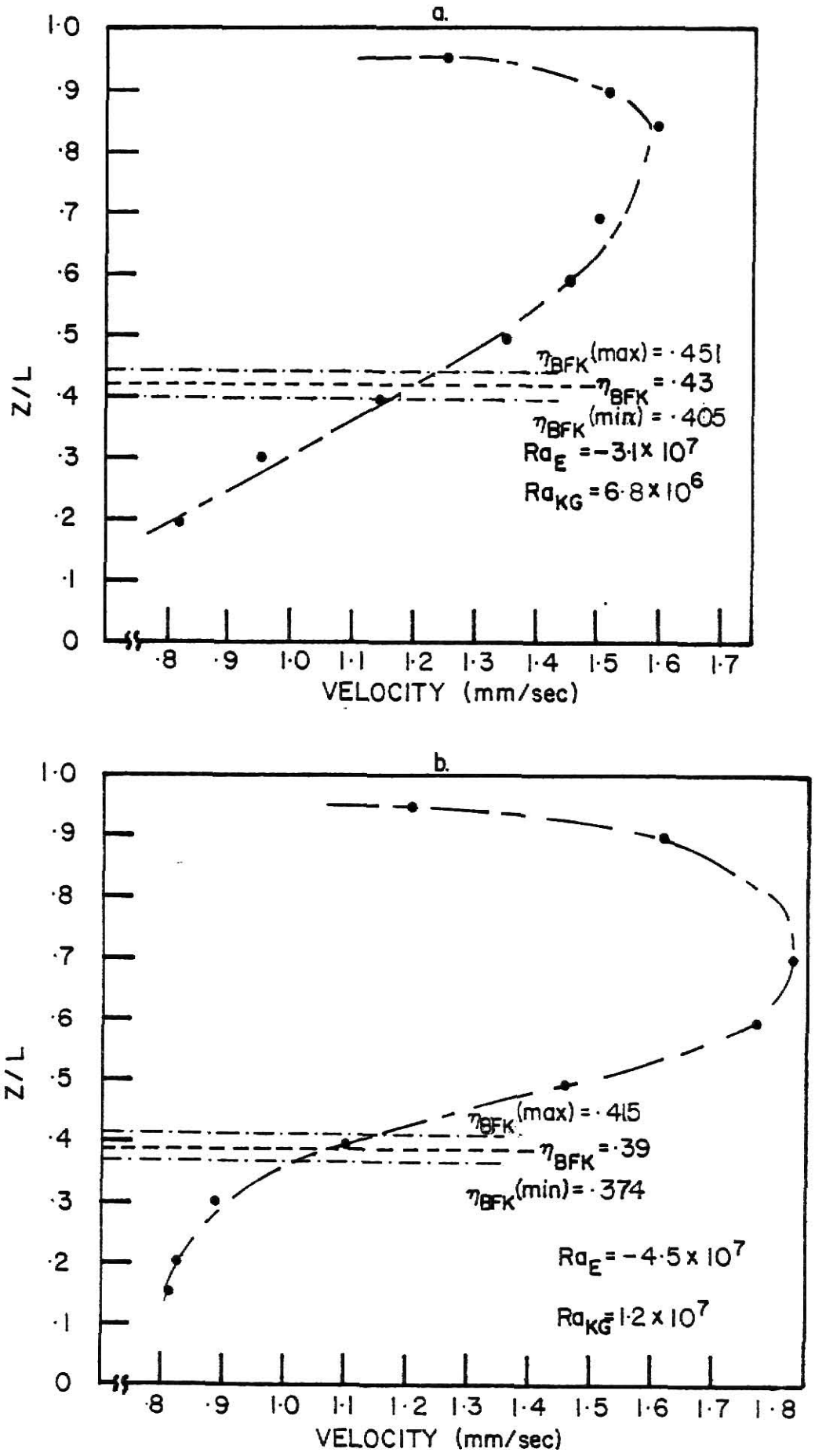

Fig. 20. Convection Cell Velocity Profiles (Z = 5.08 cm).
a. Experimental Run No. 13.
b. Experimental Run No. 14.

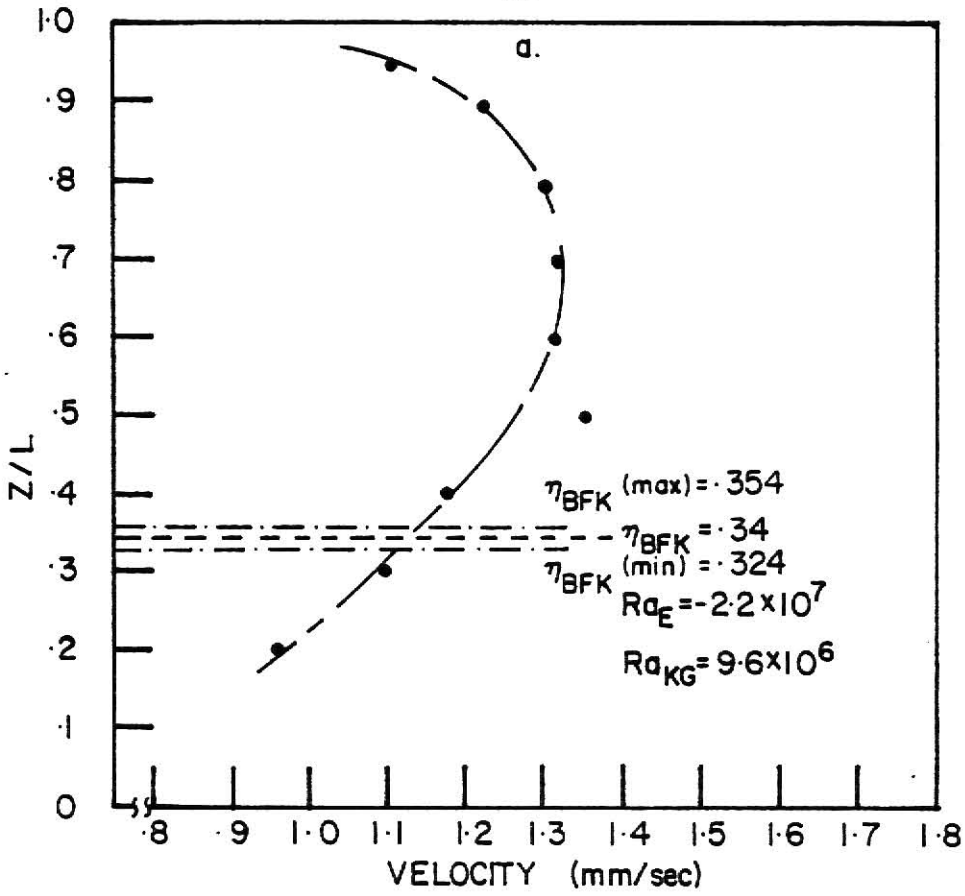

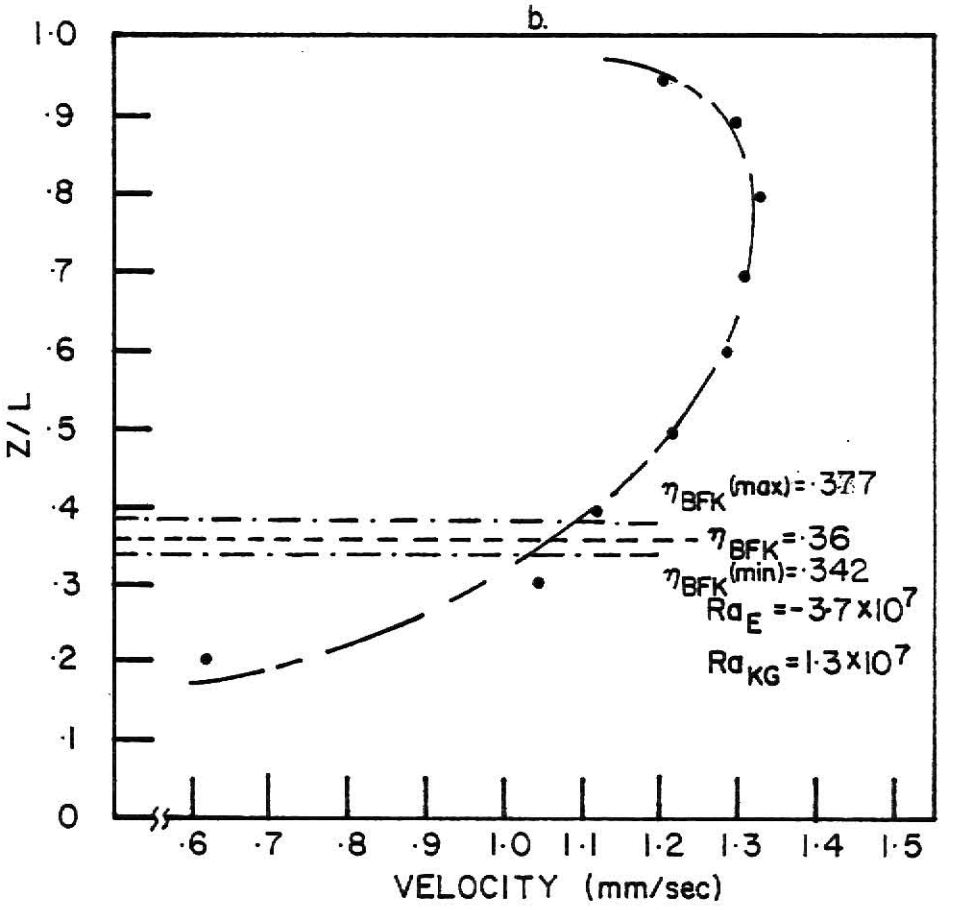

Fig. 21. Convection Cell Velocity Profiles (Z = 5.08 cm).
a. Experimental Run No. 16.
b. Experimental Run No. 17.

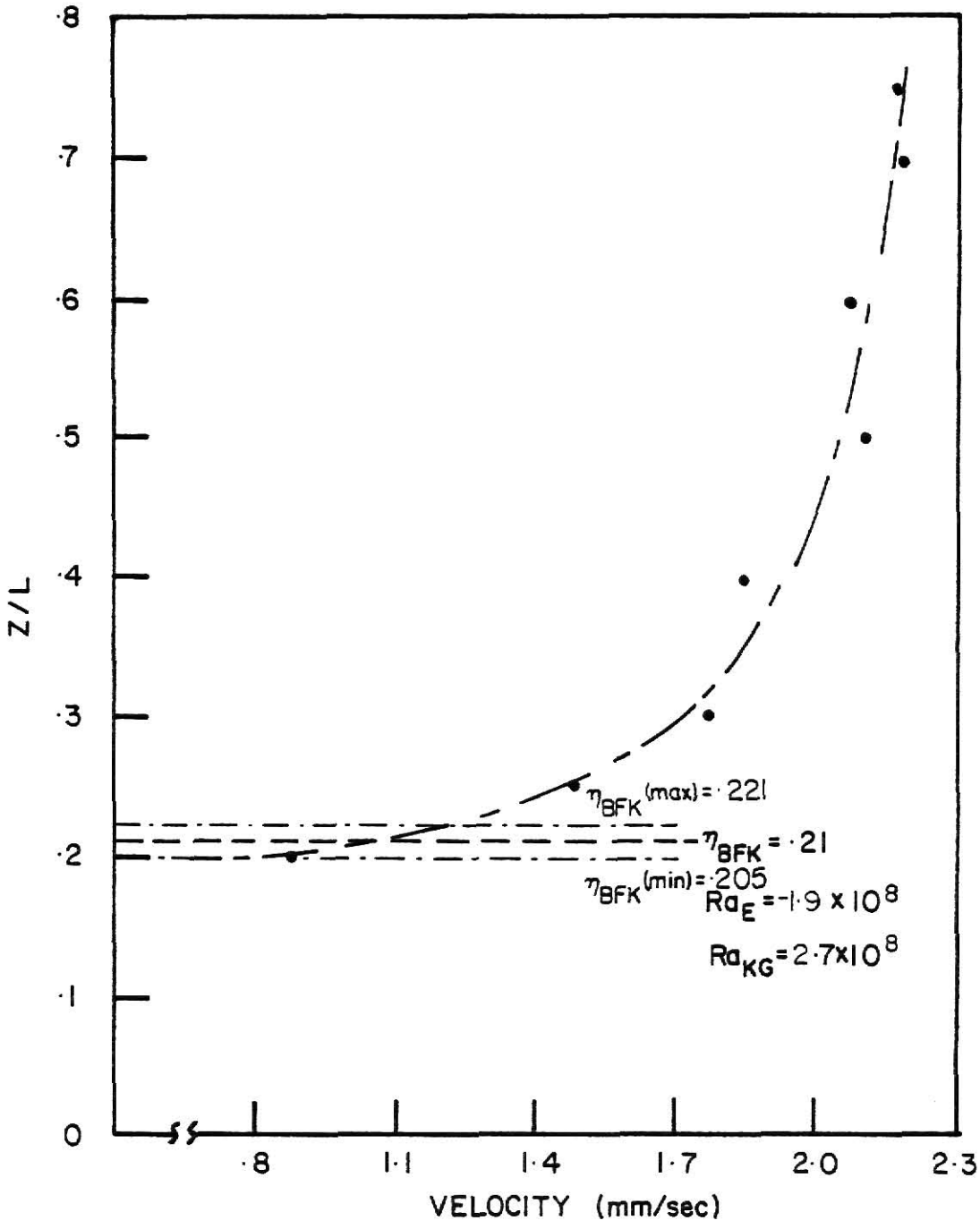

Fig. 22. Convection Cell Velocity Profiles (Z = 10.16 cm) - Experimental Run No. 23.

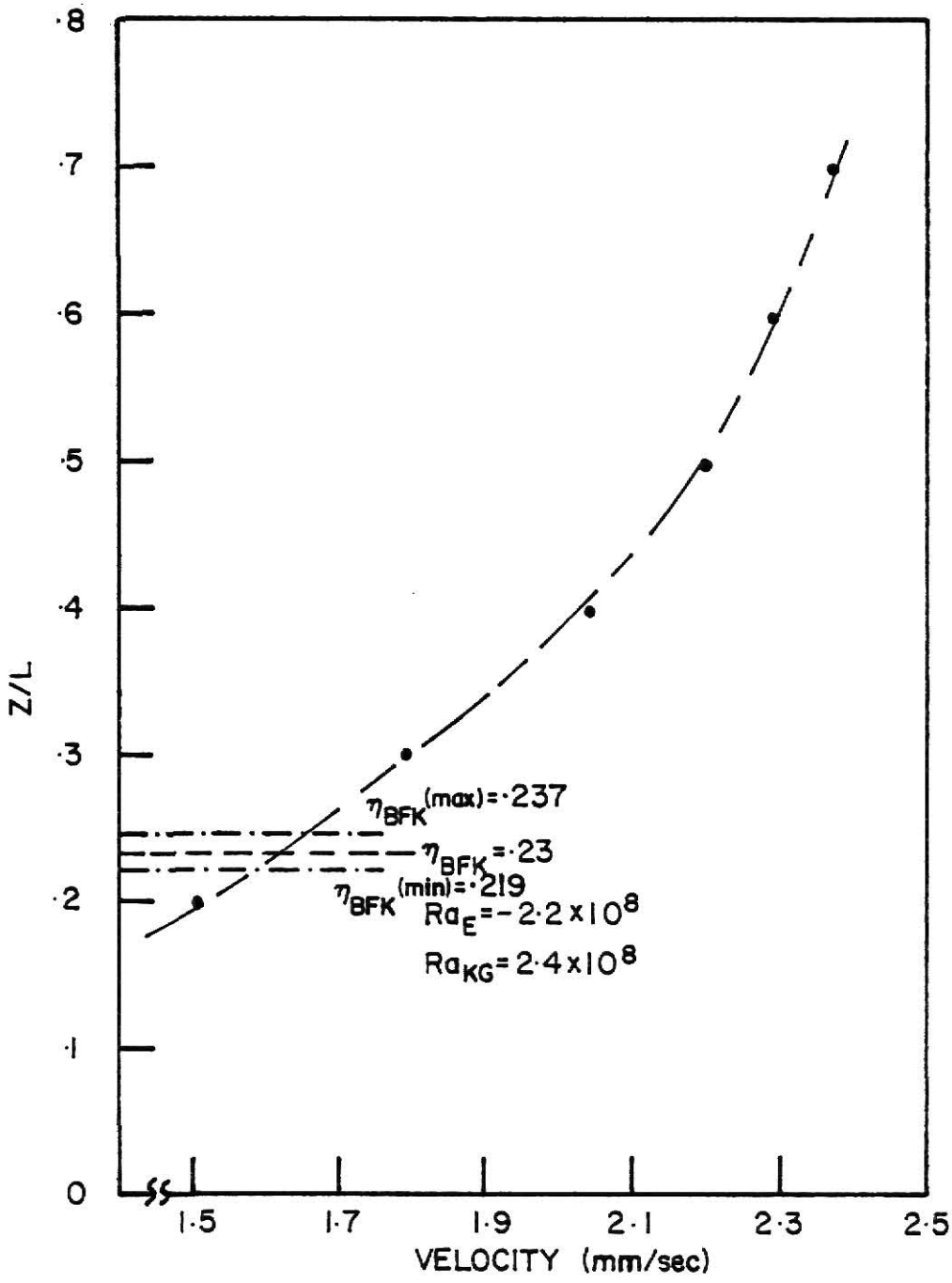

Fig. 23. Convection Cell Velocity Profile (Z = 10.16 cm), Experimental Run No. 29.

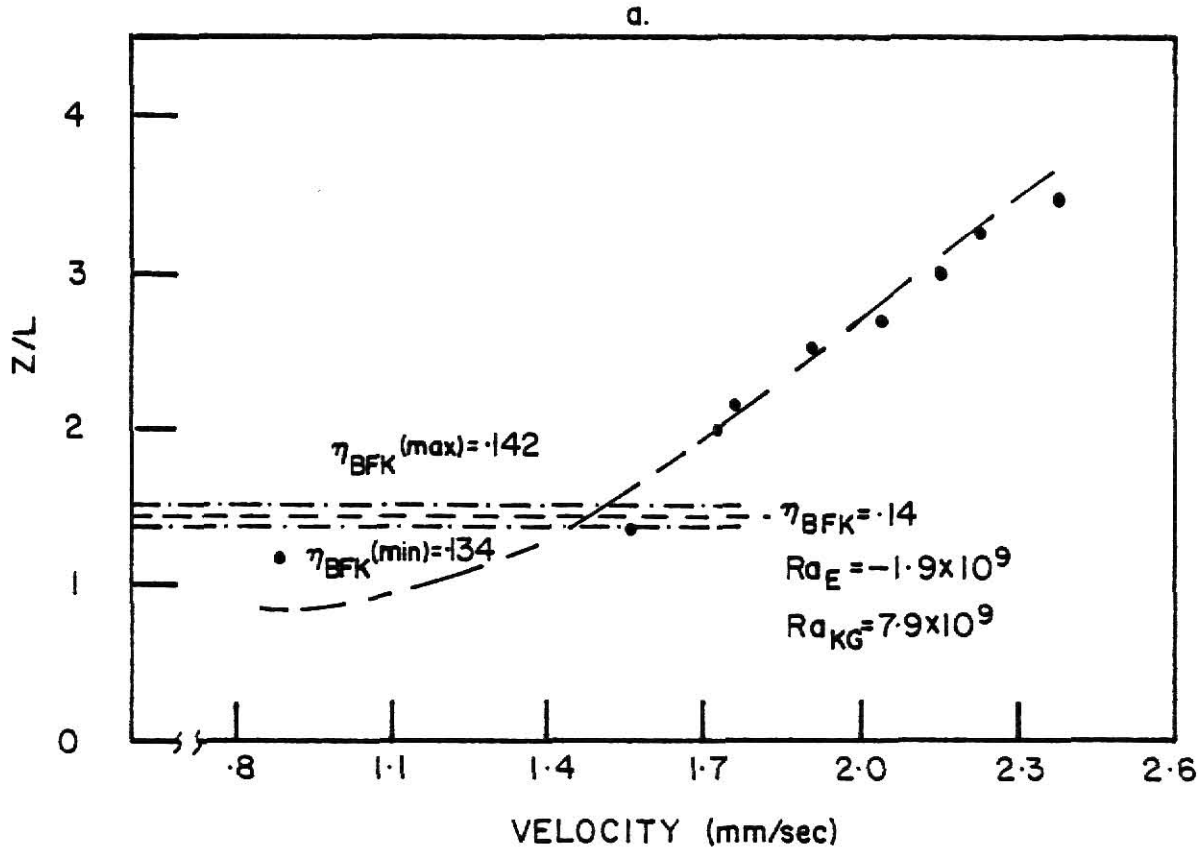

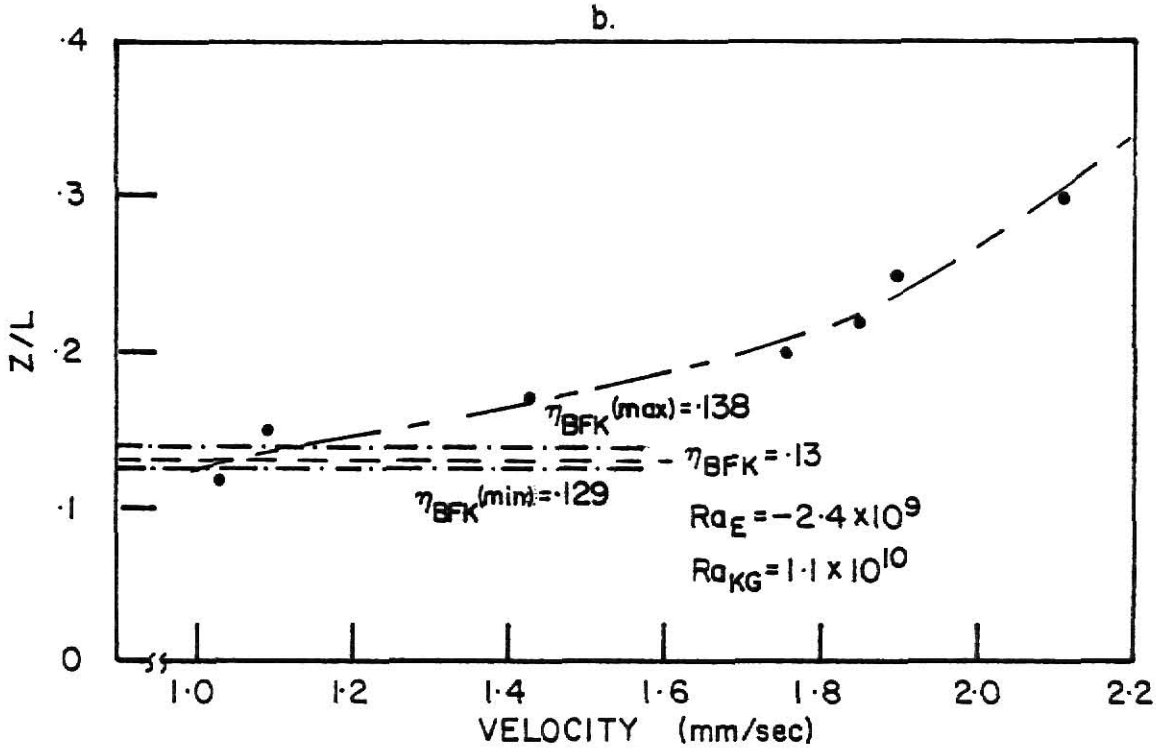

Fig. 24. Convection Cell Velocity Profiles (Z = 20.32 cm).
a. Experimental Run No. 31.
b. Experimental Run No. 32.

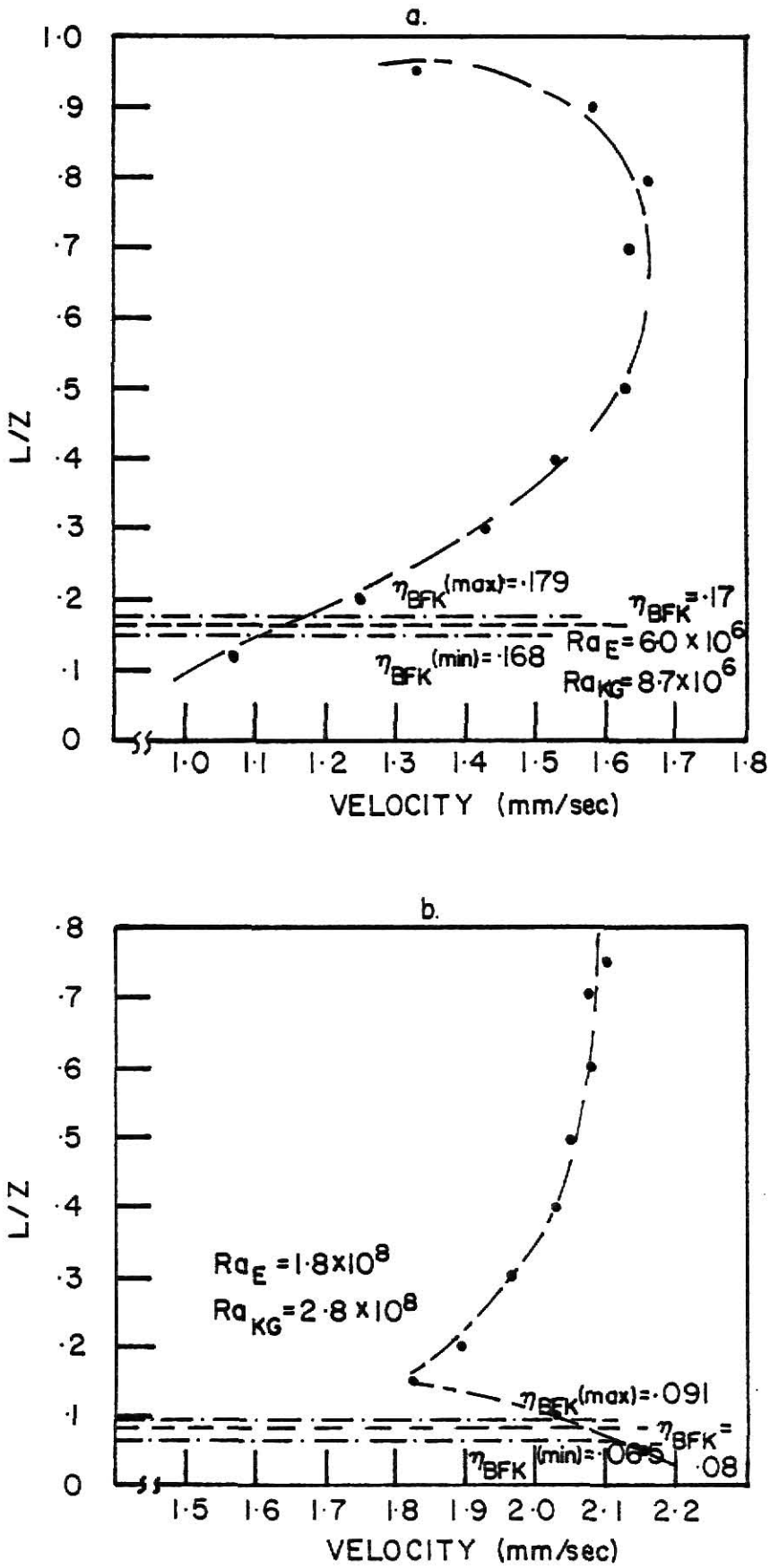

Fig. 25. Convection Cell Velocity Profiles, $|Ra_E|$.
a. Experimental Run No. 18, Z = 5.08 cm.
b. Experimental Run No. 25, Z = 10.16 cm.

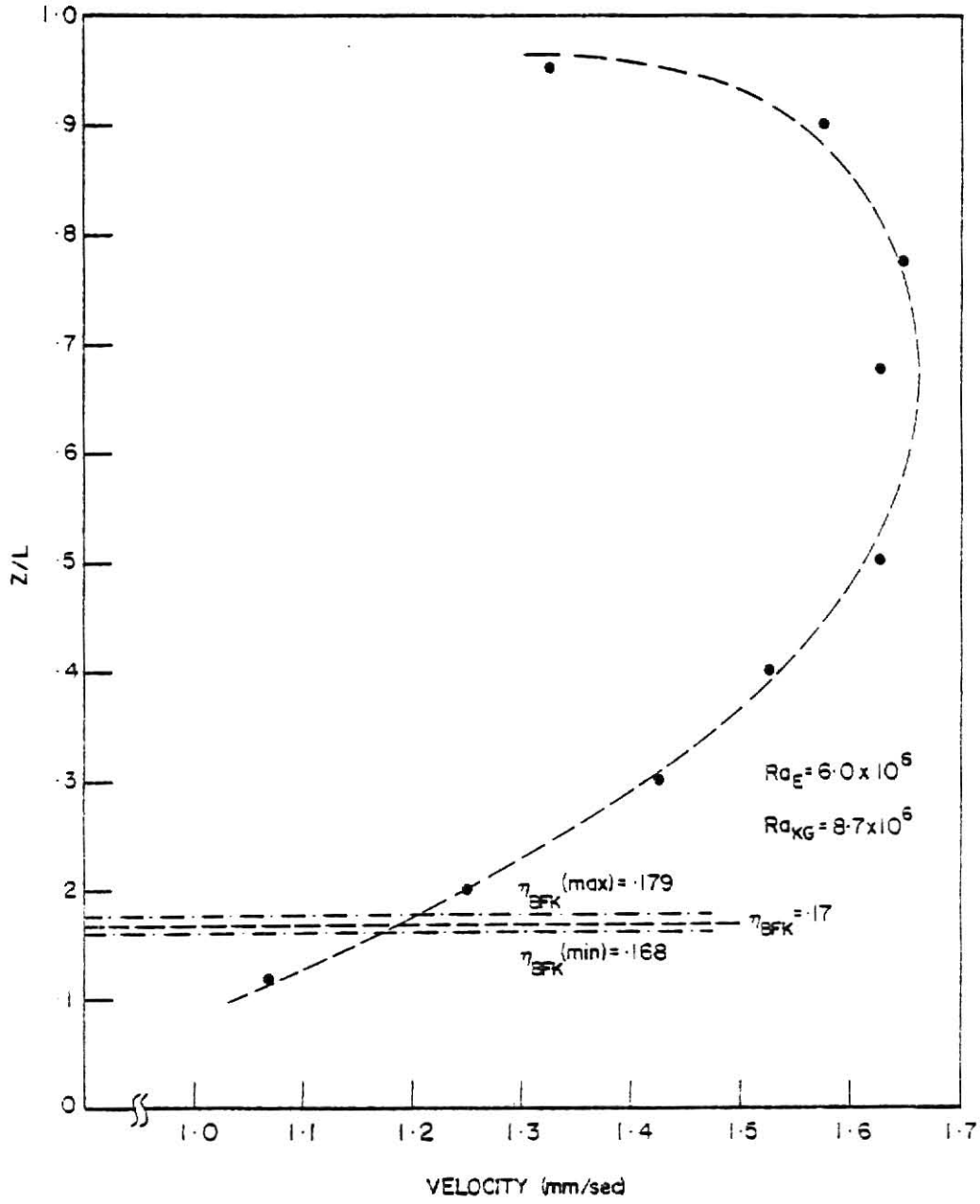

Fig. 25. Convection Cell Velocity Profile $|Ra_E|$. Experimental Run No. 18, Z = 5.08 cm.

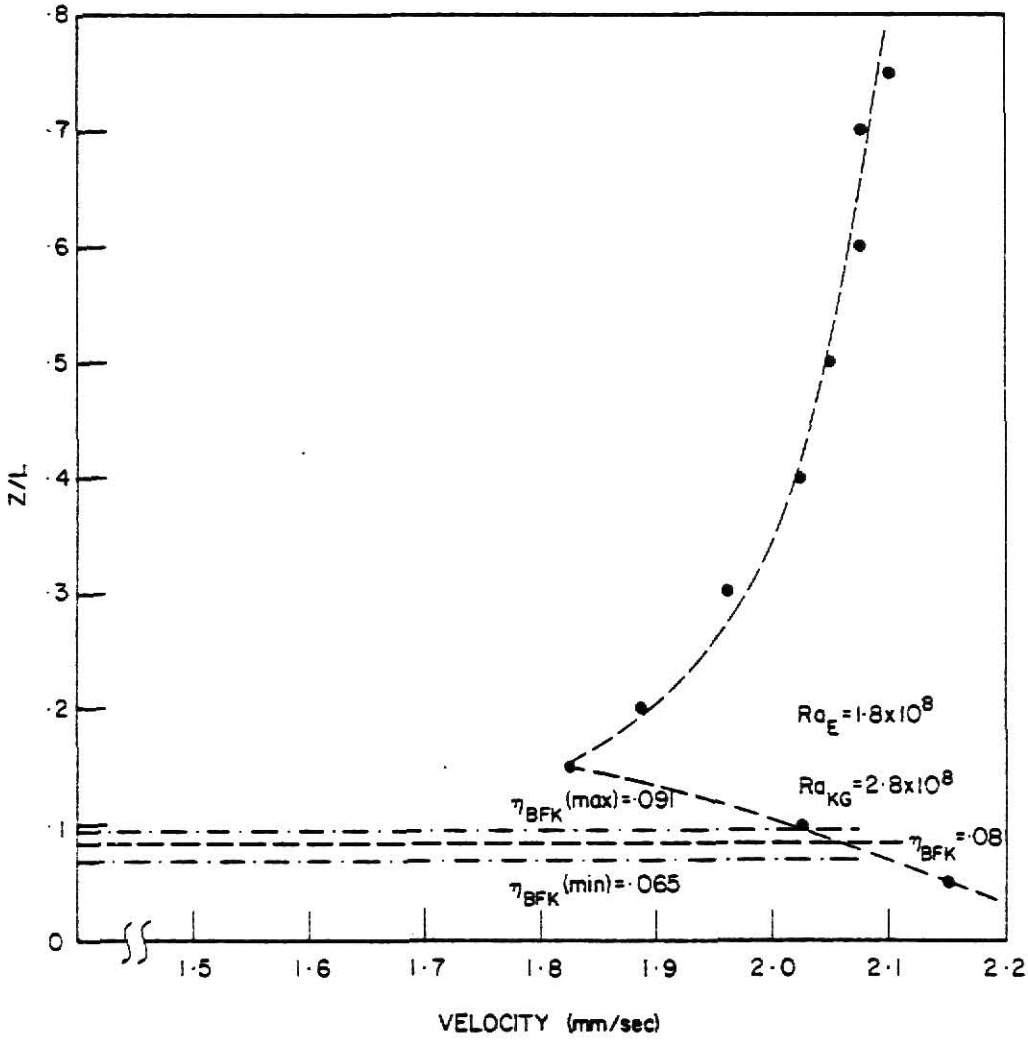

Fig. 26. Convection Cell Velocity Profile $|Ra_{\bar{F}}|$. Experimental Run No. 25, Z = 10.16 cm.

these low velocities. Consider, for example, experimental run no. 16 (see Fig. 21.a) Figures 27 and 28 depict representative multichannel-analyzer spectra obtained in experimental run no. 16. Upon comparison with Figs. 15 and 16 it is obvious that the spectra obtained from the convection cell have been considerably broadened due to turbulence effects. As a result of this broadening the non-linear TAC conversion process has a more pronounced effect on the resultant spectra than was evident with the spectra obtained from the rotating glass plate.

Another effect due to turbulence that presented problems in the experiment was that due to the randomly changing values of the instantaneous velocity - it became difficult to separate the Doppler portion of the total PM-tube signal from the pedestal component (see Appendix A.7 for description of the PM-tube output signal) as the average velocity in the convection cell decreased. Stating the problem in another way, because of turbulence-induced fluctuations in the instantaneous velocity it was difficult to adjust the band-pass filter so as not to lose any low-frequency Doppler signals but at the same time not let any higher-frequency pedestal signals pass through the filter to the signal analysis system. This was not a problem with the rotating glass-plate experiment because the glass plate rotated with a constant angular velocity and generated relatively constant signal frequencies. Thus the bandpass filter was more readily adjusted to remove the unwanted low-frequency component of the PM-tube output signal for signals generated by the rotating glass plate.

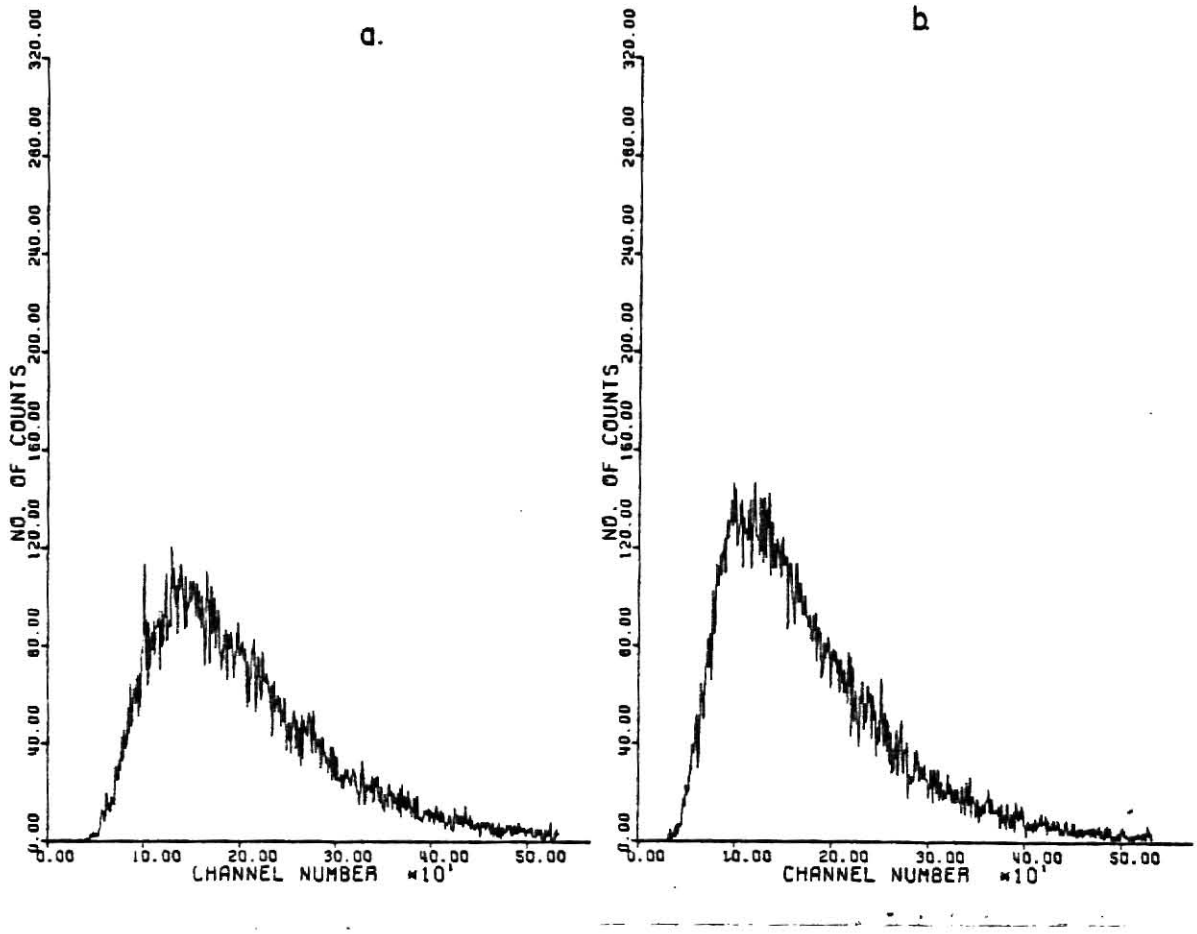

Fig. 27. Multichannel-Analyzer Spectra, Experimental Run No. 16. (Z = 5.08 cm)
a. Z/L = .94
b. Z/L = .79

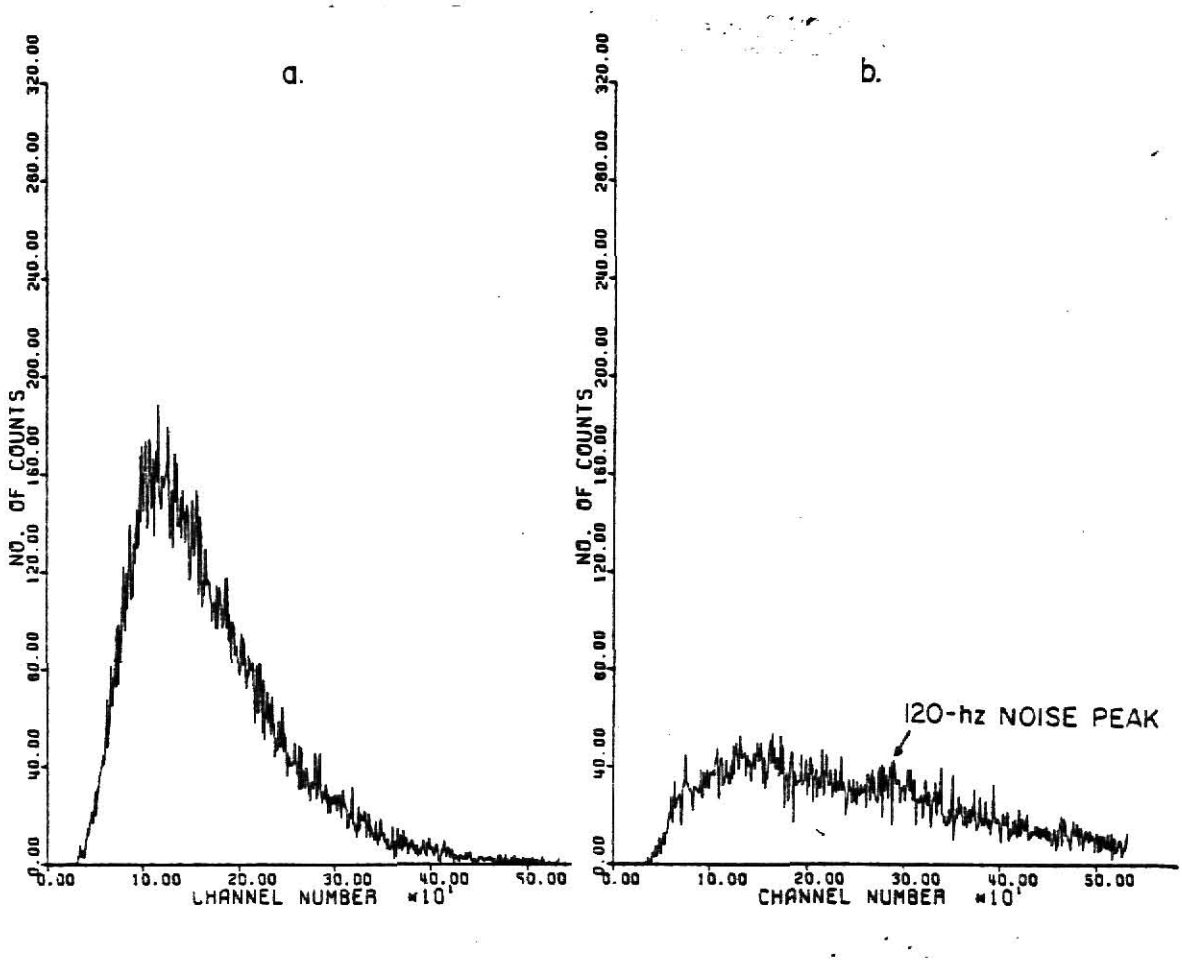

Fig. 28. Multichannel-Analyzer Spectra, Experimental Run No. 16 (Z = 5.08 cm)
a. Z/L = .49
b. Z/L = .20

It should be noted at this point that frequency-shifting (as described in Sect. 2.2) with the same optical configuration employed in this study would have eliminated any separation problems between the Doppler signal and the pedestal signal because the pedestal-signal frequency would have been unchanged while the Doppler-signal frequency would have been increased by an amount equal to the shift frequency.

Because the velocities measured in the convection cell were low, the corresponding Doppler-signal frequencies were also low. For this study the Doppler-signal frequencies ranged from the tens of hertz to the hundreds of hertz. Measurement of these relatively low frequencies is not a problem unless there are low-frequency noise sources present (due to electronics, laser-intensity fluctuations, etc.). In this study there was little problem in obtaining and measuring low-frequency Doppler signals except for the case where the Doppler signal was intermittent (Doppler signal intermittency is discussed in the next section). For this case a persistent noise source centered around 120 hz appeared in the multichannel-analyzer spectra. Figure 28 indicates a slight peak due to this noise effect, while Fig. 29 depicts a spectra in which the 120-hz noise peak was more pronounced. Because the frequency of this noise source was of the same magnitude as the range of Doppler frequencies, it was not possible to filter it out with the bandpass filter.

Another effect noted with the LDV system when measuring in the convection cell was movement of the beams forming the scattering volume

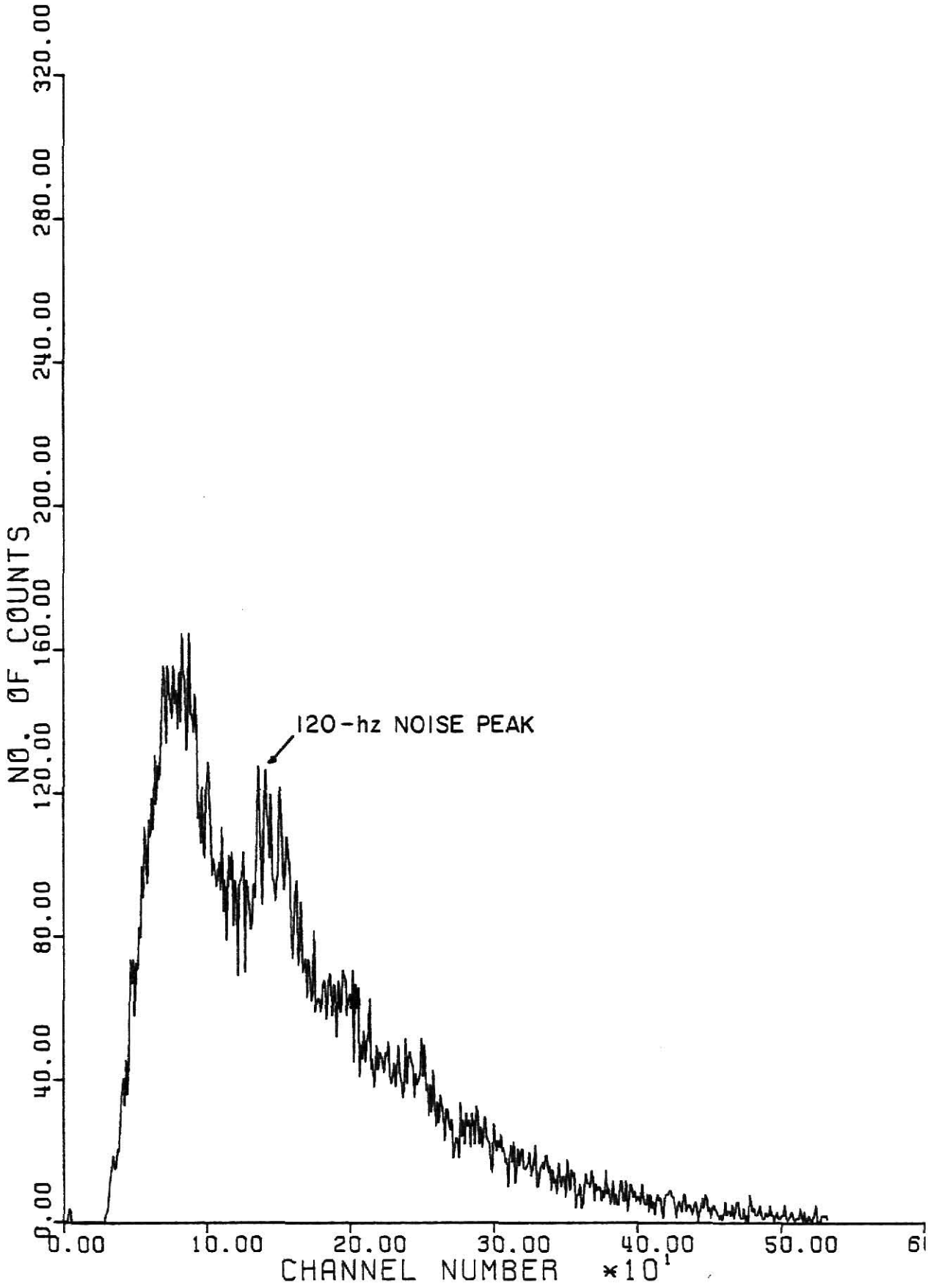

Fig. 29. Multichannel Analyzer Spectrum, Experimental Run Run No. 28 (Z = 10.16 cm), Z/L = .20.

due to temperature-induced refractive index gradients in the cell. Although this created some ambiguity in the knowledge of the exact location of the scattering volume, this effect was not considered to be significant. Durrani and Greated (1977) quote an analysis performed by Jonsson (1974, as quoted in the reference by Durrani and Greated) in which Jonsson calculated that for a beam passing through a 0.5-m water channel with a temperature fluctuation in the range of 20-21 C one might expect total rms (root-mean-square) beam deflections of the order .1 mm.

The effect of refractive-index gradients on the Doppler signal was also considered negligible. For example, using a table for the refractive index of pure water given in the reference edited by Weast (1975) one can calculate that the percent difference in the refractive index for pure water at 15 C and 50 C is only .34%. Insofar as the greatest temperature difference measured between the upper and lower plates in this study was about 20 C, the effect of refractive-index fluctuations on the Doppler signal was not important.

All of the effects mentioned in this section will be further illustrated in the next section in which a discussion of the velocity profiles obtained from the convection cell is presented.

4.3 Discussion of Convection Cell Velocity Profiles

One immediate observation that can be made from the convection cell velocity profiles presented in Figs. 20-26 is that velocities were obtained below the boundary separating the lower conductive heat-transfer sublayer from the upper predominantly convective heat-transfer

sublayer as predicted by the Baker, Faw, and Kulacki model. Yet the velocities did decrease as measurements were made closer to the bottom of the cell for all experimental runs (except for the profile depicted in Fig. 26 - this profile will be discussed later on in this section).

In all of the negative external-Rayleigh number experimental runs (depicted in Figs. 20-24) measurements close to the bottom of the cell were not limited by any of the physical limitations discussed in Sect. 4.2 but by the presence of an intermittent Doppler signal. As mentioned in the previous section, an intermittent Doppler signal resulted in the recording of a 120-hz noise peak in the multichannel-analyzer spectrum. When signal dropout became significant, the 120-hz noise peak precluded any accurate measurement for the average velocity. Thus a point was reached where further measurements for the average velocity close to the bottom of the cell was pointless (it should be noted that Fig. 29 represents one of the worst cases of 120-hz noise contamination. Even if no noise had been present, any value for the average velocity in an intermittent-flow regime obtained with the signal analysis system employed in this study would have been in error as there exists no procedure for taking into account zero velocity inasmuch the signal analysis system was developed for continuous signals. For accurate measurements to be made in the intermittent regime a temporal history of the velocity fluctuations must be recorded.

The question arises as to the origin of the intermittent Doppler signals below or around the η_{BFK} boundary line in Figs. 20-24. A possible answer can be derived from the study carried out by Adrian (1975) which was discussed in Sect. 1.2.2. In this study Adrian measured the velocity fluctuations across the interface that exist in the stable conduction layer and the convection layer for the turbulent convective flow-field present in water over ice. Adrian quoted Townsend (1964) as stating that these fluctuations were due to fluid impactions on the base of the stable conduction region whose spread is predominantly horizontal. A similar penetrative convection effect appears to be occurring at the boundary between the conduction sublayer and the convection sublayer as predicted by the Baker, Faw, and Kulacki model.

Near the top of the convection cell the vertical velocities decrease in a similar fashion (as shown in Figs. 20, 21, and 25) as the measured velocities near the bottom of the cell, although the decrease is less dramatic. It is believed that the vertical velocity decreases near the top plate due to the rising fluid impacting the top plate and spreading out in the horizontal direction. This would seem to account for the decreasing vertical-velocity component near the top plate assembly shown in the 5.08-cm layer height experimental runs.

In contrast with the negative external-Rayleigh number experimental runs, no noise problems were encountered making velocity measurements for positive external-Rayleigh number runs. The resulting velocity

profiles for the two positive external-Rayleigh number runs are presented in Figs. 25 and 26. With the absence of noise, measurements were made as close to the bottom of the cell as possible until the physical limitations discussed in Sect. 4.2.2 prevented any further measurements. This lack of a stable lower sublayer agrees with Boon-Long's (1978) results in which he found that η_{BFK} tended to overpredict the experimental value for η for positive external-Rayleigh number experimental runs. Because of this Boon-Long conjectured the presence of destabilizing forces in the lower sublayer; the results of this study tend to confirm this hypothesis.

Figure 26 depicts a profile different from any of the other profiles in that the average velocities went through a minimum near the bottom of the convection cell, and then increased. One possible explanation for this behavior is that movement of the convection cell for the last two measurements shifted the fluid-flow patterns in the convection cell such that the last two measurements were made in a region of higher fluid-flow velocity than the previous measurements (this shifting of fluid-flow patterns did occur in several runs not reported in this study, causing erratic variations in the measured average velocities in the fluid layer). Another possible explanation can be offered with the help of Fig. 19. Note that experimental run number 25 occurred very near the line of zero downward heat flux. Thus it is possible that the fluid layer in this run was heated by both internal heat sources and by the bottom plate assembly. It is

conceivable, then, that with additional heat being added to the fluid layer from the bottom plate convective fluid motion occurs next to the bottom plate in which the fluid rises to a boundary defined by the minimum velocity in Fig. 26, transfers heat to the descending fluid in the upper fluid layer, and then sinks to the bottom of the convection cell to start the process over. With only one measurement, however, it is not possible to state definitively that this is the case.

Because of the turbulence-induced broadening of the multichannel-analyzer signal, it is not possible to definitively relate the TAC non-linear conversion errors obtained with the rotating glass-plate experiments to the velocity results obtained in the convection cell. Because of this and the difficulty encountered in some runs in separating the Doppler signal from the pedestal portion of the signal, the best error estimate that can be applied to the data obtained in this study is $\pm$ 10%, which is the worst error obtained with the rotating glass-plate data.

The uncertainties associated with the evaluations of η_{BFK} (as shown in Figs. 20-26) were evaluated by first estimating the uncertainties present in each calculation for the internal Rayleigh number (Ra_{KG}) and the external Rayleigh number (Ra_E) and using the resulting minimum and maximum Rayleigh number values in Eq. (11) to find the minimum and maximum values for η_{BFK}. In the calculation of the Rayleigh numbers uncertainties existed in the property values of the

fluid used (due to the fact that pure water property values were used rather than values for copper sulfate solutions), in the measurement of temperatures, with the fluid layer depth (L), and in the calculated power density in the fluid.

Boon-Long (1978) estimated the maximum error in the property values used in the calculation of the Rayleigh numbers to be of the order of 2%. He based his estimation on comparison of the properties of pure water and copper sulfate solutions. Boon-Long's estimation of the maximum uncertainty associated with the property values used in the Rayleigh number calculations was used for this study because of the similar approach to the use of the convection cell apparatus.

In the same study Boon-Long also estimated the maximum uncertainty in the calculated power density to be of the order of 2%, primarily due to uncertainties in the measurement of the cell power by the watt transducer and to uncertainties in the measurement of the cell volume and height. According to Boon-Long the maximum error associated with the measurement of the fluid layer depth was estimated to be approximately 1.2% based on the 1.27 cm-layer height. Again, because of a similar approach in the use of the convection cell in this study, the previously mentioned uncertainties for the power density and the fluid layer depth were used in this study as well.

In Boon-Long's study the maximum uncertainty in the measured temperature difference between the upper and lower copper plates was estimated to be 2.2% for the $0.5^{\circ}C$ temperature difference.

Tests carried out with an ice-water bath in the convection cell indicated that the uncertainties in the measured temperatures for this study are somewhat larger, approximately 3%.

Once the uncertainties had been estimated, the combined uncertainty was calculated using the following equation:

$$\sigma^2 (f(x_1,x_2,\ldots,x_n)) = \sum_{i=1}^{n} \sigma^2(x_i) \left(\frac{\partial f}{\partial x_i}\right)^2 . \qquad (13)$$

Equation (13) was then applied to Eqs. (2) and (3) where it was found that the maximum uncertainty associated with each Rayleigh number calculation was approximately 7%. The resulting minimum and maximum values for the Rayleigh numbers were then used in Eq. (11) in order to evaluate for the minimum and maximum values for η_{BFK} shown in Figs. 20-26.

5.0 CONCLUSIONS AND RECOMMENDATIONS

A LDV system has been designed, tested, and used to measure the vertical velocity components present in a fluid layer with internal heat sources. To the extent that this work has documented some of the convective motion inside such layers, the assumptions of the conceptual model of Baker, Faw, and Kulacki (1976) may be tested for the first time. The salient conclusions of the study with regard to both the operation of the LDV system used by the author and to the extent to which several assumptions of the Baker, Faw, and Kulacki model are in agreement with the observed phenomena are now presented.

5.1 LDA System

The LDA system developed for this study was able to obtain adequate values of average velocity for measurements made with the rotating glass plate and for measurements made in the convection cell. However, if it is desired to both improve the accuracy of the results as well as obtain other parameters of interest (such as turbulence intensity) in convection cell studies several changes should be implemented. These changes will be briefly detailed in the following paragraphs of this section.

First, and foremost, frequency shifting should be implemented because of the low fluid velocities present in any convection-cell velocity measurements. Frequency shifting allows easier separation of the Doppler signal from any unwanted components and provides a means for determining the direction of the fluid flow.

Despite the problems encountered in this study in making measurements close to the plates forming the fluid layer boundaries with a dual-beam optical configuration, it is not believed that it is necessary to employ a reference beam configuration (see Appendix A.4.1) to overcome this problem. The dual-beam (or real-fringe) mode is still preferred due to ease of alignment. A two-component real-fringe LDA system has been developed specifically for measurements in a convection cell by Adrian (1975). This system utilizes a three-beam equiangular optical configuration that permits measurement of the normal velocity component very near a wall. Two Bragg cells are used in this configuration so as to allow separation of the two velocity components being measured by electronic-filtering methods. Adrian's paper warrants careful consideration for any future attempts to measure velocity profiles in a convection cell.

The signal-analysis system developed for use in this study should not be employed if quantities other than the average velocity are desired due to the non-linear TAC conversion process. The type of signal-analysis instrumentation employed in any LDA study depends upon the type of signals that are to be analyzed; i.e., whether individual realization or continuous signals (see Appendix A.7) are to be used. It is recommended for convection cell work that individual-realization signals be used (i.e., seed the distilled water with artificial particles to the point that only one scattering particle exists in the scattering volume at any instant in time). Use of single-particle scattering

eliminates transit-time broadening (see Appendix A.8.2) of the Doppler signal and thus would allow easier evaluation of the turbulence parameters of interest.

Signal-analysis systems are commercially available that will analyze single-particle Doppler signals and reject Doppler signals created by two or more scattering particles in the scattering volume. They are relatively expensive; a more economical method might be to build a microprocessor-based signal analysis system similar to the one described in a paper by Kendell, et. al. (1977).

5.2 Convection Cell Measurements

This study obtained vertical-velocity profiles in the center of a fluid layer with unequal boundary temperatures and containing heat sources. These profiles demonstrate that the semi-empirical model described in Sect. 1.1 that was developed to model the heat transfer mechanism in the fluid layer is partially correct. For convection-cell conditions for which the external Rayleigh number is negative (i.e., upper fluid boundary hotter than lower fluid boundary) the velocity measurements indicate the existence of two sublayers; an upper convective region with a relatively stable region below it. No indication was found of a well-defined boundary between the upper and lower regions as predicted by the model. Experimental evidence indicates that fluid from the upper layer is convected into the lower layer; thus the assumption of an adiabatic boundary between the upper and lower sublayers is not strictly correct. No evidence was found of a stable layer for positive external-Rayleigh number experimental

runs. For this case the velocities did decrease near the bottom of the cell; however, at no measurement position in these experimental runs was signal dropout observed, which would have indicated some stability at the measurement point.

Recommendations for improving the measurements obtained in the convection cell have already been discussed in Sect. 5.1 which dealt with improvements of the LDA system. In addition to these improvements future studies should consider general observation of the fluid-flow profile throughout the cell using the technique described in the paper by Tritton and Zarraga (1967). In particular, the fluid-flow patterns should be looked at for the case of the fluid layer heated both internally and from below to determine if there exists two regions of convective flow.

REFERENCES

1. Adrian, R. J., "Turbulent Convection in Water Over Ice," J. Fluid Mech., 69, Part 4, 753-781 (1975).

2. Adrian, R. J., "A Bi-Polar Two Component Laser Velocimeter," J. Phys. E: Sci. Instrum., 8, 9, 723-726 (1975).

3. Adrian, R. J., and Earley, E. L., "Evaluation of LDV Performance Using Mie Scattering Theory," Proceedings of Minnesota Symposium on Laser Anemometry (available from Department of Conferences, University of Minnesota), 426-454 (1975).

4. Adrian, R. J., and Fingerson, L. M., Laser Anemometry...Theory, Applications, and Techniques, Thermo-Systems, Inc. (TSI) publication, 1976.

5. Adrian, R. J., and Goldstein, R. J., "Analysis of a Laser Doppler Anemometer," J. Phys. E: Sci. Instrum., 4, 505-511 (1971).

6. Amenitskii, A. N., Rinkevicyhus, B. S., Kirsanov, M. A., "Examination of Natural Convection with a Direction-Sensitive Doppler Velocimeter," High Temp. (USA), 12, 1, 205-207 (1974).

7. Amenitskii, A. N., Rinkevichus, B. S., and Solov'ev, G. M., "Measurements Using the Doppler Effect of Small Velocities in Flows Occurring in the Free Convection of Fluids," Soviet Physics - DokLady, 17, 11, 1078-1079 (1973).

8. Bajpai, A. C., Mustoe, L. R., and Walker, D., Advanced Engineering Mathematics, John Wiley and Sons, Ltd., Great Britain, 1977.

9. Baker, L. J., Faw, R. E., and Kulacki, F. A., "Postaccident Heat Removal - Part 1: Heat Transfer Within an Internally Heated Nonboiling Liquid Layer," Nuclear Science and Engineering, 61, 22-230 (1976).

10. Beesley, M. J., Lasers and Their Applications, Taylor and Francis Ltd., London, 1976.

11. Bergé, P. and Dubois, M., "Time Dependent Velocity in Rayleigh-Bernard Convection: A Transition to Turbulence," Optics Comm., 19, 1, 129 (1976).

12. Bernard, H., "Les Tourbillons Cellulaires dau une Nappe Liquide, Methods Optiques d'Observation et d'Enregistrement," J. de Physique, 10, 254 (1901).

13. Bevington, P. R., Data Reduction and Error Analysis for the Physical Sciences, McGraw-Hill Book Company, New York, 1969.

14. Boon-Long, P., "An Experimental Study of Convective Heat Transfer in a Horizontal Fluid Layer with Uniform Heat Sources," Ph.D. Dissertation, Kansas State University (1978).

15. Born, M., and Wolf, E., Principles of Optics, Pergamon Press, Oxford, 1970.

16. Brayton, D. B., "Small Particle Signal Characteristics of a Dual-Scatter laser Velocimeter," Appl. Opt., 13, 10, 2346-2351 (1974).

17. Brayton, D. B., Kalb, H. T., and Crosswy, F. L., "Two-Component Dual-Scatter Laser Doppler Velocimeter with Frequency Burst Signal Readout," Appl. Opt., 12, 6, 1145-1156 (1973).

18. Donohue, G. L, McLaughlin, D. K., and Tiederman, W. G., "Turbulence Measurements with a Laser Anemometer Measuring Individual Realizations," Phys. Fluids, 15, 11, 1920-1926 (1972).

19. Drain, L. E., "Coherent and Noncoherent Methods in Doppler Optical Beat Velocity Measurement," J. Phys. D., 5, 481-495 (1972).

20. Durrani, T. S., and Greated, C. A., Laser Systems in Flow Measurements, Plenum Press, New York, 1977.

21. Durst, F., "Development and Application of Optical Anemometers," Ph.D. Thesis, University of London (1972).

22. Durst, F., "Scattering Phenomena and Their Application in Optical Anemometry," ZAMP, 24, 619-643 (1973).

23. Durst, F., "Electronic Processing of Optical Anemometer Signals," Proceedings of the LDA Symposium Copenhagen (available from Technical University of Denmark), 208-250 (1975).

24. Durst, F., and Eliasson, B., "Properties of Laser Doppler Signals and Their Exploitation for Particle Size Measurement," Proceedings of the LDA Symposium Copenhagen (available from Technical University of Denmark), 457-477 (1975).

25. Durst, F., Melling, A., and Whitelaw, J. H., Principles and Practices of Laser-Doppler Anemometry, Academic Press, London, 1976.

26. Durst, F., and Stevenson, W. H., "Influence of Gaussian Beam Properties on Laser Doppler Signals," Appl. Opts., 18, 4, 516-524 (1979).

27. Durst, F., and Whitelaw, J. H., "Aerodynamic Properties of Separated Gas Flows; Existing Measurement Techniques and a New Optical Geometry for the Laser Doppler Anemometer," Prog. Ht. Mass Trans., 4, 311 (1971).

28. Eckert, E. R. G., and Drake, R. M., Analysis of Heat and Mass Transfer, McGraw-Hill Book Company, New York, 1972.

29. Eckert, E. R. G., and Goldstein, R. J., Measurements in Heat Transfer, Second Edition, Hemisphere Publishing Company, Washington, 1976.

30. Edwards, R. V., Angus, J. C., French, M. J., and Dunning, T. W., "Spectral Analysis of the Signal from the Laser-Doppler Flowmeter: Time-Independent Systems," J. Appl. Phys., 42, 837 (1973).

31. Eliasson, B., and Dändliker, R., "A Theoretical Analysis of Laser Doppler Flowmeters," Optica Acta, 21, 2, 119-149 (1974).

32. Garon, A. M., and Goldstein, R. J., "Velocity and Heat Transfer Measurements in Thermal Convection," Phys. Fluid, 16, 11, 1818-1825 (1973).

33. George, W. K., and Lumley, J. L., "The Laser-Doppler Anemometer and Its Application to Turbulence," J. Fluid Mech., 60, 321-362 (1973).

34. Kendall, C. K., Stock, D. E., and Rigas, H. B., "A Microprocessor-Based Signal Processing System for Laser Doppler Anemometry," Paper presented at Joint Automatic Control Conference (IEEE), San Francisco, Ca., 22-24, June 1977.

35. Kerker, M., The Scattering of Light and Other Electromagnetic Radiation, Academic Press, New York, 1969.

36. Kreith, F., Principles of Heat Transfer, Third Edition, Intext Educational Publishers, New York, 1973.

37. Kulacki, F. A., and Emara, A. A., "High Rayleigh Number Convection in Enclosed Fluid Layers with Internal Heat Sources," NUREG 75/065; Tech. Rep. 3952-1, Mech. Engg. Dept., Ohio State University (1975).

38. Kulacki, F. A., and Goldstein, R. J., "Thermal Convection in a Horizontal Fluid Layer with Uniform Volumetric Energy Sources," J. Fluid Mech., 55, Part 2, 271-287 (1972).

39. Lancaster, D., Active-Filter Cookbook, Howard W. Sams and Co., Inc., Indianapolis, 1975.

40. Maynard, J. A., Gaylord, T. K., and Rust, J. H., "Data Acquisition System for Laser Doppler Velocimeters," Rev. Sci. Instrum., 46, 11, 1469-1473 (1975).

41. Mazumder, M. K., "A Laser Doppler Measurement Without Directional Ambiguity By Using Frequency Shifted Incident Beams," Appl. Phys. Lett., 16, 11, 462-467 (1970).

42. Mazumder, M. K., "A Symmetrical Laser-Doppler Velocity Meter and Its Application to Turbulence Characterization," NASA CR 2031 (1972).

43. Mazumder, M. K., and Wankum, D. L., "SNR and Spectra Broadening in Turbulence Structure Measurements Using a CW Laser," Appl. Opt., 9, 3, 633-637 (1970).

44. Ning, K. S., "Theoretical Study of Stability in Horizontal Fluid Layers with Uniform Volumetric Energy Sources," M.S. Thesis, Kansas State University (1977).

45. Rudd, M. J., "A New Theoretical Model for the Laser Dopplermeter," J. Phys. E: Sci. Instrum., 2, 2, 55-58 (1969).

46. Schwiderski, E. W., and Schwab, H. J. A., "Convection Experiments with Electrolytically Heated Fluid Layers," J. Fluid Mech., 48, 703-719 (1971).

47. Steinberner, V., and Reineke, H.-H., "Turbulent Buoyancy Convection Heat Transfer with Internal Heat Sources," Sixth International Heat Transfer Conference, Part II, Toronto, Canada, August 1978, 305-310.

48. Stevenson, W. H., "Principles of Laser Velocimetry," AIAA Volume on Experimental Diagnostics in Gas Phase Combustion Systems, 53 (1977).

49. Townsend, A. A., "Natural Convection in Water Over Ice," Quart. J. Roy. Met. Soc., 90, 248 (1964).

50. Tritton, D. J., and Zarraga, M. N., "Convection in Horizontal Layers with Internal Heat Generation Experiments," J. Fluid Mech., 30, 21-31 (1967).

51. TSI News, published by Thermo Systems, Inc., (TSI) St. Paul, Minn. (January 1977).

52. Wang, C. P., "A Unified Analysis on Laser Doppler Velocimeters," J. Phys. E: Sci. Instrum., 5, 763-766 (1972).

53. Wang, C. P., and Synder, D., "Laser-Doppler Velocimetry: Experimental Study," Appl. Opt., 13, 1 98-103, (1974).

54. Watrasiewicz, B. M., and Rudd, M. J., Laser-Doppler Measurements, Butterworths, London-Boston, 1976.

55. Weast, R. C. (editor), Handbook of Chemistry and Physics, 56th Edition, CRC Press, Cleveland, 1975-1976.

56. Yeh, Y., and Cummins, H. Z., "Localized Fluid Flow Measurements with an He-Ne Laser Spectrometer," Appl. Phys. Letters, 4, 10, 176-178 (1964).

ACKNOWLEDGEMENTS

The author would like to express his deep gratitude to Dr. Thomas W. Lester, major advisor, for his guidance and support throughout this study. His calm and professional manner in reducing many problems to their true level of significance will always be remembered.

Thanks is extended to Y. Pan, friend and officemate throughout this study, for putting up with sometimes unreasonable demands for lab time and for quickly understanding when an alignment on his apparatus was inadvertently jarred. Thanks is also extended to S. Kemnitz, typist of this manuscript, who made special efforts in her work with this manuscript, and to Bill Starr, whose help in dealing with equipment problems was much appreciated. Deep appreciation and gratitude is extended to two very special people, Steve and Deb Vaughn. Their support and understanding in putting up with a houseguest who stayed longer than anyone planned will never be forgotten.

Finally, the author would like to thank his parents for their patience, support, and love throughout this project.

Appendix A

Laser-Doppler Anemometry

A.1 Introduction

Laser-Doppler anemometry (LDA) is a method of making non-obstrusive velocity measurements in fluid flows using the principle of the Doppler shift. It was first demonstrated successfully in 1964 by Yeh and Cummins (1964). Since that first demonstration, the use of LDA systems has greatly increased in popularity primarily because it is a way of making local velocity measurements without disturbing the fluid-flow pattern. In addition, there is a simple linear relationship between the signal and the velocity being measured.

Nevertheless, LDA does have its disadvantages. One is that since it is a technique that relies upon laser-light scattering, the medium in which velocity measurements are to be made must be able to transmit light. Another disadvantage, which may or may not be a problem, is that the technique of LDA involves velocity measurements not of the fluid itself but of small particles which are suspended in the fluid flow. Thus the researcher using LDA to make velocity measurements must always make sure the particles being used to make velocity measurements follow the flow pattern faithfully.

The purpose of this appendix is to present a brief review of some of the theory and practices associated with laser Doppler anemometry. It is by no means comprehensive, and for more extensive details the following four basic LDA references can be used: 1) Principles and Practices of Laser-Doppler Anemometry, by F. Durst, A. Melling, and J. H. Whitelaw (1976), 2) Laser Systems in Flow Measurements, by T. S. Durrani and C. A. Greated

(1977), 3) Laser Anemometry ... Theory, Applications, and Techniques, by R. J. Adrian and L. M. Fingerson (1976) and 4) Laser Doppler Measurements, by B. M. Watrasiewicz and M. J. Rudd. Other papers and conference proceedings are mentioned in these four basic references as well as in the remainder of this appendix.

A.2 Doppler Shift

As its name implies, LDA relies upon the Doppler shift for the measurement of local fluid velocities. When electromagnetic radiation is scattered from a moving object it undergoes a frequency shift which is proportional to the velocity of the moving particle. In Fig. A.1 plane, monochromatic light waves are being emitted by a stationary light source. A particle passes through the light beam, its speed and direction of travel given by the velocity vector $\vec{V}$. The interaction of the particle with the light beam causes light to be scattered in the direction given by the scattered wave propagation vector $\vec{k}_s$. With the assumption that the speed of the particle is much smaller than the speed of light, the following mathematical relationship can be derived between the velocity of the particle and the magnitude of the frequency shift of the scattered light:

$$\nu_D = \frac{\vec{V}\cdot(\vec{k}_s - \vec{k}_i)}{2\pi} \qquad (A.1)$$

Equation (A.1) relates the magnitude of the Doppler shift to the velocity component of $\vec{V}$ in the direction $(\vec{k}_s - \vec{k}_i)$.

The magnitude of the frequency shift as given by Eq. (A.1) is very small compared to the source frequency because the speed of the particle is

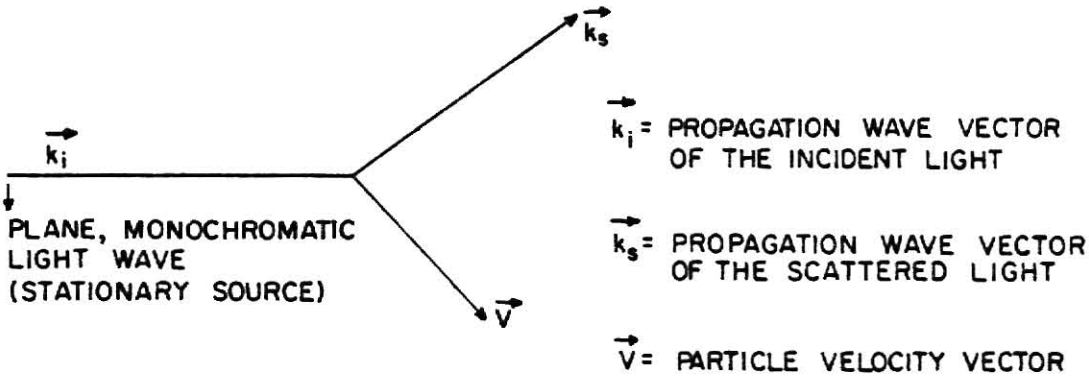

Fig. A.1 Doppler Effect.

much smaller than the speed of light. The best spectroscopic techniques in use today can detect frequency shifts on the order of one part in 150 million, which rules out direct measurement of the magnitude of the Doppler shift for most fluid flows of interest. Instead the measurements must be made using the technique of optical mixing (or optical heterodyning), the subject of the next section.

A.3 Optical Mixing

In LDA systems optical mixing occurs when the Doppler-shifted light is combined with a coherent reference beam of light on the surface of a photodetector. As an example, consider the case in which the Doppler-shifted light is combined with light of the original frequency on the surface of a photomultiplier (PM) tube. For simplicity, the two light beams will be considered to be plane, linearly polarized, and coaxial. By letting $\Omega_1 = 2\pi\nu_i$ and $\Omega_2 = 2\pi(\nu_i+\nu_D)$, the electric field distributions of the two light beams on the surface of the PM tube can be written as

$$E_1\ (x_1,t) = E_{01} \sin\ [\omega_1 t - (kx_1 + \varepsilon_1)]\ , \qquad (A.2)$$

and

$$E_2\ (x_2,t) = E_{02} \sin\ [\omega_2 t - (kx_2 + \varepsilon_2)\ , \qquad (A.3)$$

where E_{01} and E_{02} are the amplitudes of the two harmonic disturbances propagating in the x-direction, ε_1 and ε_2 are the initial phases or epoch angles of the two beams, and x_1 and x_2 are the distances from the sources of the two light beams to the surface of the PM tube. Let

$$\alpha_j\ (x,\varepsilon) = -\ (kx_j + \varepsilon_j)\ , \quad j = 1,2 \qquad (A.4)$$

where α is known as the phase of the wave and is assumed constant in this derivation. Equations (A.2) and (A.3) can be rewritten as

$$E_1(x_1,t) = E_{01} \sin [\omega_1 t + \alpha_1] , \tag{A.5}$$

and

$$E_2(x_2,t) = E_{02} \sin [\omega_2 t + \alpha_2] . \tag{A.6}$$

The resultant electric field disturbance on the surface of the PM tube is simply the linear superposition of E_1 and E_2, i.e.,

$$E_R = E_{01} \sin (\omega_1 t + \alpha_1) + E_{02} \sin (w_2 t + \alpha_2) . \tag{A.7}$$

The PM tube is a square-law detector in that it detects the intensity of the light which falls upon its surface. Thus the output current from the PM tube is proportional to the square of the total electric field incident upon it. The output current can therefore be written as

$$i(t) \alpha [E_{01} \sin (\omega_1 t + \alpha_1) + E_{02} \sin (\omega_2 t + \alpha_2)]^2 . \tag{A.8}$$

Equation (A.8) can be expanded to the following form with the substitution of the appropriate trigonometric identities:

$$i(t) \alpha \frac{E_{01}^2}{2} [1 - \cos^2 (\omega_1 t + \alpha_1)] + E_{01} E_{02} \{\cos[(\omega_1 t - \omega_2 t) + (\alpha_1 - \alpha_2)] - \cos[(\omega_1 t + \omega_2 t) + (\alpha_1 + \alpha_2)]\} + \frac{E_{02}^2}{2} [1 - \cos 2(\omega_2 t + \alpha_2)] . \tag{A.9}$$

The frequency of visible light is of the order 5×10^{14} hz. A PM tube cannot detect frequencies of that magnitude, so it will time-average the terms in Eq. (A.9) containing frequencies of the order ν_i.

Consequently the cosine terms in Eq. (A.9) containing frequencies of the order ν_i will not appear in the PM tube output since their time-average is zero. If the magnitude of the Doppler shift frequency is small enough, it will be transmitted by the PM tube. For this case the output current as given by Eq. (A.9) reduces to the following form:

$$i(t) \alpha \frac{E_{01}^2 + E_{02}^2}{2} + E_{01} E_{02} \cos [2\pi\nu_D t + (\alpha_1 - \alpha_2)] . \quad (A.10)$$

As is illustrated by Eq. (A.10) the total output signal from the PM tube due to the optical-heterodyning (or mixing) effect consists of a dc part due to the total instantaneous light incident upon the surface of the PM tube plus an ac signal whose amplitude is modulated by the magnitude of the Doppler shift. Once this frequency has been determined Eq. (A.1) can be used to determine the value of the velocity component being measured. Notice in Eq. (A.10) that the maximum depth of modulation occurs for equal intensities of mixing lights. This has important consequences in the design of LDA systems in that LDA optical configurations employ nearly equal intensity light beams so as to obtain high-quality signals at the photodetector.

Equation (A.10) contains information crucial to the successful operation of a LDA system. It is assumed in the derivation of Eq. (A.10) that the phases of the two light beams mixing on the surface of the photodetector are constant. This implies that their phase difference is constant as well. If this phase difference is not constant the frequency of the signal output from the PM tube depends not only on the value for ν_D but also on the value for $(\alpha_1 - \alpha_2)$. This effect contaminates the measurement for ν_D.

In LDA systems unwanted phase fluctuations can occur due to vibrations, laser incoherence, or refractive index fluctuations in the fluid. The effect of laser incoherence can best be seen by rewriting the phase-difference term in Eq. (A.10) as

$$(\alpha_1-\alpha_2) = (kx_1-kx_2) + (\varepsilon_1-\varepsilon_2) \ , \qquad (A.11)$$

or

$$(\alpha_1-\alpha_2) = \frac{2\pi}{\lambda} (x_1-x_2) + (\varepsilon_1-\varepsilon_2) \ . \qquad (A.12)$$

Light waves for which $(\varepsilon_1-\varepsilon_2)$ is constant are said to be coherent, regardless of its value. If the light source used in LDA work were not coherent, the effect of the fluctuating value for $(\varepsilon_1-\varepsilon_2)$ would prevent measurement for the Doppler frequency ν_D. Thus, successful operation of a LDA system requires the use of coherent light beams.

The term (kx_1-kx_2) in Eq. (A.11) represents the optical path-difference between the two light-beam paths. This optical path-length difference must be less than the coherence length of the light beams or, again, the phase difference term $(\alpha_1-\alpha_2)$ becomes time-dependent. The subject of coherence is discussed further in Section (A.5).

Vibrations and refractive index fluctuations can cause additional time-dependent optical path-length differences to occur. It is necessary therefore that all optics and the laser be mounted on vibration-free surfaces. Refractive index fluctuations are usually not a problem unless there is a steep temperature gradient present in the flow field being measured. Generally speaking, the most troublesome aspect of vibrations and refractive index fluctuations is the problem in determining the point at which the velocity measurements are being made.

A.4 LDA Optical Systems

Three basic LDA systems have been developed utilizing the principle of optical heterodyning. A discussion of these three systems is presented in this section.

A.4.1 Reference-Beam System

The reference beam system, known also as the local oscillator system or the virtual fringe system, was the first type of LDA system to be developed (Yeh and Cummins, 1964). As shown in Fig. A.2a, the laser beam is first split into two separate beams, a weak reference beam and an intense scattering beam. The two beams are focused to a common intersection point so as to form an intense light-scattering volume. From the scattering volume the reference beam continues on to the surface of the photodetector. When a particle traverses the scattering volume it scatters light from the scattering beam. A portion of this scattered light then combines with the reference beam on the photodetector surface to yield an output signal whose frequency is equal to the magnitude of the Doppler shift (as derived in the previous section on Optical Mixing).

Using Fig. A.2b the frequency of the output signal from the photodetector can be related to the particle velocity using the Doppler model. Light scattered from beam 1 has undergone a frequency shift as a result of the scattering process such that its frequency in the direction of $\hat{s}_1$ is

$$\nu_1 = \nu_0 + \frac{\vec{v} \cdot (\hat{r}-\hat{s}_1)}{\lambda} . \qquad (A.13)$$

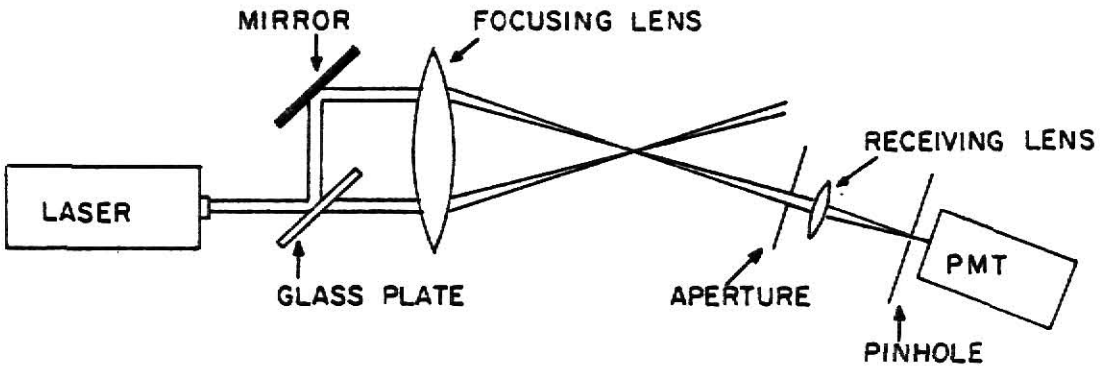

Fig. A.2.a. Reference-Beam Optical Configuration (from Wang, 1972).

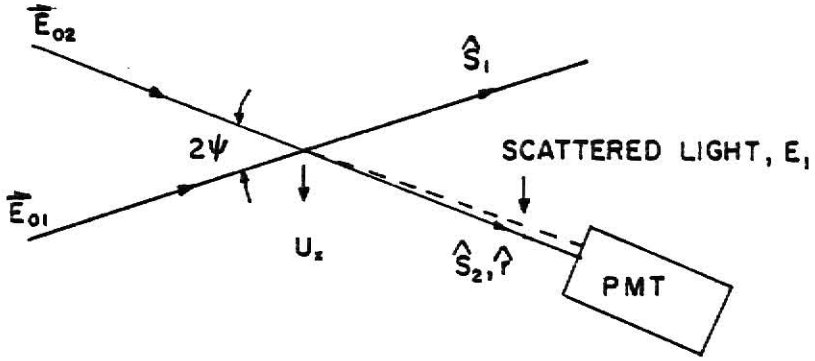

Fig. A.2.b. Reference-Beam Optical Heterodyning Arrangement.

The scattered light from beam 1 is then combined on the surface of the photodetector with the unscattered light from beam 2. The output signal from the photodetector has a frequency which is equal to the difference in frequency between the scattered light from beam 1 and the unscattered light from beam 2, or

$$\nu_D = \frac{\vec{v} \cdot (\hat{f}-\hat{s}_1)}{\lambda} . \qquad (A.14)$$

Equation (A.14) relates the frequency of the output signal from the photodetector to the component of the particle velocity in the direction $(\hat{f}-\hat{s}_1)$. This direction is perpendicular to the bisector or beams 1 and 2 in Fig. A.2b. Thus, Eq. (A.14) can be simplified to the following form:

$$\nu_D = \frac{2v_x \sin \theta}{\lambda} \qquad (A.15)$$

Notice in Fig. A.2a that an aperture is placed before the receiving lens in front of the photodetector. One purpose this aperture serves is to limit the spatial region that the photodetector sees. In other words, the photodetector should collect light from the immediate region of the scattering volume and not, for example, stray light reflections from the room in which the measurements are being made. Another very important purpose of the aperture is related to spatial coherence. The importance of spatial coherence is dealt with in Section A.5.

In addition to the four basic LDA references given in Section A.1, other worthwhile analyses for reference-beam systems are those of Adrian and Goldstein (1971), and George and Lumley (1973), and Eliasson and Dändliker (1974).

A.4.2 Dual-Beam System

The dual-beam (or fringe) system was first proposed in 1969 by Rudd (Rudd, 1969). Figure A.3a depicts the basic optical configuration of the dual-beam system. As shown in this figure two light beams of equal intensity are focused to form a scattering volume. When a particle traverses the scattering volume it scatters light from both beams. Only the scattered light is collected and focused on the surface of the photodetector. Note that by using a single lens to focus the two light beams light scattered from one beam is automatically injected into the scattered light from the second beam.

The Doppler model can be used in conjunction with Fig. A.3b to predict the frequency of the signal obtained from the photodetector. Light scattered from beam 1 has undergone a frequency shift caused by the scattering process such that the frequency of the scattered light in the direction $\hat{s}_1$ is

$$\nu_1 = \nu_0 + \frac{\vec{v} \cdot (\hat{r}-\hat{s}_1)}{\lambda} . \qquad (A.16)$$

Likewise, the light scattered from beam 2 in the direction $\hat{s}_2$ has a frequency equal to

$$\nu_2 = \nu_0 + \frac{\vec{v} \cdot (\hat{r}-\hat{s}_2)}{\lambda} . \qquad (A.17)$$

The output signal from the photodetector has a frequency equal to the difference in frequency between ν_1 and ν_2, or

$$\nu_D = \frac{\vec{v} \cdot (\hat{s}_2-\hat{s}_1)}{\lambda} \qquad (A.18)$$

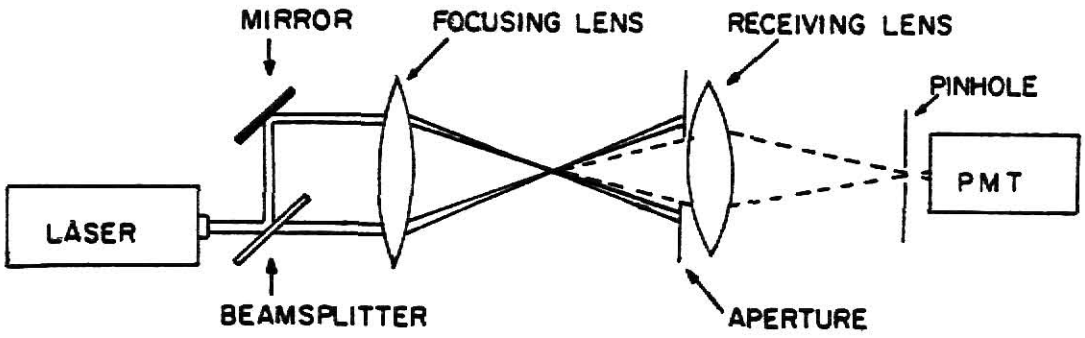

Fig. A.3.a. Dual-Beam Optical Configuration (from Wang, 1972).

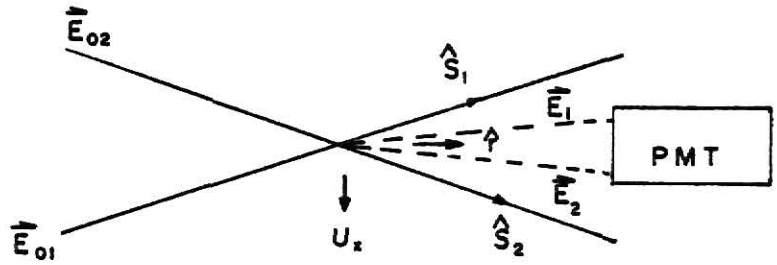

Fig. A.3.b. Dual-Beam Optical Heterodyning Arrangement.

The component of the particle velocity measured is in the direction given by (s_2-s_1), which is the direction perpendicular to the bisector of beams 1 and 2. This is the direction given by v_x in Fig. A.3b, so Eq. (A.18) can be reduced to

$$\nu_D = \frac{2\ v_x\ \sin\theta}{\lambda} \qquad (A.19)$$

Notice in both Eq. (A.18) and Eq. (A.19) that the expression for ν_D is independent of the direction of observation (unlike the reference-beam system). This has important consequences in the size of the aperture opening that is used. The size of the aperture opening is dealt with in more detail in Section A.5.

When Rudd first proposed the dual-beam system he also proposed the fringe model as an alternate way of explaining the signal obtained from the photodetector. When two coherent light beams intersect they interfere constructively and destructively to form a stationary fringe pattern in the scattering volume. When a particle in the fluid flow traverses the scattering volume (and hence the fringe pattern) the intensity of the scattered light that falls upon the photodetector varies at a rate that is directly proportional to the particle velocity. It can be shown that the fringe spacing in the measuring volume is (Rudd and Watrasiewicz, 1976)

$$d = \frac{\lambda}{2\ \sin\theta}\ . \qquad (A.20)$$

If the particle is traveling in a direction perpendicular to the fringes with a speed V, the frequency of the observed signal from the photodetector will be related to the particle speed as follows:

$$\nu_D = \frac{V}{d} = \frac{2V\sin\theta}{\lambda} \quad . \tag{A.21}$$

Equation (A.21) agrees with Eq. (A.19), so the Doppler and fringe models agree on the form of the evaluation equation to be used in calculating velocities.

The dual-beam system will be discussed in greater detail in the subsequent sections of this appendix. More detailed analyses of the dual-beam mode are given in the four basic references cited in Section A.1. Other helpful discussions may be found in Adrian and Earley (1975), Brayton (1974), Brayton, Kalb, and Crosswy (1973), and Eliasson and Dändliker (1974).

A.4.3 Dual-Scatter System

As shown in Fig. A.4 this LDA optical configuration employs a single focused laser beam directed into the fluid flow. Scattered light then collected from two different directions (usually in a symmetric fashion about the system optical axis) by a large lens and two aperture openings. The collected light is then mixed on the surface of the photodetector. Theoretically, this system is an exact inverse of the dual-beam system.

The dual-scatter system offers no clear advantage over the dual-beam system and is used infrequently by LDA researchers. A more complete description of this optical configuration can be found in papers by Mazumder and Wankum (1970), Durst and Whitelaw (1971), and Mazumder (1972).

A.5 Coherence Effects and Requirements

Coherence effects and requirements play an important role in the

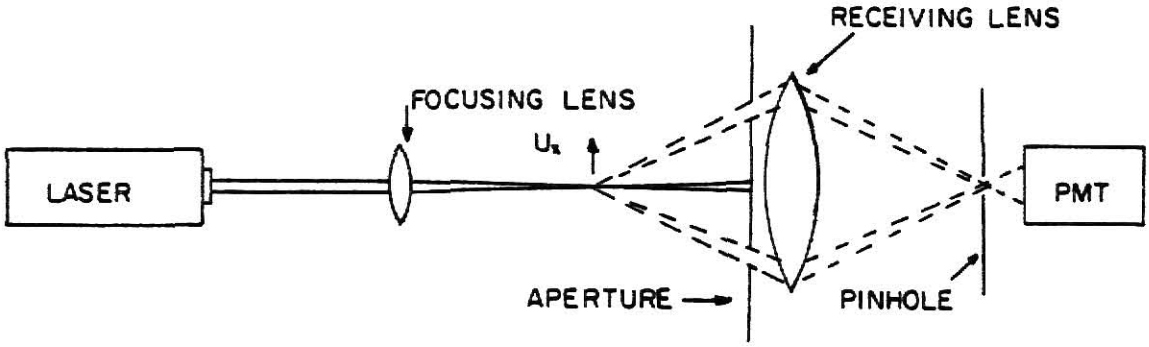

Fig. A.4. Dual-Scatter Optical Configuration.

successful operation of a LDA system. Simply speaking, coherence implies the ability to predict both the amplitude and phase of an electromagnetic wave. Coherence has already been mentioned in Section A.3 in which it was shown that waves which possessed constant phase relationships with each other were said to be coherent, and that waves which possessed random phase relationships were incoherent. Two intersecting, coherent light beams of equal frequency interfere at the point of intersection to form a stable fringe pattern. This does not mean that two incoherent light waves cannot interefere with each other to form fringe patterns. However, for the case of two incoherent, interfering light waves the resultant fringe pattern can only be observed during the time of one wave train ($\sim 10^{-8}$ sec for thermal light sources). The random phase-difference fluctuations present between the two incoherent light waves causes random shifts in the spatial position of the fringe pattern; thus over the observation period of the eye or the photodetector the fringe patterns smear out. For this case the interference term in Eq. (A.10) averages to zero, so that the expression for the output current reduces to

$$i(t) \propto \frac{E_{01} + E_{02}}{2} \propto \frac{I_{01} + I_{02}}{2} \qquad (A.22)$$

Thus, for superposition of coherent waves on the surface of a photodetector it is necessary to first add the complex amplitudes before squaring to obtain the resultant intensity, while for incoherent waves it is only necessary to add the individual intensities.

Coherence has meaning in both space and time. Light is said to be spatially coherent if the wavefronts remain constant in time (a wavefront

is defined to be the surface formed by points of equal phase). Lasers have excellent spatial-coherence properties, and well designed lasers can maintain spatial coherence indefinitely. Laser light can be considered to have the same spatial coherence as radiation from a point source at infinity.

Light is said to be temporally coherent if it has very nearly a single frequency (the spread in frequency or bandwidth is small). Temporal coherence describes the phase coherence in the direction of propagation. There are no sources of light which radiate at a single frequency. However, a laser with its very narrow bandwidth, approximates a monochromatic source and thus has a relatively long coherence time. The coherence length, which represents the length of an uninterrupted wave train, is found by taking the product of the coherence time and the speed of light. For lasers, this value can be as much as 50 km (Beesley, 1976). One consequence of the finite coherence length of lasers used in LDA systems that employ fringe patterns is that any optical path length difference introduced between the two beams should be less than the coherence length of the laser, or clear fringes will not be formed in the scattering volume.

It is worthwhile noting at this point that it is possible to obtain coherent light for LDA systems using a thermal light source. It is necessary to use a pinhole, filter, and lens to obtain the necessary planar, monochromatic light (see Fig. A.5). The problem with coherent light obtained in this manner is that the scattered light intensity produced is considerably less than that which is obtained from lasers. Thus,

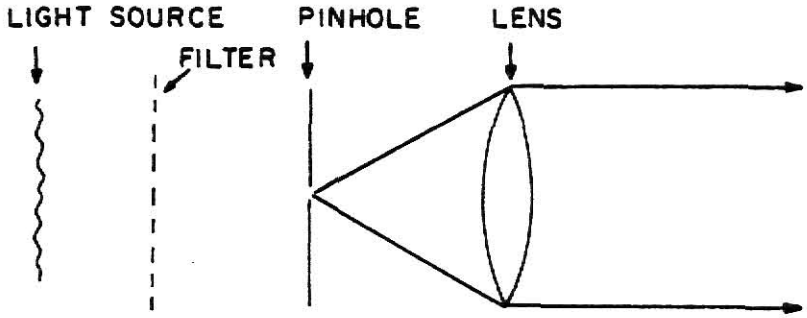

Fig. A.5. Production of Coherent Light From an Incoherent Source (from Beeslen, 1976).

the two reasons for using lasers in LDA systems is because of their excellent coherence properties and because they are intense sources of light.

When selecting a laser for a LDA system it must be remembered that higher-powered lasers have shorter coherence lengths. This is because the increase in amplification is provided by an increase in the number of axial modes present in the laser output (Durst, Melling, and Whitelaw, 1976). This increases the bandwidth of the laser light. The bandwidth is related to the coherence length as follows:

$$l_c = \frac{1}{\Delta f} . \qquad (A.23)$$

Thus increasing the bandwidth has the effect of reducing the coherence length of the laser. This must be taken into account when unequal path lengths are to be traveled by the laser beams.

In Section A.4.1 it was mentioned that one reason for the aperture in front of the receiving lens for reference-beam and dual-beam systems was to limit the spatial region of observation seen by the PM tube. With the aperture spurious light sources such as laser light reflections cannot substantially contribute to the noise present in the output signal. Another purpose of the aperture is related to spatial coherence. It is important that the instantaneous phase difference between the two combining light waves does not vary appreciably over the photodetector observation area. The use of a single transmission lens for the dual-beam system to form the scattering volume causes the scattered light from one beam to be automatically injected into the scattered light from the second

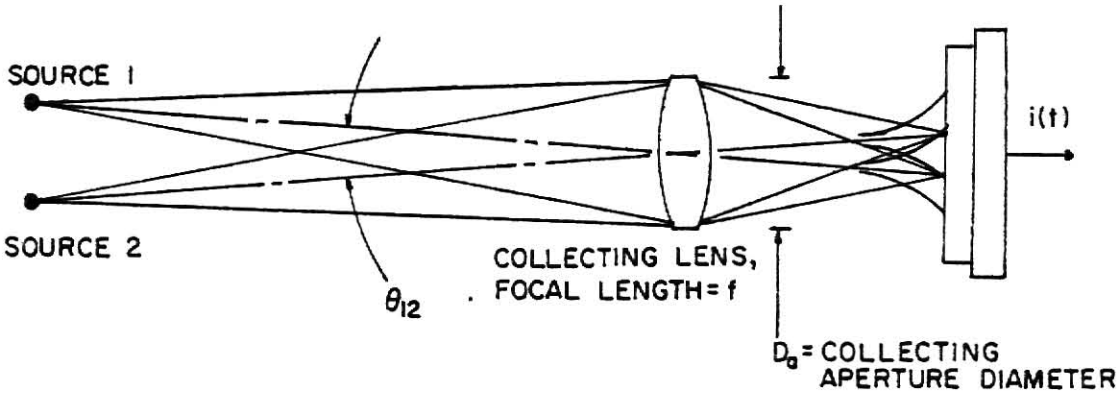

Fig. A.6. Source/Aperture Coherence Factor (from Adrian and Fingerson, 1977).

beam. Thus the spatial coherence criteria is automatically satisfied for dual-beam systems. Because of this, the aperture size for dual-beam systems can be increased substantially over that possible with reference-beam systems, so more of the scattered light can contribute to the signal. This is an important advantage for the dual-beam system over the reference-beam system.

Coherence is also used to describe the type of detection that is occurring, depending on the type of LDA system that is being used. Non-coherent detection refers to the mixing of two light-beams scattered from one particle, while coherent detection refers to the mixing of two light-beams scattered by two particles separated in space (Drain, 1972). Figure A.6 can be used to explain these concepts further. For the coherent detection case the light scattered from each individual particle is imaged into an Airy pattern on the photodetector surface, and these patterns must be focused by the receiving optics so that overlap occurs. Overlap between two patterns occurs if the following aperture coherence criterion is satisfied (refer to Fig. A.6) (Adrian and Fingerson, 1977):

$$\theta_{12} < \frac{\lambda}{D_a} . \qquad (A.24)$$

Thus the diameter of the receiving aperture for LDA systems that employ coherent detection methods must satisfy the following inequality:

$$D_a < \frac{\theta_{12}}{\lambda} . \qquad (A.25)$$

Dual-beam scattered-light signals due to a single particle automatically satisfy the aperture coherence criterion (the two scattered

light-waves originate from the same point, so $\theta_{12} = 0$). Thus single-particle scatter in dual-beam systems results in non-coherent detection by the photodetector. With low enough particle concentrations no coherent contributions to the dual-beam system are present because the aperture is usually too large. Coherent contributions to the total signal at the PM tube can occur in dual-beam systems if the particle concentrations is high enough.

Reference beam systems produce only coherent signals. Thus the diameter of the aperture employed in the receiving optics must satisfy the inequality given in Eq. (A.25). This limitation severely limits the amount of signal that can be used, and is one reason why dual-beam systems are much more popular than reference-beam systems.

A.6 Light Scattering Effects

The two models used thus far in explaining the form of the LDA signal from the PM tube (Doppler and fringe) do not take into account how the size and optical properties of the scattering particle can affect the quality of the LDA signal. The size and optical properties of the scattering particles affect the angular distribution of the intensity, polarization, and phase of the scattered light.

The effects of size and optical properties of the scattering particle on the quality of the signal received by the photodetector is generally measured by the following three quantities: 1) signal quality, 2) signal strength, and 3) signal-to-noise ratio. Signal quality is defined as (Durst, Melling, and Whitelaw, 1976)

$$\eta = \frac{I_{max} - I_{min}}{I_{max} + I_{min}} \qquad (A.26)$$

where I_{max} and I_{min} refer to the scattered light intensities. Signal quality is therefore a measure of the depth of modulation of the Doppler signal. Signal quality is also referred to as signal visibility in the literature. Signal strength is defined to be the difference between the maximum and minimum value of the instantaneous light intensity (Durst, Melling, and Whitelaw, 1976). A discussion and definition of signal-to-noise ratio (SNR) is deferred until Section A.7.4.

It is the particle-size requirement that dictates the type of light scattering that occurs in LDA systems. There are three main divisions of light scattering: 1) Rayleigh, 2) Mie, and 3) reflection. Rayleigh scattering is caused by light scattering from molecules and atoms, and is characterized by very low scattering intensities. Mie scattering is caused by light scattering from small impurities in the fluid. For this type of scattering to occur the wavelength of the incident light must be approximately equal to the particle diameter. This type of scattering per particle exhibits a 10^{12}-10^{17} greater intensity level than Rayleigh scattering (Durst, 1972). Light scattered by reflection occurs when the particles are large enough that they act as optically flat surfaces to the incident light. Reflected light is governed by the laws of geometric optics.

In LDA work it is necessary to use Mie-scattered light. Atoms and molecules are unsuitable as tracer particles because of low scattered-

light intensities. Particles which are large enough for reflection to occur are unsuitable for most applications because of their inability to accurately follow the fluid flow.

The intensity, polarization, and phase of Mie-scattered light depends upon the direction of observation of the scattered light, the wavelength of the incident light, the refractive index, and the size of the scattering particle. A scattering parameter has been derived which relates the particle size and its optical properties. This scattering parameter is expressed as (Durst and Eliasson, 1975).

$$\alpha = \frac{2\pi r_p m_F}{\lambda} , \qquad (A.27)$$

where m_F is the refractive index of the surrounding fluid. For the case of Mie scattering, Figs. A.7 and A.8 depicts an example of the spatial variation of the scattered light intensity, phase, and polarization for scattering by a spherical particle in which a = 10 (Durst and Eliasson, 1975).

There are a few important light-scattering facts relevant to LDA systems that can be stated at this point with the help of Fig. A.7. First, large particles produce complicated, rapidly-varying scattered intensity fields. Secondly, there is a primary scattering lobe at either $\theta=0°$ or $\theta=180°$, depending on the type of particle used. For dielectric particles the primary scattering lobe occurs at $\theta=0°$. For metallic particles the primary scattering lobe is found at $\theta=180°$, making metallic particles more suitable for use in backscatter systems. Finally, scattered light is in

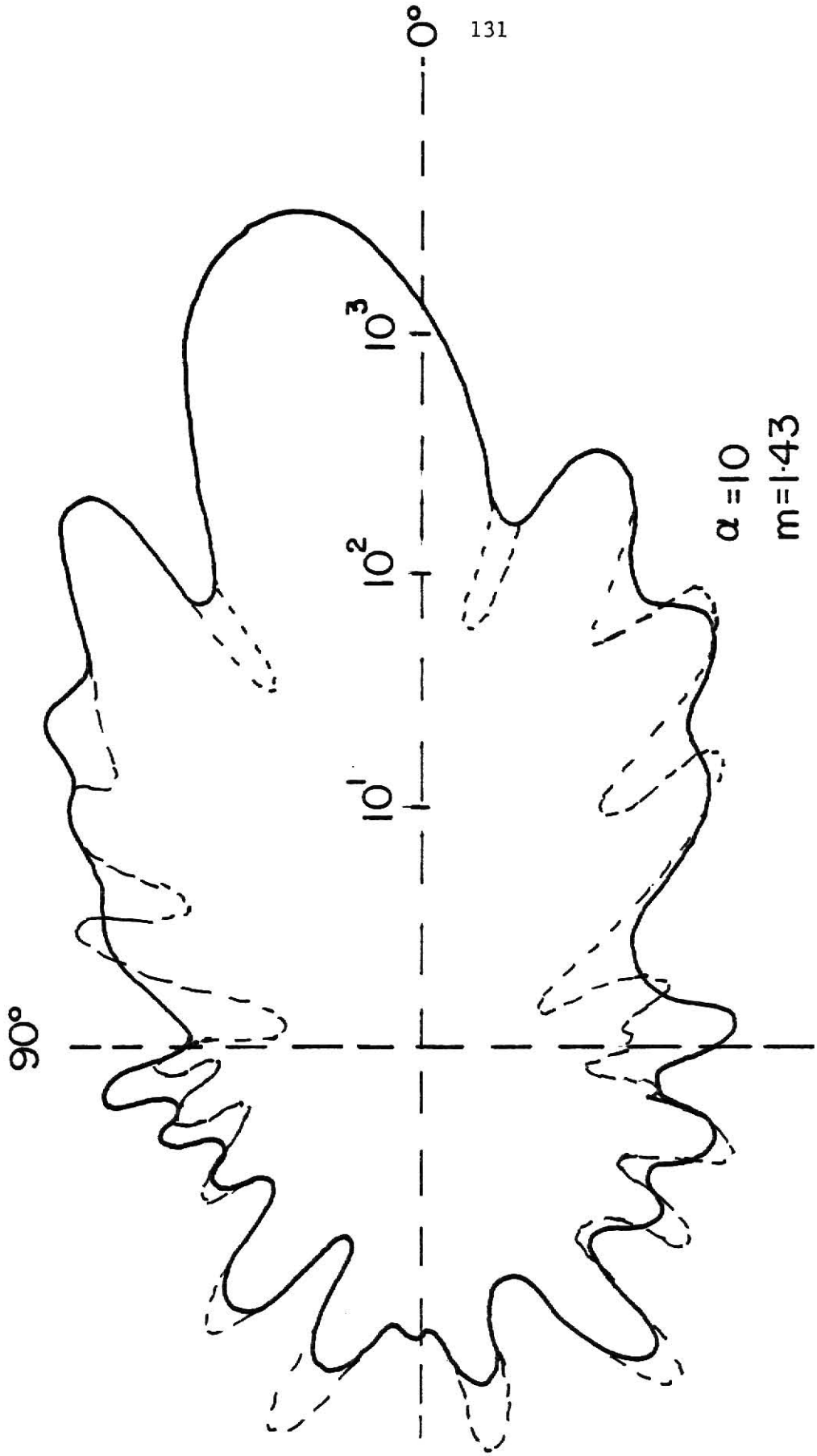

Fig. A.7. Spatial Intensity Distribution of Scattered Light Waves (from Durst and Eliasson, 1975).

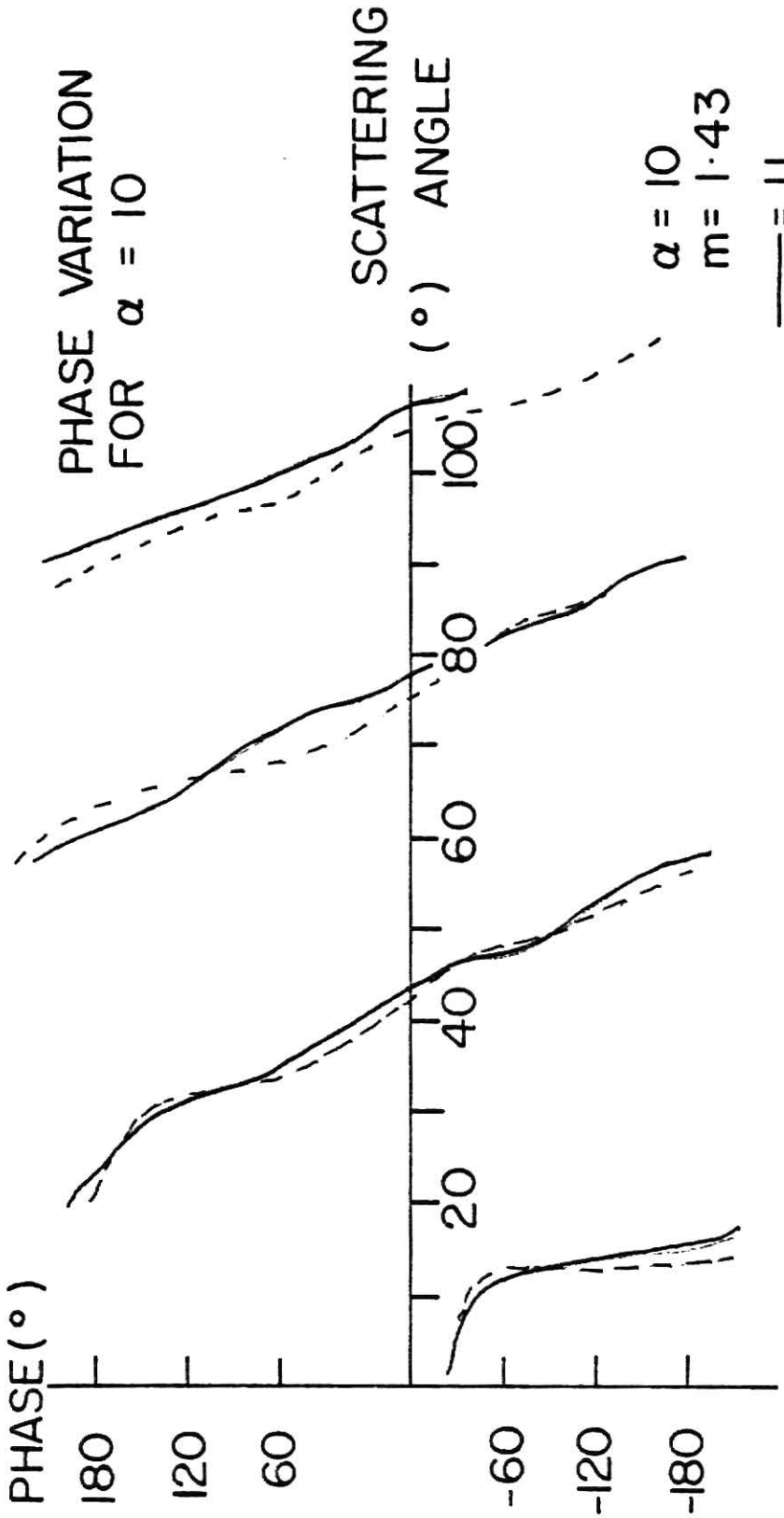

Fig. A.8. Spatial Phase Variations of Scattered Light Waves (from Durst and Eliasson, 1975).

general elliptically polarized. However, light scattered paraxially (i.e., θ=0° or 180°) from a linearly polarized incident light wave is linearly polarized in the same direction. Scattered light also remains linearly polarized for the electric vector either perpendicular or parallel to the plane of observation (the plane of observation is defined as the plane containing both the illuminating ray and the scattered ray) (Born and Wolf, 1975).

For the more realistic case of non-spherical particles there is a polarization change even for small scattering angles (Kerker, 1969). This is not a problem for the one-component dual-beam system. Two colinear, elliptically polarized scattered light waves either add in phase (reinforce one another when the scatter center is in a bright fringe) or add out of phase (cancel one another) when in a dark fringe, even through the polarizations of the two scattered light waves are elliptical. The elliptical polarizations only become a problem in two-component LDA systems that are based on orthogonal fringe patterns (Brayton, Kalb, and Crosswy, 1973).

For a dual-beam system, in which the half-angle of intersection between the two beams is ψ, the resultant light-intensity distribution and phase variations in space at an instant in time for both scattered light waves are depicted in Figs. A.9 and A.10. It is apparent from this figure that for a certain direction in space the two scattered light waves have different intensities and phases. It can thus be seen that at a point on the photodetector surface that the phases of the two scattered light waves and the resultant intensity will con-

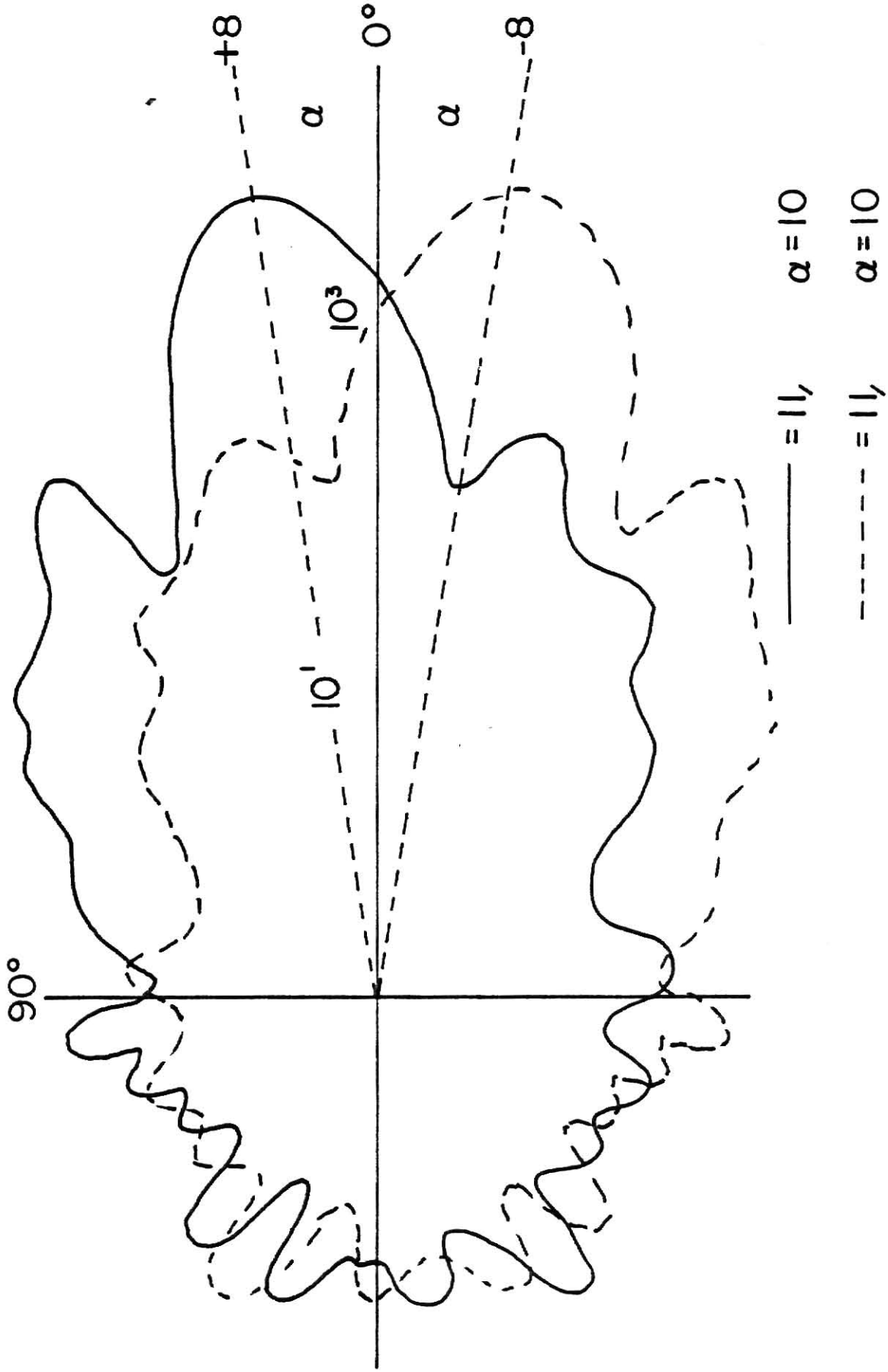

Fig. A.9. Spatial Intensity Variation of Two Scattered Light Waves Inclined 16^0 with Respect to Each Other (Durst and Eliasson, 1975).

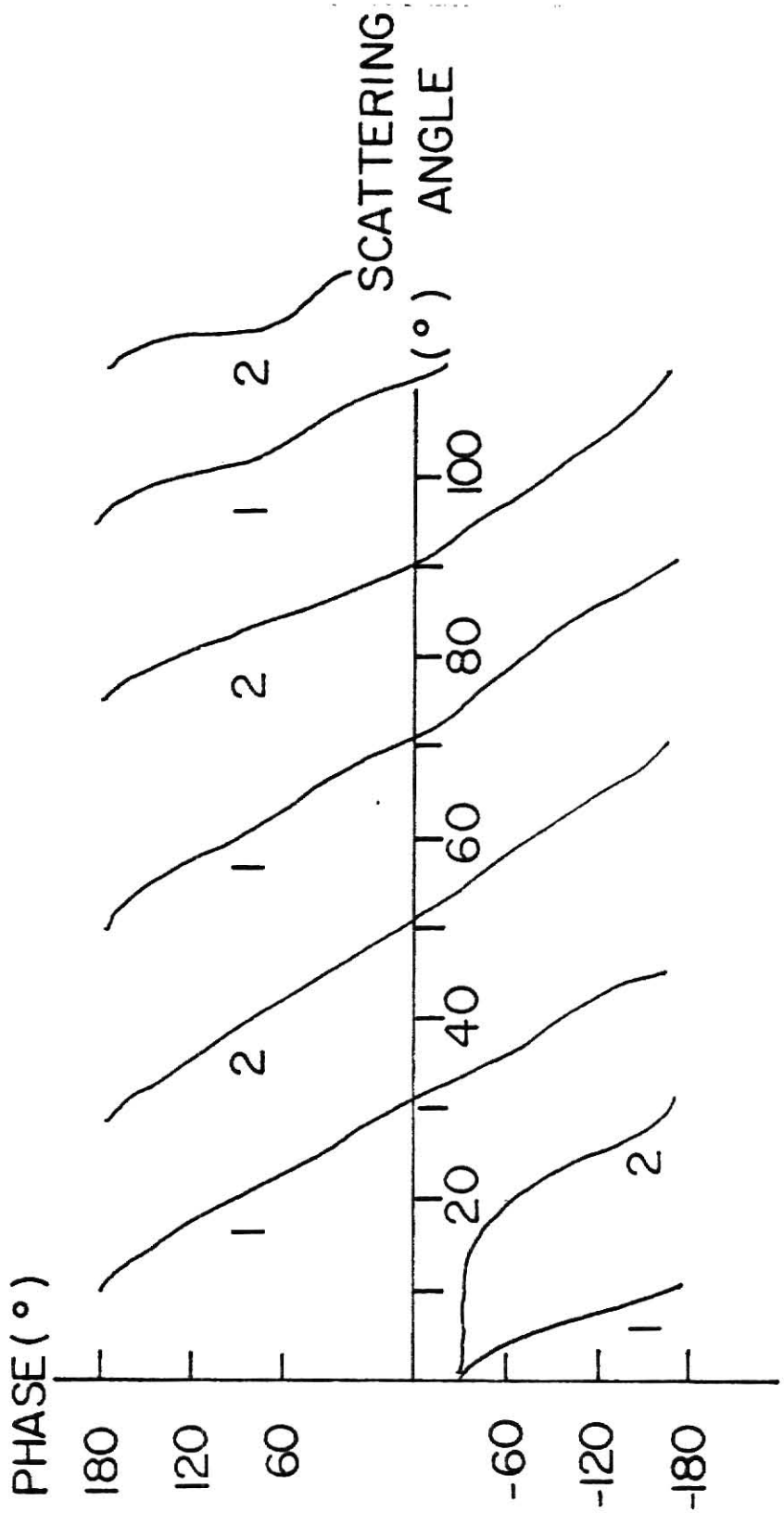

Fig. A.10. Spatial Phase Variation of Two Scattered Light Waves Inclined 16^{o} with Respect to Each Other (Durst and Eliasson, 1975).

tinually change as the particle traverses the measuring volume. In other words, LDA is based on the scattered light phase variations on the photodetector surface caused by particle motion within the incident waves and by their movement relative to the photodetector.

Because the intensity of the scattered light varies in space, the signal quality and signal strength are strongly direction-dependent due to particle-size effects. The azimuthal distributions of both the signal strength and signal quality show that both quantities are influenced primarily by the half-angle of intersection between the two scattering light beams and the direction from which the scattered light is collected (Durst, Melling, and Whitelaw, 1976). The best values for signal strength and signal quality for any half-angle of intersection are obtained when the scattered light is obtained along the optical axis. Thus when employing off-axis light-collection systems there will be a reduction in both the signal quality and signal strength from that which is obtained using on-axis light collection.

A.7 Signal Characteristics

Using the dual-beam system depicted in Fig. A.3a, Doppler signals can be generated by rotating a glass plate coated with dust particles through the scattering volume. The dust particles act as scattering centers. Figure A.11 depicts a typical signal from the PM tube generated by only one scattering center present in the scattering volume. This type of signal is known either as a Doppler burst or as an individual-realization signal (Donohue, McLaughlin, and Tiederman, 1972). Figure A.12 gives an example of the type of signal generated when there are multiple

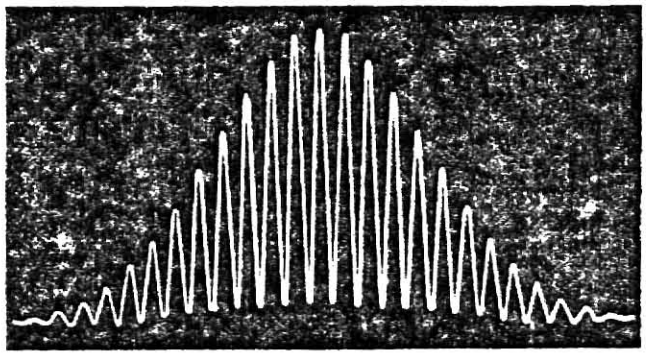

Fig. A.11. Single-Particle Doppler Burst.

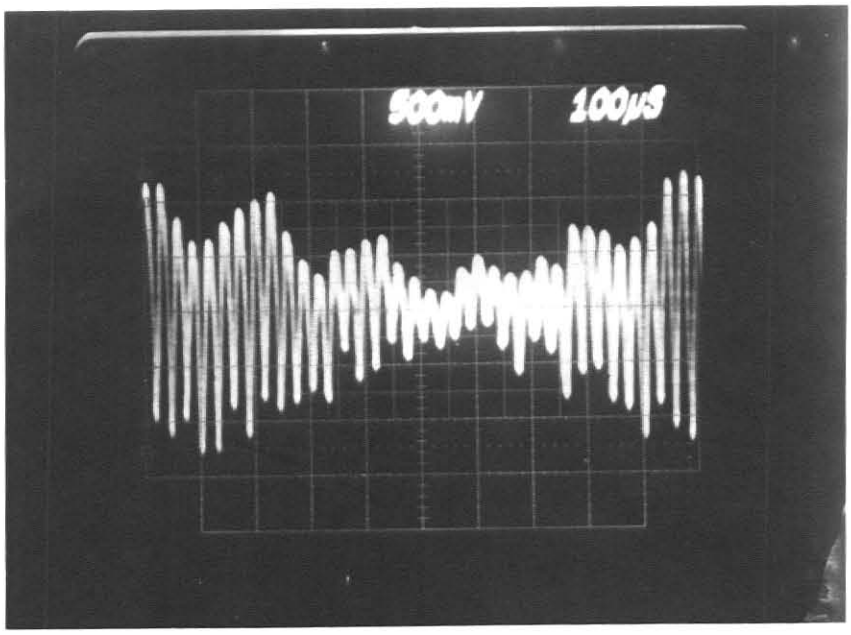

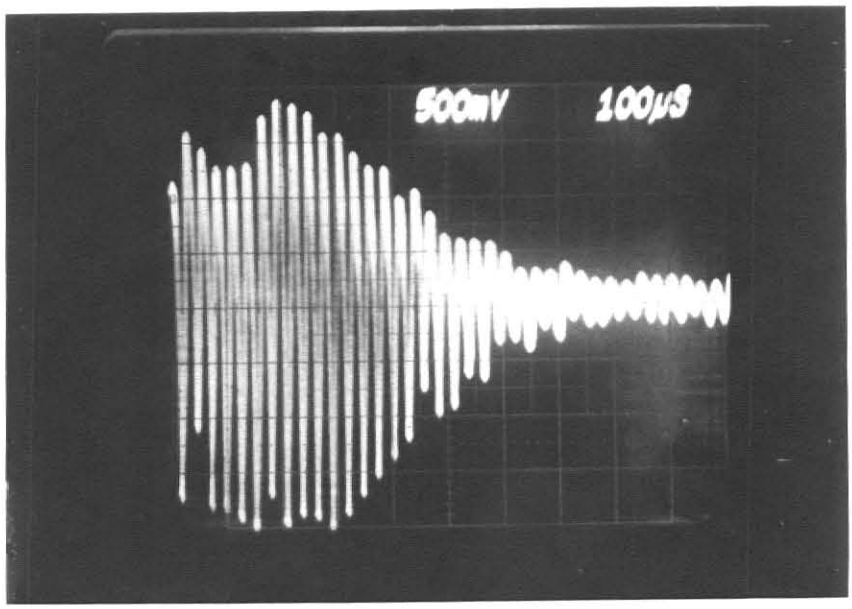

Fig. A.12. Multiple-Particle Continuous Signals.

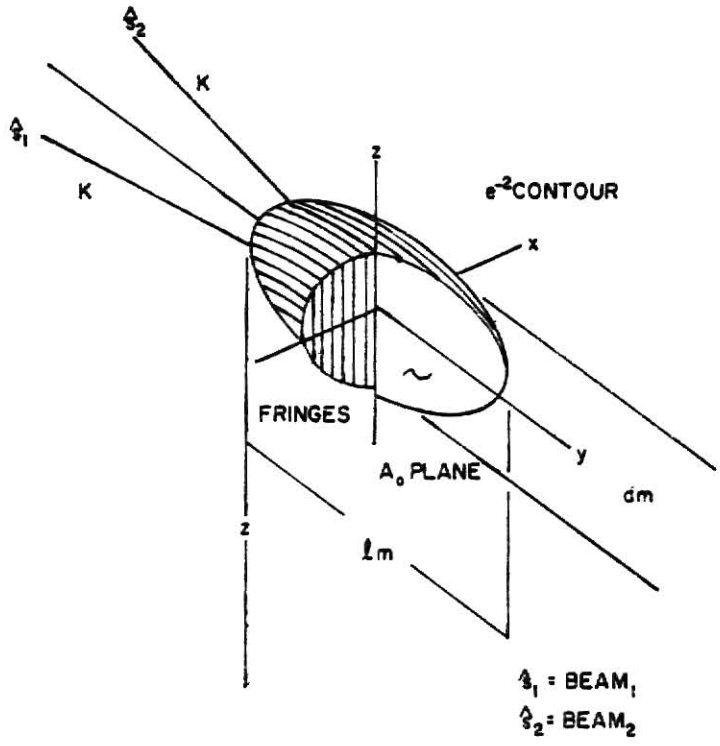

Fig. A.13. LDA Scattering Volume (from TSI News, 1977).

particles present in the scattering volume. This type of signal is generally known as a continuous signal. The characteristics of these two types of signals (amplitude variations, signal modulation variations, and the signal-to-noise ratios) will form the basis for discussion in this section.

A.7.1 Amplitude Variations

For the single-particle scatter case depicted in Fig. A.11 notice that the amplitude of the signal appears to vary in a Gaussian fashion. This is due to the light-intensity profile associated with lasers. The usual mode of operation of a laser in LDA work is the TEM_{oo} mode (this means there are no transverse standing-waves in the laser cavity). For this mode of operation the intensity profile of the laser beam perpendicular to the axis of propagation is Gaussian, and the wavefronts are plane and parallel (Eckert and Goldstein, 1976). Thus when the two Gaussian-intensity laser beams are intersected the resulting scatter-volume shape reflects the Gaussian-intensity dependence of the laser light.

The shape of the scattering volume is usually defined by either the e^{-1} or e^{-2} intensity contour of the beam-intersection region. For example, the e^{-1} intensity contour defines the region in which the intensity at every point is at least .37 times that of the maximum intensity present in the geometric center of the scattering volume. Figure A.13 depicts the shape of the scattering volume as well as the fringes that are present. As can be seen in Fig. A.13 the scattering-

volume intensity falls off in a Gaussian fashion in both the radial and axial direction. Mathematically, the scattering volume is labeled an ellipsoid of revolution.

Since the intensity variation of the scattering volume has a Gaussian profile the amplitude of the signal detected by the photodetector will also vary in a Gaussian fashion. Thus in Fig. A.9 the peak amplitude of the Doppler burst corresponds to a particle position at the centerline of the scattering volume.

Amplitude variations for the continuous signal case depicted in Fig. A.10 depends not only on the Gaussian-intensity profile of the scattering but also on the particle concentration in the scattering volume. For the multiple-particle case all of the individual signals generated by each scattering particle are added to form the output signal from the photodetector. Because the particles are randomly dispersed in the scattering volume they will generate individual signals which have random amplitudes with respect to each other. Thus the amplitude of the signal output from the PM tube will vary as a function of time according to the concentration and position of the scattering particles present in the scattering volume.

A.7.2 Signal Modulation Characteristics

The modulation of the signal from the PM tube depends primarily on four factors: particle size, particle path through the probe volume, particle concentration, and the angular distribution of the scattered-light intensity. The particle-size effect can be visualized by referring to the fringe model and neglecting the Gaussian intensity variation present

in the scattering volume. If the particle diameter is less than half of the fringe spacing, then as the particle travels through the scattering volume it will produce a fully-modulated signal from the PM tube. However, if the particle dimater is larger than half the fringe spacing, the amplitude of the PM tube signal will increase but the modulation will decrease because the total integrated intensity is never zero. For particles of a certain size the modulation may disappear completely (Stevenson, 1977). This does not mean that it is not possible to obtain good signals with these larger particles. Several investigators have found that particles much larger than the fringe spacing can produce excellent signals due to diffraction and refraction effects (e.g., Durst and Eliasson, 1975).

As shown in Section A.3 the modulation of the signal is only 100% when the intensity of the two-interfering light waves are equal. Because of the Gaussian-intensity falloff both radially and axially in the scattering volume, points of equal intensity occur only near the geometric center of the scattering volume. Signal modulations that can be expected for various particle paths through the scattering volume are detailed in a paper written by Brayton (1974).

Particle concentration plays an important role in the Doppler-signal modulation. If two particles see the same intensity modulation and they are in phase (i.e., when one is in a bright fringe the other is also in a bright fringe) the two signals generated will reinforce each other at the surface of the photodetector and a well-modulated signal will result. If they are not in phase (i.e., one is in a dark fringe

and one is in a bright fringe) complete phase cancellation could occur which leads to a complete loss in the signal. As the number of scattering particles in the scattering volume increase the modulation depth and the amplitude of the signal decreases (Durst, Melling, and Whitelaw, 1976).

In the previous discussion on signal modulation it was implicitly assumed that the scattered-light intensity from both beams were equal. Due to Mie-scattering effects the intensities may not be equal, leading to a further reduction in the modulation depth. In Fig. A.8 it can be seen that the intensity of the two scattered-light waves are equal only along the axis bisecting the two interfering light beams. Thus, LDA systems employing off-axis light-collection optics will suffer reduced signal modulation due to this effect.

A.7.3 Signal-to-Noise Ratio

The signal-to-noise ratio (SNR) is an important quantity used when describing the characteristics of the three different types of LDA systems described in Section A.4. Noise sources in LDA applications determine the lower limit of signal detection, and so it is necessary to understand what the sources of noise are and where they occur. Although noise is usually thought of in the electronics sense, noise is generally defined as any effect that detracts from the ability to determine the Doppler signal. In LDA applications noise sources can be divided into three areas: 1) optical noise sources, 2) photodetection effects, and 3) electronics noise.

Optical noise sources include diffractive and refractive beam perturbations, coherence degradation (due to effects mentioned in Section A.5), light dispersion from lenses and medium, and laser hum. Usually these effects are minimal if careful design of the optical configuration is employed (i.e., use diffraction-limited lenses, minimize optical path-length differences, etc.). Another optical noise source in spurious heterodyne signals generated at the photodetector by laser reflections or flare. This problem is minimized by the use of an aperture in the receiving optics that allows only light scattered from the scattering volume to be imaged on the surface of the photodetector.

Another optical noise source is the introduction of noise by light-scattering effects. Noise generated in this manner comprises one of the two major sources of noise in LDA systems, and was examined in a paper written by Durst (1975). In this paper Durst assumed the laser light was of constant intensity. With this assumption the laser light has a SNR of infinity before any scattering has occurred. The scattering process reduces this infinite value to a finite value because the particle can absorb the photon as well as scatter it. This process is irreversible - no amount of noise-free amplification will be able to improve the photon signal-to-noise ratio. Thus it is important to use particles with large scattering cross-sections in LDA systems.

Signal perturbations caused by electronic noise is due primarily to Johnson noise. Johnson noise is caused by thermal movements of conducting

electrons in resistors. The use of PM tubes easily overcomes this noise source as the signal level is raised considerably over the Johnson-noise level by the secondary-emission and low-noise amplifications process of the dynode structure.

Thermal effects are also responsible for dark current in PM tubes. Dark current is electron emission from the PM tube photocathode caused by thermal excitation of the photocathode material. Thus dark current is present in PM tubes even if there is no light incident on the photocathode surface. In most LDA applications the current due to the scattered light is much higher than the dark current, so the dark current can be neglected (Durst, 1975).

The other primary source of noise present in LDA systems is shot noise present at the photocathode of the PM tube. Shot noise appears as random fluctuations in the PM tube output about a mean value. Explaining further, if the light flux incident on the photocathode is constant, the mean rate of emission of photoelectrons is also constant, but the number of photo-emissions in any finite time interval fluctuates in a random fashion about the mean value. This process is known as a Poisson process (Durrani and Greated, 1977). Thus, in LDA systems the signal from the photodetector will exhibit shot noise as high-frequency fluctuations in the signal. Because the generally noise-free amplification present in the secondary-multiplication structure of the dynode chain in PM tubes overcomes most other noise sources, the detection process in optical aneometry is shot-noise limited. Most of the SNR values reported in

the literature are signal-to-shot noise ratios (Durst, 1975).

For reference-beam systems, the SNR (shot-noise limited) can be expressed as (Wang, 1972)

$$SNR \sim n_p \sigma_p \, (\lambda_L^2 / 1_s^2) \tag{A.28}$$

For dual-beam systems the SNR can be expressed as (Wang, 1972)

$$SNR \sim \left(\frac{\sigma_p}{n^{5/3}}\right) \left(\frac{\lambda_L^2}{1_p^2}\right) . \tag{A.29}$$

Equation (A.28) indicates that the SNR increases with particle concentration for reference-beam systems, while for dual-beam systems Eq. (A.29) indicates that the SNR decreases with increasing particle concentration. The dependence of the SNR on particle concentration for both the dual-beam and reference beam systems is borne out by experimental evidence (Wang and Synder, 1974). In fact little is gained in SNR by going above one or two particles in the scattering volume for the dual-beam system (Drain, 1972). In the case of reference beam systems it should be mentioned that the SNR will increase with increasing particle concentration, but will begin to decrease at the point at which light-attenuation effects become important.

A.8 Signal Analysis

This section will briefly detail the electronic data analysis methods used in LDA systems, and will also discuss the sources of error and uncertainties present in the analysis of the PM tube signal.

A.8.1 Data Analysis Methods

There are four different types of electronic data-processing systems

used in LDA systems: 1) frequency or spectrum analyzers, 2) frequency tracking demodulators, 3) fixed-gate frequency counters, and 4) period timers. One of the first type of signal processors used in LDA systems was the spectrum analyzer. The spectrum analyzer operates in the frequency domain and can be obtained by using an oscilloscope with a plug-in spectrum analyzer in which the visual display yields signal intensity (ordinate) vs. frequency (abscissa). The output from a complete spectrum analyzer set-up is a true representation of the probability density distribution of the frequency of the signal. This is completely true only if the mean number and size of the scattering centers passing through the scattering volume does not change with time (Durst, Melling, and Whitelaw, 1976). Another limitation associated with spectrum analyzers is that since a probability-density distribution is being developed at a particular measurement location it is not possible to obtain real-time information on the velocity at that point.

Frequency tracking demodulators (or frequency trackers) were developed exclusively for LDA work. Frequency trackers provide instantaneous frequency-to voltage conversion yielding real-time information on the velocity at the measurement point. Frequency trackers provide a continous signal even though the corresponding input signal may be discontinuous (as it can be for low particle concentration). Present trackers have "drop-out detection" and "hold" features, but the output must still be treated with care if the input signal has a large-percentage drop-out time. Not only is signal drop-out a problem

but large frequency variations in the signal (i.e., have highly-turbulent flow) can also cause the tracker to lose the signal.

Fixed-gate counting involves counting over a preset time the number of times the signal amplitude crosses a preset trigger level. The gate time must be less than the particle transit time through the scattering volume, or errors will result. Thus fixed-gate counting systems are limited to flow-fields where there are only small velocity-variations with time.

Period timing was developed to overcome the problems associated with fixed-gate counting systems (i.e., large frequency variations). This technique measures the time it takes a particle to cross a preset number of fringes. The burst counter is the name of the period-timing instrument that has been developed and put to great use for single-particle scatter applications.

There are other techniques that have been used other than the four primary techniques already mentioned. One is the filter bank in which banks of filters are used to process the signal in the frequency domain (as opposed to the spectrum analyzer which only uses one filter to sweep the frequency range of interest). The primary advantage of filter banks is that real-time information can be obtained. Another technique gaining wider acceptance is photon correlation. Its main advantages are the ability to work with low levels of light intensity and good noise-rejection capabilities. Finally, all of the electronic data-analysis techniques mentioned thus far depend on the mixing of coherent light waves. For high-velocity

flows it has been possible in some cases to determine directly the magnitude of the Doppler-shifted light through the use of Fabry-Perot etalons (Durst, Melling, and Whitelaw, 1976).

A.8.2 Uncertainties and Errors in Data Analysis

One of the most important complications associated with the use of LDA systems is that the velocity measurements are made using particles randomly distributed in the fluid. Recall in Section A.6 it was stated that LDA is based on scattered-light phase variations on the photodetector surface caused by particle motion within the incident light wave and by their movement relative to the photodetector. The output signal from the photodetector is the result of the sum of all the signals produced by all of the scatterers present in the scattering volume at that instant in time. Each individual signal has the same frequency (in the case of laminar flow), but each has a different phase which is dependent on the particle position in the scattering volume (recall that the intensity of each scattered light wave is dependent also on particle position and size). Thus the resultant frequency of the output signal from the photodetector varies with time as signals from particles leaving the scattering volume at arbitrary times are lost and replaced by signals from newly-entering particles. Two statements can be made at this point:
1) the output signal from the PM tube fluctuates in frequency even if the flow is laminar, and 2) the uncertainty in the frequency determination due to phase fluctuations is related to the particle transit time and thus to the dimensions of the scattering volume. The broadening due to random phase additions is usually labeled finite transit-time broadening.

For the case where the output of the data-analysis instrumentation yields a probability-density distribution (e.g., spectrum analyzers or the instrumentation used for the research done for this thesis) the finite life-time broadening can be expressed as (George and Lumley, 1973).

$$\Delta f_t = \frac{\overline{u}}{4\pi\sigma} . \qquad (A.30)$$

where σ is the dimension of the scattering volume parallel to the direction of the flow.

Finite transit-time broadening is the main source of uncertainty present in most LDA systems. There are three other sources of broadening that can occur due to 1) variations of local velocity with time (as in turbulent flows), 2) broadening due to optical imperfections, and 3) broadening due to spatial variations in velocity. Broadening due to spatial variations in velocity can be minimized by decreasing the scattering volume size. Decreasing the scattering volume size will increase the finite transit-time broadening (refer to Eq. (4.30)). Thus there is a trade-off that exists between spatial and spectral resolutions of the velocity.

The main source of uncertainty that can occur with optical broadening is due to improper focusing of the two Gaussian-intensity laser beams to form the intersection volume. For Gaussian-intensity laser beams that are focused the wavefronts are plane and parallel only near the location of the beam waist (the beam waist is defined as the location of the smallest beam diameter). Using Fig. A.12, the location of the focused waist of a Gaussian-intensity laser beam is

given by the following equation (Durst and Stevenson, 1979),

$$\omega_1 = \frac{\omega_{of}}{[(Z_o-f)^2 + (\frac{\pi\omega_o}{\lambda})^2]^{1/2}} . \qquad (A.31)$$

Thus, the focused waist is located in the lens focal plane only if the input beam waist is located at the back focal plane or at an infinite distance. The result of improper beam focusing on the measured mean frequency is illustrated in Fig. A.13, in which it can be seen that a broadening of the signal will occur due to unequal fringe spacing. Generally speaking, this type of frequency broadening is only a problem when accurate measurements of turbulence parameters are to be made in flows of low turbulence intensity (Durst and Stevenson, 1979).

Due to the frequency broadening effects that have been previously mentioned, it is not possible to interpret the broadening of the probability-density distribution as due only to variations of velocity with time if a turbulent flow-field is being measured. It is necessary, therefore, to have a well-designed optical system to minimize broadening of the signal due to the optical components and spatial-variations of velocity in the scattering volume, and also to correct the frequency probability-density distribution for transit-time broadening in order to obtain information on turbulence parameters.

APPENDIX B

DISCUSSION OF POLFIT

The code POLFIT was used to calculate a linear fit to the frequency data collected according to the procedure outlined in Sect. 3.1 for the frequency calibration of the LDA signal-analysis instrumentation. POLFIT was obtained from the reference by Bevington (1969). This code is used to fit a polynomial function to a set of data. The program calculates the coefficients a, b, c, d, etc., associated with the polynomial fit to the data points. For this study, however, it was used to calculate a linear least-squares fit to the data generated by the frequency calibration of the LDA signal-analysis system described in Sect. 3.1 so as to obtain Eqs. (5) and (6).

Input data for the routine consists of the x and y data points, the number of points to be fitted (NPTS), the degree of the polynomial fit to be tried (N1), and a control parameter (MODE) that determined the method of weighting the fit. For this study MODE = 0, which meant no weighting was applied to the input data points as the fit was being calculated.

Although POLFIT is capable of applying a second and higher-order fit to the data, only a linear fit was applied to the data. The output from the program consisted of values associated with the form of the fit.

A computer listing of the program is given in the following pages.

ILLEGIBLE DOCUMENT

THE FOLLOWING DOCUMENT(S) IS OF POOR LEGIBILITY IN THE ORIGINAL

THIS IS THE BEST COPY AVAILABLE

```
C ***********************************POLFIT*************************************
C *                                                                            *
C *      POLFIT IS TAKEN FROM THE BOOK DATA REDUCTION AND ERROR                *
C *      ANALYSIS FOR THE PHYSICAL SCIENCES BY P.R. BEVINGTON                  *
C *                                                                            *
C *                                                                            *
C *      THIS PROGRAM CALCULATES A LEAST-SQUARES FIT TO DATA WITH              *
C *      A POLYNOMIAL CURVE                                                    *
C *                                                                            *
C *      THREE SETS OF INPUT DATA ARE NEEDED.  THE FIRST SET CONTAINS          *
C *      THE FOLLOWING QUANTITIES:                                             *
C *        NPTS= NUMBER OF POINTS TO BE FITTED                                 *
C *        N1= DEGREE OF POLYNOMIAL TO USE IN FIT                              *
C *        MODE= METHOD OF WEIGHTING TO BE APPLIED TO INPUT DATA               *
C *      THE SECOND DATA SET CONTAINS THE ARRAY OF DATA POINTS                 *
C *      FOR THE INDEPENDENT VARIABLE, WHILE THE THIRD SET CONTAINS            *
C *      THE ARRAY OF DATA POINTS FOR THE DEPENDENT VARIABLE.                  *
C *                                                                            *
C ******************************************************************************
C
      IMPLICIT REAL*8(A-H,O-Z)
      DIMENSION X(40),Y(40),SIGMAY(40),A(40),XX(40),YY(40)
      DIMENSION SUMX(40),SUMY(40),ARRAY(40,40)
   99 WRITE(6,1)
    1 FORMAT(////,5X,'THIS PROGRAM PERFORMS A LEAST SQUARE FIT TO DATA
     1',///,5X,'WITH A POLYNOMIAL CURVE.',///,5X,'ENTER THE NUMBER OF DATA
     2A POINTS')
    3 FORMAT (3I3)
    4 READ (5,3,END=80) NPTS,N1,MODE
      READ(5,610)(XX(I),I=1,NPTS)
  610 FORMAT (10F8.2)
      READ(5,620)(YY(I),I=1,NPTS)
  620 FORMAT (10F8.2)
  150 NTERMS=N1+1
      DO 2 I=1,NPTS
      X(I)=DLOG(XX(I))
      Y(I)=DLOG(YY(I))
    2 CONTINUE
C
C        ACCUMULATE WEIGHTED SUMS
C
   11 NMAX=2*NTERMS-1
      DO 13 N=1,NMAX
   13 SUMX(N)=0.000
      DO 15 J=1,NTERMS
   15 SUMY(J)=0.000
      CHISQ=0.000
   21 DO 50 I=1,NPTS
      X1=X(I)
      Y1=Y(I)
   31 IF(MODE)32,37,39
   32 IF(Y1)35,37,33
   33 WEIGHT=1.000/Y1
      GO TO 41
   35 WEIGHT=1.000/(-Y1)
      GO TO 41
   37 WEIGHT=1.000
      GO TO 41

   39 WEIGHT=1.000/SIGMAY(I)**2
   41 XTERM=WEIGHT
      DO 44 N=1,NMAX
      SUMX(N)=SUMX(N)+XTERM
   44 XTERM=XTERM*X1
   45 YTERM=WEIGHT*Y1
      DO 48 N=1,NTERMS
      SUMY(N)=SUMY(N)+YTERM
   48 YTERM=YTERM*X1
   49 CHISQ=CHISQ+WEIGHT*Y1**2
   50 CONTINUE
C
C        CONSTRUCT MATRICES AND CALCULATE COEFFICIENTS
C
   51 DO 54 J=1,NTERMS
      DO 54 K=1,NTERMS
      N=J+K-1
   54 ARRAY(J,K)=SUMX(N)
      DELTA=DETERM(ARRAY,NTERMS)
      IF(DELTA)61,57,61
   57 CHISQR=0.000
      DO 59 J=1,NTERMS
   59 A(J)=0.000
      GO TO 80
   61 DO 70 L=1,NTERMS
   62 DO 66 J=1,NTERMS
      DO 65 K=1,NTERMS
      N=J+K-1
   65 ARRAY(J,K)=SUMX(N)
   66 ARRAY(J,L)=SUMY(J)
   70 A(L)=DETERM(ARRAY,NTERMS)/DELTA
```

```
C
C       CALCULATE CHI SQUARE
C
   71 DO 75 J=1,NTERMS
      CHISQ=CHISQ-2.000*A(J)*SUMY(J)
      DO 75 K=1,NTERMS
      N=J+K-1
   75 CHISQ=CHISQ+A(J)*A(K)*SUMX(N)
   76 FREE=NPTS-NTERMS
   77 CHISQR=CHISQ/FREE
   79 WRITE(6,100)NL
  100 FORMAT(///////,5X,'FORM OF FIT: A1+A2*X+A3*X**2+...',///,5X,'DEGREE
     1E OF FIT:  ',I2)
      DO 105 I=1,NTERMS
  105 WRITE(6,110)I,A(I)
  110 FORMAT(//,10X,'I=',I2,10X,'A(I)=',E12.5)
      WRITE(6,115)CHISQR
  115 FORMAT(//,1X,'CHISQR=',E12.5)
      GO TO 4
   80 STOP
      END

      FUNCTION DETERM(ARRAY,NORDER)
C.....
C                                                                       .
C       THIS PROGRAM IS TO CALCULATE THE DETERMINANT OF A SQUARE MATRIX .
C                                                                       .
C..................................... PARAMETERS ....................
C                                                                       .
C       ARRAY  -  MATRIX                                                .
C       NORDER -  ORDER OF DETERMINANT (DEGREE OF MATRIX)               .
C                                                                       .
C.....
C
      IMPLICIT REAL*8(A-H,O-Z)
      DIMENSION ARRAY(40,40)
   10 DETERM=1.000
   11 DO 50 K=1,NORDER
      IF(ARRAY(K,K))41,21,41
C                                                                       .
C         INTERCHANGE COLUMNS IF DIAGONAL ELEMENT IS ZERO
C
   21 DO 23 J=K,NORDER
      IF(ARRAY(K,J))31,23,31
   23 CONTINUE
      DETERM=0.000
      GO TO 60
   31 DO 34 I=K,NORDER
      SAVE=ARRAY(I,J)
      ARRAY(I,J)=ARRAY(I,K)
   34 ARRAY(I,K)=SAVE
      DETERM=-DETERM
C
C         SUBTRACT ROW K FROM LOWER ROWS TO GET DIAGONAL MATRIX
C
   41 DETERM=DETERM*ARRAY(K,K)
      IF(K-NORDER)43,50,50
   43 K1=K+1
      DO 46 I=K1,NORDER
      DO 46 J=K1,NORDER
   46 ARRAY(I,J)=ARRAY(I,J)-ARRAY(I,K)*ARRAY(K,J)/ARRAY(K,K)
   50 CONTINUE
   60 RETURN
      END
```

APPENDIX C: DISCUSSION OF LDAAP

The code LDAAP, laser-doppler anemometry analysis and plot, calculates a value for the average velocity given a frequency probability distribution such as that generated by the LDA system used in this study. The code inputs the frequency probability distribution from a 800 bpi (bytes per inch) 9-track magnetic tape. In addition, the code will plot the frequency probability distribution if so desired.

The program inputs are the number of channels in the spectrum (NCHNLA-1024 max), the identification number associated with the spectrum of interest (MID1, the start and stop channel locations of the peak NPEAK1, NPEAK 2), the two constants (A_1 and A_2) used in the frequency calibration of the multichannel analyzer (recall Eqs. (5) and (6)), and either a one or a zero (NPLOT) that is used to determine whether or not to plot the frequency probability-distribution. If a plot of the distribution is desired (NPLOT = 1) another input card is required; and this card contains plotting parameters, i.e., start x- and y-values, and ΔX and Δy values for the spacing associated with the axes of the plot. Plotting is done on an 8-inch (y-axis) by 6-inch (x-axis) plot, so the plotting parameters must be selected accordingly.

Once the desired spectrum from the magnetic tape has been found and inputted to the arrays set up by the program, the program evaluates for the average frequency of that spectrum using a frequency calibration of the form of Eq. (5) or (6) and Eq. (8). This value for the average frequency is then used in Eq. (9.21) to calculate the average velocity. The program then prints out the spectrum identification number and the associated average velocity.

Note that the JCL (job control language) associated with this program is specifically designed for input data stored on 800 bpi, 9-track tapes. Any future users should be aware that the Kansas State University Computing Ceter is planning a hardware change with the plotter that could affect how the program works.

The following pages contain a computer listing of LDAAP.

```
C ***********************************LDAAP*************************************
C *                                                                           *
C *      LDAAP - LASER DOPPLER ANEMOMETRY ANALYSIS AND PLOT                   *
C *      WRITTEN BY ROBERT MCGRIFF (1979)                                     *
C *                                                                           *
C *      LDAAP IS DESIGNED TO REMOVE A FREQUENCY SPECTRUM FROM A              *
C *      MAGNETIC TAPE AND ANALYZE THE SPECTRA FOR THE AVERAGE                *
C *      VELOCITY.  THE PROGRAM ALSO PROVIDES A PLOT OF THE SPECTRA           *
C *      IF SO DESIRED.  FOR THIS PROGRAM THE SPECTRA SHOULD BE RECORDED      *
C *      ON NO MORE THAN 1024 CHANNELS.                                       *
C *                                                                           *
C *      A MAXIMUM OF TWO DATA CARDS IS REQUIRED WITH THIS PROGRAM IF         *
C *      A PLOT IS REQUIRED.  IF NO PLOT IS DESIRED ONLY ONE DATA CARD        *
C *      IS USED.  THE FIRST CARD IS ALWAYS NEEDED AND CONTAINS THE           *
C *      FOLLOWING QUANTITIES:                                                *
C *        NCHNLS= NUMBER OF CHANNELS IN THE SPECTRUM                         *
C *        MID= FILE NUMBER OF DESIRED SPECTRA                                *
C *        NPEAK1= START CHANNEL NUMBER OF SPECTRUM PEAK                      *
C *        NPEAK2= END CHANNEL NUMBER OF SPECTRUM PEAK                        *
C *        A1= COEFFICIENT IN MCA CALIBRATION FORMULA WHICH IS OF             *
C *            THE FOLLOWING FORM:  LN(FREQ)=A1+A2*LN(CH.NO.)                 *
C *        A2= SEE A1 ABOVE                                                   *
C *        NPLOT= 0 IF NO PLOT IS DESIRED                                     *
C *             = 1 IF NO PLOT OF THE SPECTRUM IS WANTED                      *
C *                                                                           *
C *      IF A PLOT IS DESIRED, A SECOND CARD IS READ IN WITH THE FOLLOWING    *
C *      INPUT PARAMETERS:                                                    *
C *        X1= START VALUE FOR X-AXIS                                         *
C *        DELTX= DATA UNITS PER INCH OF AXIS                                 *
C *        Y1= START VALUE FOR Y-AXIS                                         *
C *        DELTY= DATA UNITS PER INCH OF Y-AXIS                               *
C *                                                                           *
C ***********************************************************************
C
      DIMENSION  BUF(4000),XAXIS(1030),ISPECT(1030),SPECT(1030)
      DIMENSION PEAK(1030)
      IPLT=0
C
C     READ IN INFORMATION FROM FIRST CARD DESCRIBED ABOVE
C
    9 READ (5,4,END=99) NCHNLS,MID,NPEAK1,NPEAK2,NPLOT,A1,A2
    4 FORMAT (5I5,2F8.4)
      IF (NPLOT .EQ. 0) GO TO 1
C
C     READ IN PLOTTING PARAMETERS
C
      READ (5,20) X1,DELTX,Y1,DELTY
   20 FORMAT (4F6.2)
C
C
C     READ IN DATA FROM TAPE
C
    1 READ (8,2,ERR=23,END=80) ID, (ISPECT(I),I=1,NCHNLS)
    2 FORMAT (I6,(T7,16(1X,I6)))
      IF (ID .NE. MID) GO TO 1
C
C     CHANGE INTEGER SPECTRUM VALUES TO REAL VALUES
C
      DO 10 I=1,NCHNLS
   10 SPECT(I)=ISPECT(I)
C
C     DEFINE PEAK AREA
C
      J=0
      DO 24 I=1,NPEAK2
      PEAK(I)=SPECT(I)
   24 IF (I.EQ.1) PEAK(I)=0.0
      PEAK(NPEAK2+1)=Y1
      PEAK(NPEAK2+2)=DELTY
C
C     SET UP CHANNEL NO. ARRAY (X-AXIS)
C
      DO 42 I=1,NPEAK2
   42 XAXIS(I)=I
      XAXIS(NPEAK2+1)=X1
      XAXIS(NPEAK2+2)=DELTX
C
C     CALCULATE AVERAGE VELOCITY
C
    6 SUMNUM=0.0
      SUMDEN=0.0
      DO 36 I=NPEAK1,NPEAK2
      EFREQ=A1+A2*ALOG(XAXIS(I))
      SUMNUM=SUMNUM+SPECT(I)*EFREQ
      SUMDEN=SUMDEN+SPECT(I)
   36 CONTINUE
      AVEFRE=SUMNUM/SUMDEN
      AVGFRE=EXP(AVEFRE)
      VEL=(488.0E-6*AVGFRE)/(2.0*SIN(0.0209))
```

```
C
C      WRITE VALUE FOR AVERAGE VELOCITY
C
       WRITE (6,101) MID,VEL
  101 FORMAT (10X,'SPECTRUM ID= ',I3,10X,'VELOCITY (MM/SEC) = ',E10.3)
       IF (NPLOT .EQ. 0) GO TO 9
C
C      INITIALIZE PLOTTING
C
   18 IF (IPLT.GT.0) GO TO 19
       CALL PLOTS (BUF,4000)
       CALL PLOT (0.0,-12.0,23)
       CALL PLOT (2.0,1.5,23)
       IPLT=1
C
C      DRAW AXIS
C
   19 CALL AXIS (0.0,0.0,'CHANNEL NUMBER',-14,6.0,0.0,XAXIS(NPEAK2+1),XA
      CXIS(NPEAK2+2))
       CALL AXIS (0.0,0.0,'NO. OF COUNTS',13,8.0,90.0,PEAK(NPEAK2+1),PEAK
      C(NPEAK2+2))
C
C      DRAW SPECTRUM
C
       CALL LINE (XAXIS,PEAK,NPEAK2,1,0,0)
       CALL PLOT (12.0,0.0,-3)
       GO TO 9
C
C      CLOSE PLOTTING
C
   99 WRITE (6,501)
  501 FORMAT ('1  NORMAL END')
  199 CALL PLOT (0.0,0.0,999)
       GO TO 80
   23 WRITE (6,503)
  503 FORMAT ('1 ERROR ENCOUNTERED IN TAPE - JOB ABANDONED')
   80 STOP
       END
```

VELOCITY PROFILE MEASUREMENT IN A HORIZONTAL FLUID LAYER CONTAINING HEAT SOURCES USING THE TECHNIQUE OF LASER-DOPPLER ANEMOMETRY

by

Robert Wayne McGriff

B.S. Kansas State University, 1977

A MASTER'S THESIS

submitted in partial fulfillment of the
requirements for the degree

MASTER OF SCIENCE

Department of Nuclear Engineering
KANSAS STATE UNIVERSITY
Manhattan, Kansas

1980

ABSTRACT

Velocity profiles are presented for ten different sets of measurements in the convection cell; eight with the lower boundary temperature warmer than the upper boundary, a potentially destabilizing condition, and two with the lower plate temperature cooler than the upper plate, a more stable configuration. The Rayleigh number (absolute values) ranged from 6.28×10^6 to 1.07×10^7, conditions of interest for understanding phenomenological underpinnings of both geothermal heat transfer and heat transfer in fast breeder reactors.

A one component laser-Doppler anemometry (LDA) system was designed and constructed to measure fluid-flow velocity profiles. Tests were performed with this system by measuring tangential velocities generated with a rotating glass plate. The system was then used for the first time to obtain vertical-velocity profile measurements in a fluid layer with unequal boundary temperatures and containing heat sources.

The velocity profiles were used to check assumptions in a recent semi-empirical model which has been developed to model the heat transfer mechanisms in such fluid layers. The velocity profiles indicate that the model's assumption of a quiescent lower sublayer is only partially correct for the case where the upper fluid boundary is warmer than the lower fluid boundary. Documentation was obtained that significant penetrative convection from the upper sublayer into the lower sublayer exists. Moreover, for the case where

the lower boundary is hotter than the upper boundary, no experimental evidence was found that would indicate any regions of zero-velocity flow.